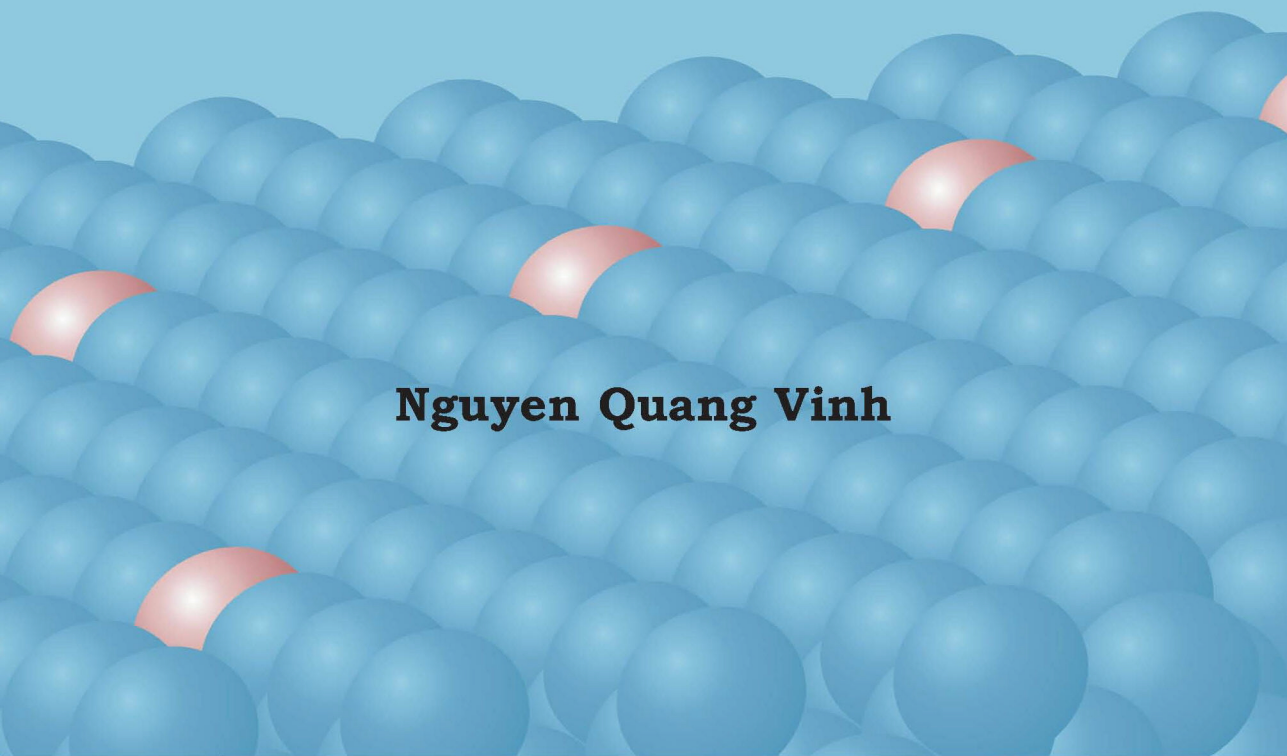


# **Optical properties of isoelectronic centers in crystalline silicon**

**Nguyen Quang Vinh**



OPTICAL PROPERTIES  
OF ISOELECTRONIC CENTERS  
IN CRYSTALLINE SILICON

Nguyen Quang Vinh



OPTICAL PROPERTIES  
OF ISOELECTRONIC CENTERS  
IN CRYSTALLINE SILICON

ACADEMISCH PROEFSCHRIFT

TER VERKRIJGING VAN DE GRAAD VAN DOCTOR  
AAN DE UNIVERSITEIT VAN AMSTERDAM,  
OP GEZAG VAN DE RECTOR MAGNIFICUS  
PROF. MR. P. F. VAN DER HEIJDEN  
TEN OVERSTAAN VAN EEN DOOR HET COLLEGE VOOR PROMOTIES  
INGESTELDE COMMISSIE, IN HET OPENBAAR TE VERDEDIGEN  
IN DE AULA DER UNIVERSITEIT  
OP DINSDAG 26 OKTOBER 2004, TE 14:00 UUR

DOOR

Nguyen Quang Vinh  
geboren te Thaibinh, Vietnam

### **Promotiecommissie**

Promotor      Prof. dr. hab. T. Gregorkiewicz  
Overige leden Prof. dr. F. R. de Boer  
                 Prof. dr. M. S. Golden  
                 Prof. dr. W. Jantsch  
                 Prof. dr. ir. J. C. Maan  
                 Dr. ir. F. P. Widdershoven

Faculteit der Natuurwetenschappen, Wiskunde en Informatica

ISBN 90-9018671-9

*The work described in this thesis was carried out at the Van der Waals-Zeeman Institute, University of Amsterdam. Some of the experimental work was done at the Dutch Free Electron Laser facility for Infrared eXperiments (FELIX) at the FOM Institute for Plasma Physics “Rijnhuizen” in Nieuwegein. The work was partially supported by the Nederlandse Organisatie voor Wetenschappelijk Onderzoek (NWO).*

*Kính tặng Cậu Mẹ*

*To my parents*



# Contents

<b>1</b>	<b>Introduction</b>	<b>1</b>
1.1	Optical centers in semiconductors . . . . .	1
1.2	Isoelectronic centers . . . . .	3
1.3	Silicon photonics . . . . .	4
1.3.1	Si:Ag, Si:Cu . . . . .	4
1.3.2	Si:Er . . . . .	5
1.4	This thesis . . . . .	5
<b>2</b>	<b>Experimental Techniques</b>	<b>7</b>
2.1	Photoluminescence and time-resolved experiments . . . . .	7
2.2	Photoluminescence excitation spectroscopy . . . . .	9
2.3	Two-color spectroscopy . . . . .	9
2.4	Magneto-optical spectroscopy . . . . .	10
<b>3</b>	<b>Optical Properties of a Silver-Related Defect in Silicon</b>	<b>13</b>
3.1	Introduction . . . . .	13
3.2	Experimental details . . . . .	15
3.3	Structure of the luminescence band . . . . .	16
3.4	Isotope effects . . . . .	19
3.5	Perturbations of the no-phonon lines by magnetic and stress fields .	21
3.6	Electron-phonon coupling . . . . .	26
3.7	Thermal quenching of the luminescence . . . . .	30
3.8	Summary . . . . .	34
<b>4</b>	<b>Two-Color FEL Spectroscopy of Isoelectronic Center in Silicon</b>	<b>35</b>
4.1	Introduction . . . . .	35
4.2	Experimental details . . . . .	37
4.3	Results and discussion . . . . .	38
4.4	Conclusions . . . . .	43

<b>5</b>	<b>The First Observation of Zeeman Effect in Photoluminescence of Si:Er</b>	<b>45</b>
5.1	Introduction . . . . .	45
5.2	Experimental details . . . . .	47
5.3	Results and discussion . . . . .	48
5.4	Conclusions . . . . .	53
<b>6</b>	<b>Microscopic Structure of a Single Type of Optically Active Center in Si/Si:Er Nanostructures</b>	<b>55</b>
6.1	Introduction . . . . .	55
6.2	Sample preparation and experiment . . . . .	57
6.3	Photoluminescence . . . . .	59
6.4	Zeeman splitting of the PL lines . . . . .	63
6.4.1	Introduction: theoretical considerations . . . . .	63
6.4.2	Splitting of line $L_1^1$ . . . . .	67
6.4.3	Splitting of line $L_4^1$ . . . . .	68
6.4.4	Splitting of line $L_1^2$ (the hot line) . . . . .	70
6.4.5	Splitting of other spectral components . . . . .	71
6.5	Discussion . . . . .	73
6.5.1	Symmetry considerations . . . . .	73
6.5.2	Consequences for the microscopic model of the Er-1 center . . . . .	75
6.6	Summary and conclusions . . . . .	78
<b>7</b>	<b>Optical Properties of the Er-1 Center: A Candidate for Realization of Optical Gain in Si:Er</b>	<b>79</b>
7.1	Introduction . . . . .	79
7.2	Experimental details . . . . .	82
7.3	Results and discussion . . . . .	83
7.4	Conclusions . . . . .	91
	<b>Appendix</b>	<b>91</b>
<b>A</b>	<b>Specific Aspects of Er Excitation Across the Bulk of a Si Wafer</b>	<b>93</b>
A.1	Introduction . . . . .	93
A.2	Experimental details . . . . .	94
A.3	Effect of electrical bias on PL delay time . . . . .	94
A.4	Excitation cross section of erbium in silicon . . . . .	97
<b>B</b>	<b>The Effects of Stress and Magnetic Fields</b>	<b>101</b>
	<b>References</b>	<b>103</b>

---

<b>Summary</b>	<b>115</b>
<b>Samenvatting</b>	<b>117</b>
<b>Acknowledgements</b>	<b>121</b>
<b>List of publications</b>	<b>123</b>
<b>Awards</b>	<b>125</b>



# Chapter 1

## Introduction

### 1.1 Optical centers in semiconductors

Recombination resulting from the annihilation of electron-hole pairs in semiconductors is called the photoluminescence (PL). This can be accomplished by a variety of ways. When semiconductor crystals are excited by a laser or other radiation, electrons are removed from the valence band and placed in the conduction band, leaving holes in the valence band. Because of the mutual attraction between the electrons and the holes, these particles can exist as pairs, excitons, which can move throughout the crystal. Free carriers and excitons can be trapped at donors or acceptors in either neutral or ionized states and subsequently recombine. Various electron-hole recombination processes produce an emission spectrum with many different components.

A useful distinction can be made between charged centers, i.e. donor or acceptor, and neutral (or “isoelectronic”) centers. A single donor has one excess electron (such as Si:P), meaning that the defect region has a net positive core charge. Similarly, a single acceptor (such as Si:B) has a net negative localized charge. An isoelectronic center (such as Si:C, Si:Cu) has no net charge in the local bonding region. A hole or an electron can be localized at such a center by a local (core) potential; subsequently, the secondary particle can be captured by Coulomb field into a shallow, effective-mass-theory (EMT) state. The main difference between neutral and charge centers is absence of the long-range Coulomb potential. This simple picture is adequate for single donors, acceptors and isoelectronic centers, but also for complex defects which involve more than one site, such as a pair of substitutional impurities, a substitutional-interstitial pair, a vacancy pair, a vacancy interstitial pair (if one constituent is a shallow donor or acceptor), etc. [1]. There are two systems of symbol which are used in literature to label these luminescence centers; these are given in the Table 1.1

Table 1.1: Common symbols for labelling recombination processes.

Free exciton	X	+−
Donor	D <sup>0</sup>	⊕−
Acceptor	A <sup>0</sup>	⊖+
Exciton bound at neutral donor	D <sup>0</sup> , X	⊕ = +
Exciton bound at ionized donor	D <sup>+</sup> , X	⊕ − +
Exciton bound at neutral acceptor	A <sup>0</sup> , X	⊖ −
Exciton bound at ionized acceptor	A <sup>−</sup> , X	⊖ + −
Exciton bound at isoelectronic center		⊙±
Free electron to acceptor transition	e, A <sup>0</sup>	
Donor to free hole transition	D <sup>0</sup> , h	

In the case of single donors or acceptors the ground state already contains one bound electronic particle, an electron or a hole, respectively. The excited states for these centers can usually be described in the EMT approximation [2, 3] based on the hydrogen-like Coulomb potential. Localization of an exciton to these centers creates the bound exciton (BE) excitation. A BE consists of three carriers (two holes and one electron for acceptor BE, two electrons and one hole for donor BE) bound to a charged impurity, Fig. 1.1 (a,b). Because in a BE three carriers are localized in the same region of real space, an Auger transition, in which an electron recombines with a hole and the energy is carried off by the third carrier, can occur. Auger transitions are believed to limit the lifetimes of BEs in many case.

The isoelectronic centers have no particle localized in the ground state, and the analog to the above-mentioned excitations for the donors/acceptors therefore does not exist. Such centers bind electrons (or holes) by a weak interaction (a strain field, or a local change of electronegativity). The cross section for capture of the first carrier is usually quite small for these centers. Upon localization of the primary particle, the secondary particle, a hole (or an electron) can be captured in Coulomb field of the first particle. This BE state containing two electronic particles associated with the isoelectronic center has usually very well defined electronic energy, corresponding to a sharp emission/absorption line in optical spectra, (if the phonon coupling in the optical transition is not too strong). These systems have been classified as isoelectronic donors and isoelectronic acceptors on the basis of whether the impurity is attractive for holes or electrons, respectively, Fig. 1.1 (c,d).

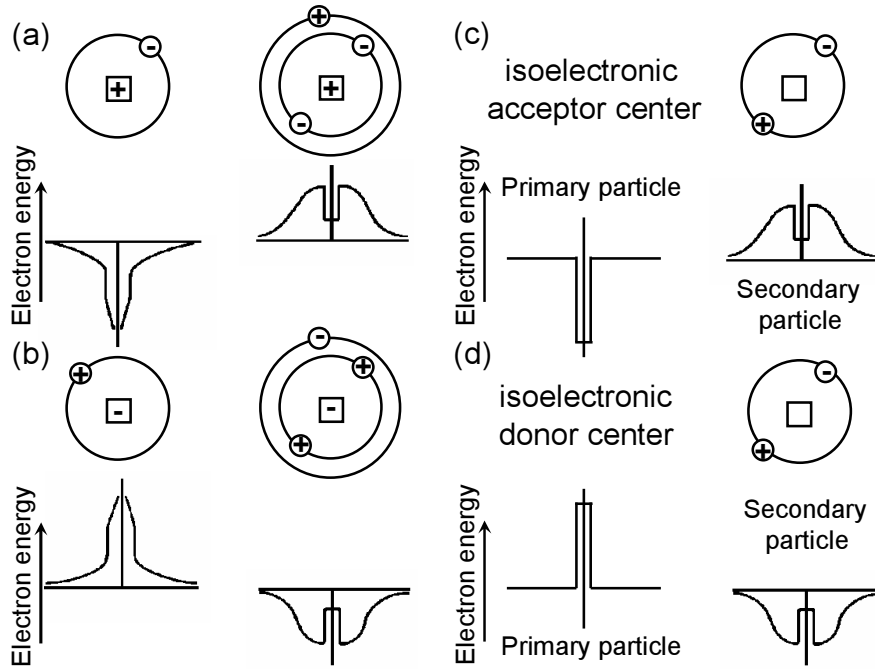


Figure 1.1: *Schematic single particle potentials of the ground state and the BE state (a) for a single donor (b) for a single acceptor (c) to an isoelectronic acceptor (d) to an isoelectronic donor center, after B. A. I. Monemar [1].*

## 1.2 Isoelectronic centers

The radiative decay of excitons bound to isoelectronic impurities is an important physical process in crystalline semiconductors. This is particularly true in indirect band-gap semiconductors like GaP and silicon, in which band-to-band radiative transitions are forbidden by the  $\vec{k}$ -conservation rule. The introduction of isoelectronic impurities into indirect band-gap semiconductors helps to improve the quantum efficiency of optical emission. Emission due to exciton bound to an isoelectronic center is characterized by a long radiative decay time, which indicates stability against nonradiative Auger processes, and high radiative quantum efficiency. The lifetime can be  $\tau > 10^{-5}$  s compared to  $\tau < 10^{-7}$  s for BE at single donors or acceptors. As a result of the relatively weak binding of both electron and hole, the luminescence from the isoelectronic centers usually has the photon energy close to the electronic gap, but considerably less than for an exciton bound to shallow donors or acceptors.

The isoelectronic bound exciton (IBE) emission from silicon has attracted considerable interest in the last few years and has now been observed for Si:S, Si:Be,

Si:In, Si:Tl, Si:Se, Si:Cu, Si:Ag as well as for some unidentified impurities in as-grown silicon [4]. IBEs are also the subject of some technological interest because larger exciton binding potential can lead to intense room temperature emission (for example, N in GaP for green LEDs). Indeed, high internal quantum efficiencies,  $\eta_{int}$ , have been observed [5]. Chalcogen complexes in silicon, in particular sulfur complexes, have the highest reported efficiencies: for S in Si an efficiency of  $\eta_{int} = 2 - 5\%$  has been reported [6].

## 1.3 Silicon photonics

Silicon technology offers almost unlimited possibilities and pervades our everyday life. Silicon chips are in our homes, our cars and sometimes even in people's bodies. Indeed, the scientific literature contains more than 250000 papers relating to silicon. But bulk silicon is extremely inefficient for emitting light, and so could play only a minor role in optoelectronics - the high-speed alternative of electronic circuits. So, to make lasers and high-speed telecommunications devices, more complex semiconductors, such as GaAs, InP,... have been called upon. These are good light emitters but are more expensive than silicon and hard to integrate into silicon microchips. If an all-silicon light emitting device could be created it would lead to new types of optoelectronic devices and also revolutionize the design of supercomputers, among others.

Optical doping is an attractive method to tailor photonic properties of semiconductor matrices for development of solid state electroluminescent structures. In particular, rare earth (RE) and transition metal (TM) ions are frequently used for optical doping of semiconductor matrices. In this way, attractive systems are formed, which combine atomic-like properties of dopants with band structure of the host material.

### 1.3.1 Si:Ag, Si:Cu

There has been a great deal of recent interest in a number of long lifetime, impurity related photoluminescence lines observed in samples of crystalline silicon. It is thought that all of these lines arise from the recombination of excitons bound to various complex isoelectronic centers. The electronic structure of the optically active Cu (or Ag)-related center in silicon was confirmed to be well described by a model of an exciton bound to an isoelectronic center. This was evidenced by the temperature-dependence of luminescence, the time-resolved measurements, and Far-infrared (FIR) absorption spectrum. The electronic level scheme of the exciton bound to the isoelectronic center was developed. In that way, for the case

of copper and silver in silicon, an estimate of the thermal ionization energy of an electron from the effective-mass-state of 33 meV has been given.

### 1.3.2 Si:Er

Rare earth doping of Si is known to result in the formation of luminescent centers and is considered as a promising way to improve photonic properties of silicon. Among the various rare earth elements, Er is of special interest since its atomic transition in the 1.5  $\mu\text{m}$  range coincides with the optical window of glass fibers currently used for telecommunications. Devices based on Si:Er system can be easily integrated within the highly successful standard silicon technology. Luminescence at this wavelength from Er-implanted Si was already observed several years ago [7]. Meanwhile Er-based light-emitting diodes operating at room temperature have been reported. The basic understanding of Er luminescence in Si, however, is far from complete. While impact with hot carriers is responsible for generation of efficient electroluminescence in reverse-biased diodes, localization or collisions with excitons at Er-related donor centers is a generally accepted mechanism of low temperature photoluminescence in crystalline Si:Er. The Auger process of exciton recombination with a simultaneous energy transfer to the  $4f$ -electron shell of the  $\text{Er}^{3+}$  ions has been modeled theoretically, but it has not been unambiguously supported by experiment, all evidence in its favor being of an indirect nature.

## 1.4 This thesis

In this thesis fundamental investigations of excitation and de-excitation processes of isoelectronic centers in crystalline silicon are described. The studies are carried out by means steady-state and time-resolved photoluminescence, photoluminescence excitation spectroscopy, two-color spectroscopy using a free-electron laser, and magneto-optical measurements.

The details of experimental techniques are discussed in Chapter 2. In Chapter 3, we report the results of a detailed study of optical properties of a silver-related center in silicon. Perturbations of optical transitions by uniaxial stresses and magnetic fields have been accurately described. With the developed energy-level scheme, the total luminescence and the radiative decay time have been fitted over the temperature range 4 – 50 K. It has been shown that from the data an estimate can be given for the time necessary to thermally ionize an electron from the EMT state. Using another isoelectronic center created by Cu dopant of silicon - Chapter 4, we have demonstrated that by two-color spectroscopy ionization cross section can be determined for centers of an unknown concentration. Further, we have pre-

sented evidence of a recapture of charge photo-ionized from the Cu-related center. In Chapters 5 and 6, we provide the most direct microscopic information on the structure of a prominent center responsible for optical activity of Er in crystalline silicon. We present specific results of a magneto-optical study of multilayer Si/Si:Er structures grown by sublimation molecular beam epitaxy technique. We show that the presence of Si spacer regions considerably increases emission intensity when compared to single layers. The PL from annealed multilayer structures is dominated by emission from the particular center, the Er-1 center, which is then preferentially formed. The PL spectrum of this center is characterized by ultra narrow, homogeneous lines. From analysis of Zeeman effect clearly observed on the main line of the Er-1 PL spectrum, the lower-than-cubic symmetry of the emitting center is conclusively identified as orthorhombic- $I$  ( $C_{2v}$ ). Based on this analysis, we propose that the microscopic structure of the Er-1 center comprises a single  $\text{Er}^{3+}$  ion at a distorted interstitial  $T_d$  site with multiple oxygen atoms in its direct vicinity. Subsequently, a detailed consideration of excitation mechanisms of the Er-1 center, carried out under cw and pulsed laser pumping, is made in Chapter 7. The overall excitation cross section and the total number of optically active  $\text{Er}^{3+}$  ions present in Si/Si:Er nanolayers have been evaluated.

Finally, in Appendix A, we briefly discuss the role of exciton diffusion in the excitation process of Er in Si.

# Chapter 2

## Experimental Techniques

*This chapter concerns instrumental and experimental details of photoluminescence spectroscopy, time-resolved measurements, photoluminescence excitation, two-color spectroscopy and magneto-optical measurements used in the investigations described in this thesis.*

### 2.1 Photoluminescence and time-resolved experiments

Photoluminescence (PL) is the spontaneous emission of light from a material under optical excitation. The excitation energy and intensity can be chosen to probe different excitation types and also different parts of the sample. PL investigations can be used to characterize a variety of materials parameters. Features of the emission spectrum can be used to identify surface, interface, and impurity levels... Under pulsed excitation, PL intensity transients yield lifetimes of excited states. In addition, thermally activated processes of non-radiative recombination cause changes of PL and can be investigated in this way.

PL analysis is nondestructive. The technique requires very little sample manipulation or environmental control. When light of sufficient energy is incident on a material, photons are absorbed and (electronic) excitations are created. These excitations relax and the system returns to the ground state. The PL can be collected and analyzed to provide information about the photo-excited states. The PL spectrum reveals transition energies. The PL intensity gives a measure of the relative rates of radiative and non-radiative recombinations. Variation of the PL intensity upon change of external parameters, e.g., temperature, can be used to further characterize electronic states and bands.

The typical PL experimental set-up used in our laboratory is illustrated in Fig.

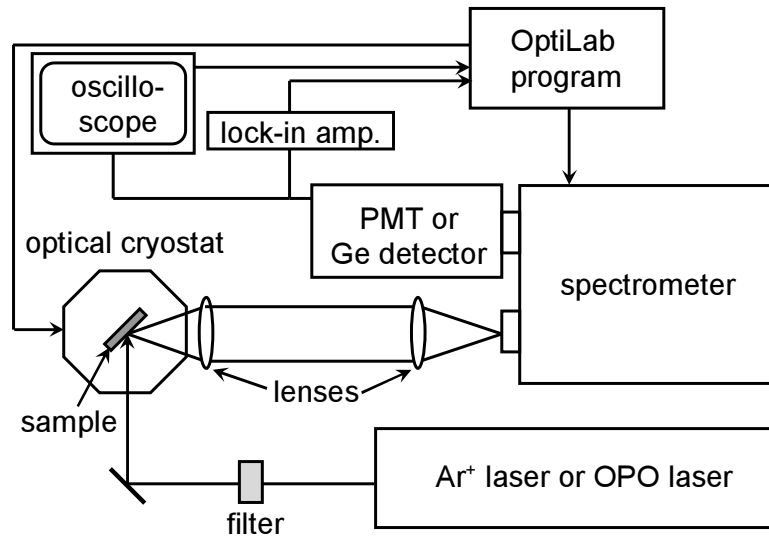


Figure 2.1: *Typical experimental set-up for PL measurements*

2.1. The PL experiments were carried out in a variable temperature continuous-flow cryostat accessing the 1.5 – 300 K range (Oxford Instruments Optistat CF). The samples were excited using a continuous-wave (cw) argon-ion laser operating at 514.5/488/351 nm, or a tunable Optical Parametric Oscillator (OPO) laser system, producing pulses of 5 ns duration at 20 Hz repetition rate. The luminescence was resolved with a 1 m F/8 monochromator (Jobin-Yvon THR-1000) equipped with a 900 grooves/mm grating blazed at 1.5  $\mu\text{m}$  and detected by a high sensitivity germanium detector (Edinburgh Instruments) or a Hamamatsu R5509-72 InP/InGaAs nitrogen-cooled photomultiplier tube.

Time-resolved measurements were carried out using a Tektronix TDS 3000 digital oscilloscope in combination with the Hamamatsu detector. The experimental response time of the system was  $\tau_{dec} \approx 3$  ns for the Hamamatsu detector at 50  $\Omega$ ;  $\tau_{dec} \approx 350$  ns at 1 k $\Omega$ ;  $\tau_{dec} \approx 35$   $\mu\text{s}$  at 100 k $\Omega$  and  $\tau_{dec} \approx 400$   $\mu\text{s}$  at 1 M $\Omega$ . The PL response could be integrated in time using a digital oscilloscope (TDS 3032, Tektronix). In the cw mode, excitation modulation was achieved by using a pinhole and chopping the laser beam mechanically at 200 Hz. In these cases, the PL spectrum was recorded by using a lock-in amplifier. The time resolution was measured as 15  $\mu\text{s}$  using 1 k $\Omega$  setup.

A program called “OptiLab” was developed for remote operation of the experimental setup. The program uses a GPIB card and a serial port (RS-232) to control: the high resolution spectrometer, variable temperature cryostat, lock-in amplifier, ADC and laser. The software was written in C language and CVI program under Windows environment.

## 2.2 Photoluminescence excitation spectroscopy

In PL spectroscopy, which is performed at a fixed excitation energy, the luminescence properties are generally investigated, while photoluminescence excitation spectroscopy (PLE), which is carried out at a fixed detection energy, provides mainly information about the absorption properties and probes excited states of optical centers. In this experiment, the sample is excited by photons of the energy  $h\nu$  tuned to be absorbed by specific optical centers. Therefore, this technique requires a tunable excitation source. In our setup, for this purpose the OPO has been used. Its emission wavelength can be tuned in wavelength range (400 nm to 2200 nm). The high resolution PLE, i.e., the combination of highly resolved PL spectra as a function of the well-defined excitation energy ( $\Delta E \approx 1\text{meV}$ ), provides detailed information about the system under investigation.

## 2.3 Two-color spectroscopy

Shallow excited states in semiconductor can be conveniently investigated by two-color spectroscopy. In these experiments, one beam with sufficient quantum energy is used to create a large population in the excited state. The second mid-infrared “probe” beam (with the photon energy of the order of 10 to few hundred meV) is used to induce transitions within the excited state of the system.

The idea of the two-color mid-infrared (2C-MIR) experiments is presented in a cartoon in Fig. 2.2. The pump beam from the second harmonic of a Nd:YAG laser (532 nm) with a repetition rate of 5 Hz and a pulse duration of 100 ps provides band-to-band excitation leading to emission from the optical dopant. A mid-infrared (MIR) probe pulse with duration of  $\sim 5 \mu\text{s}$  is provided by a free-electron laser (FEL). The FEL can be activated with a selected time delay  $\Delta t_F$  with respect to the Nd:YAG laser pulse and its wavelength is tunable. Measurements are carried with the sample fixed on the cold finger of a flow cryostat in a variable temperature range from 4.2 to 300 K. This technique is very useful for tracking energy transfer paths of optically doped semiconductor matrices, for ionization of shallow centers, and for investigation of thermally activated recombinations.

The two-color experiments described in this thesis (Chapter 4) have been performed at the Dutch Free Electron Laser facility for Infrared eXperiments (FELIX) at the FOM Institute for Plasma Physics “Rijnhuizen” in Nieuwegein [8]. The user facility provides continuously tunable radiation in the spectral range of 4 – 250  $\mu\text{m}$ , at peak powers up to 100 MW in a (sub)picosecond pulse. The infrared beam features short micropulses, which have a nominal duration of 1 ps and are separated by intervals of either 1 ns (1 GHz) or 40 ns (25 MHz), - see inset to Fig.

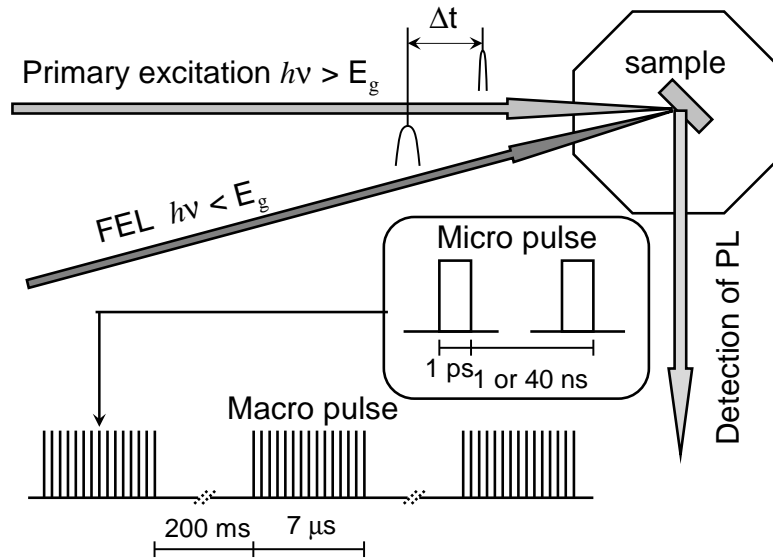


Figure 2.2: *Experimental configuration for low-color experiments. The band-to-band excitation is provided by a second harmonic of a ND:YAG laser. The MIR beam is provided by FEL.*

2.2. The micropulses form a train with a total duration of up to  $10 \mu\text{s}$ .

## 2.4 Magneto-optical spectroscopy

This technique comprises a simultaneous application of an optical excitation and a magnetic field, and is generally named Zeeman spectroscopy. It can be very informative in case when narrow spectral lines are observed in optical transitions. The usual requirement is for the sample to be at a low temperature and in a high magnetic field with good optical access, so that it can be excited with laser radiation and luminescence can be collected for analysis with a high resolution spectrometer. Upon application of magnetic field, a splitting of individual PL bands will occur. The details of this splitting, multiplicity and  $g$  factor for each particular transition, provide information on orbital angular momentum and spin of the center. The necessary condition is that the magnetic field must be such that the linear Zeeman term  $H = \mu_B \cdot g_{eff} \cdot \bar{S}_{eff} \cdot B$  is significantly larger than the natural linewidth observed. In experimental practice, magnetic fields of 5 T or higher from a superconducting magnet are used.

The magneto-optical setup available in our laboratory is shown in Fig. 2.3. The magnet with optical access (Spectromag 8) up to 6 T is immersed in liquid helium. The samples are excited by radiation from an  $\text{Ar}^+$  ion laser operating at

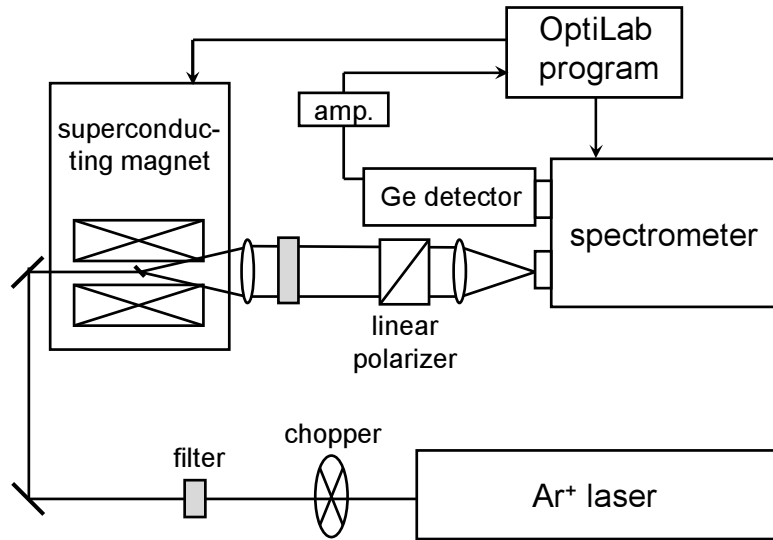


Figure 2.3: *Diagram of a magneto-optical spectrometer which is suitable for magneto emission studies. It consists of, mainly, a superconducting magnet, a high resolution spectroscopy, a laser, a  $\lambda/4$  plate and a linear polarizer*

514.5 nm, and the luminescence is analyzed with a 1.0 m or 1.5 m F/8 high resolution monochromator (Jobin-Yvon THR-1000/THR-1500 equipped with a 900 grooves/mm grating blazed at 1.5  $\mu\text{m}$ ) and detected by a high sensitivity germanium detector (Edinburgh Instruments). Temperature of the samples was varied from 1.5 – 300 K. The experimental setup is operated by remote control since access to the magnet room is usually restricted when the magnet is in operation.

For experiments, different geometries may be used: with  $\vec{k} \parallel \vec{B}$ , Faraday configuration, gives PL of circular polarization  $\sigma^+$  and  $\sigma^-$ , the Voigt configuration,  $\vec{k} \perp \vec{B}$ , yields polarization  $\sigma$  and  $\pi$  (Here  $\vec{k}$  is propagation vector of the light). The polarization is very important, because most of the optical transitions are polarized according to the corresponding optical selection rules. The analysis of circular polarized light can be made by using a  $\lambda/4$  plate and a linear polarizer.



# Chapter 3

## Optical Properties of a Silver-Related Defect in Silicon

*Doping crystalline silicon with silver results in a photoluminescence center with multiplet no-phonon structure near 778.9 meV. We show that the published assignments of the vibronic sidebands are wrong, with severe implications for the relative transition probabilities of the luminescence transitions from the excited states. At low temperature, most of the luminescence intensity derives from the phonon sideband associated with a forbidden no-phonon line through the phonon-assisted coupling of two of the excited states of the center. The effective mass of the vibration is determined from isotope effects to be close to the mass of one Ag atom. Uniaxial stress and magnetic perturbations establish that the current assignment of the electronic structure of the center is incorrect and that it is best described by a new variant on the “pseudodonor” model. An electron orbits in an effective  $T_d$  environment, with an orbital triplet as its lowest-energy state, giving a  $j = 3/2$  electron state. A tightly bound hole has its orbital angular momentum quenched by the  $C_{3v}$  symmetry of the center, leaving only spin angular momentum ( $s = 1/2$ ). These particles couple to give  $J = 2, 1, 0$  states. Using this model, the temperature dependence of both the total luminescence intensity and measured radiative decay time can be understood. These data allow an estimate to be made of the thermally induced transition rate of the electron from the effective-mass excited states into the conduction band.*

### 3.1 Introduction

It is well established that the photoluminescence (PL) of many optical centers in crystalline silicon can be described in terms of the recombination of an electron and a hole at an electrically neutral center. Usually, one of these particles is

tightly bound and the other is loosely bound. With increasing temperature, the luminescence from the centers is always quenched. However, within this generic model there is considerable diversity. The activation energy for the luminescence quenching may be equal to the binding energy of the loosely bound particle (e.g., the well-known 1014-meV Cu-related luminescence [9]), that of the tightly bound particle (e.g., the 968-meV Cu-S center [10]), that of the binding energy of the exciton to the center (e.g., the  $I_2$  boron-related center [11]), or it may equal the binding energy of the free exciton (e.g., the W center [4]). The tightly bound particle may be the electron, with the loosely bound hole maintaining its orbital angular momentum, but being split into a doublet of nearly equal transition strengths (e.g., the 935-meV  $C$ -related center [12]). Alternatively, the hole may be tightly bound, quenching its orbital angular momentum and leading to spin-triplet, spin-singlet states (e.g., the  $Q$  Li-related center [13]) with a doublet no-phonon structure of one almost forbidden line and one allowed transition. The relative strengths of transitions from these “triplet” and “singlet” states can be predicted simply from the effect on the valence-band maxima of the field binding the hole [14]. In all these cases the lowest-energy electron state is an  $A_1$  state derived from the conduction-band minima.

Many centers can be produced by doping crystalline silicon with silver, as shown by Refs. [15, 16, 17, 18, 19, 20, 21, 22, 23, 24] and the work cited therein. Electrical properties of silver in silicon were extensively studied and a number of Ag-related deep levels have been reported [15, 16]. In a deep level transient spectroscopy (DLTS) study, Baber *et al.* [17] reported that silver creates an acceptor at  $E_c - 0.54$  eV and a donor level at  $E_v + 0.34$  eV. From the Fano structure of the ionization continuum of the center, it was deduced that the transitions occurred at a deep donor [21], later refined to be a “pseudodonor” (i.e., an electrically neutral center where an effective-mass electron can orbit in the Coulomb field of a tightly bound hole) [24]. Silver-doped silicon was also thoroughly studied by electron paramagnetic resonance (EPR); following analysis of the EPR spectra, microscopic models of several Ag-related centers were proposed [18, 20].

The PL of silver-doped silicon has been investigated [21, 22, 23, 24, 25, 26, 27, 28, 29, 30, 31]. It has been found that silver doping of silicon crystals results in generation of a characteristic low-temperature emission spectrum at 780 meV [22, 25, 26]. In the PL spectrum narrow no-phonon lines (termed  $A$ ,  $B$ , and  $C$ ) and lower energy phonon replicas have been distinguished. The observed structure was identified as transitions from the effective-mass-like electronic states near the conduction band to the ground state. At temperatures below 8 K, the spectrum was dominated by two no-phonon lines  $A$  and  $B$  with energies of 778.91 and 779.85 meV, respectively [26]. Both lines produced phonon replicas with local

phonon energies of approximately 6 and 15 meV. At energies of 20.7 and 33.1 meV below the  $A$  line, two broad features were observed and assigned to the transverse-acoustic (TA) and longitudinal-acoustic (LA) silicon phonon replicas, respectively. At higher temperatures a third no-phonon line  $C$ , appeared at 784.31 meV. The intensity of this line rapidly increases with temperature while the intensities of the  $A$  and  $B$  lines decrease and the  $A-B-C$  system thermalizes [25]. At temperatures higher than 20 K some local phonon replicas of the  $C$  line were also observed.

In this Chapter we examine the multiple-excited state structure of one center. We will show that it can be described by using another variant on the bound-exciton model. The lowest-energy states consist of an effective-mass electron in a *triply degenerate* orbital state and a tightly bound hole. The response of the electron to external perturbations is determined by its effective  $T_d$  environment, while the response of the hole is that of a nondegenerate orbital state at a center of trigonal symmetry. The low-symmetry environment of the hole quenches its orbital angular momentum, and spin-spin coupling dominates in the interaction of the electron and hole. We will show that these states interact so as to produce a very unusual vibronic structure and that the changes in luminescence intensity of the band, as functions of both temperature and secondary excitation, can be understood using the model for the electronic states.

At low temperature, most of the PL intensity derives from the phonon sideband associated with a *forbidden* no-phonon line (Sec. 3.3). The responses of the excited states to uniaxial stress and magnetic field perturbations are presented in Sec. 3.5. The large splitting of line  $C$  under uniaxial stress establishes that the excited state should be assigned to a  $T_2$  effective-mass orbital state in  $T_d$  symmetry, rather than the current assignment to an  $A_1$  orbital. We show that the low-symmetry environment of the hole quenches its orbital angular momentum and spin-spin coupling dominates in the interaction of the electron and hole. The mechanism through which the vibronic sideband is produced is presented in Sec. 3.6, and by using isotope data to estimate the effective mass of the vibration, it is shown to be consistent with the perturbation data. Knowing the electronic structure, the temperature dependence of both the total PL intensity and the measured radiative decay time can be understood, and we make a first estimate of the transition rate for thermal quenching of a “pseudodonor” in silicon (Sec. 3.7). We begin by presenting the experimental method and preparation of the samples.

## 3.2 Experimental details

Silver-doped silicon samples for the present study were prepared from 75-125  $\Omega\text{cm}$  p-type float-zone silicon by diffusion. Thin silver layers were evaporated on both

sides of the silicon samples. The diffusion was performed for 4h at 1150 °C in a closed quartz ampoule containing 100 mbar of argon. Following the diffusion step, the samples were quenched to room temperature by dropping the whole ampoule in water. After diffusion, the surface layers were etched to remove about 70  $\mu\text{m}$  in a mixture of HF and  $\text{HNO}_3$  (1:3). For the diffusion, both natural and isotopically enriched silver (99.5 % and 99.4 % of  $^{107}\text{Ag}$  and  $^{109}\text{Ag}$  isotopes, respectively) was used.

The PL experiments were performed with a variable temperature continuous-flow cryostat accessing the 1.5 – 300 K range (Oxford Instruments Optistat CF). The samples were excited using a cw argon-ion laser operating at 514.5 nm. All spectra were obtained with a 1.5 m F/12 monochromator (Jobin-Yvon THR-1500) and detected by a high-sensitivity germanium detector (Edinburgh Instruments). Uniaxial stress measurements were carried out at temperatures from 4.2 up to 20 K and with stresses up to 200 MPa. For the Zeeman measurements, the magnetic field was varied from 0 up to 4.5 T.

Time-resolved measurements were carried out using a Tektronic TDS 3000 digital oscilloscope in combination with a Hamamatsu R5509-72 InP/InGaAs nitrogen-cooled photomultiplier tube. For the lifetime data of Sec. 3.7, transient excitation was achieved by using a pinhole and chopping the laser excitation beam mechanically at 200 Hz. The system response time was measured as 35  $\mu\text{s}$ .

### 3.3 Structure of the luminescence band

Usually, as the temperature decreases, the no-phonon line of a band increases in intensity relative to the vibronic sideband. Figure 3.1 shows that between 25 and 1.6 K the line  $A$  weakens relative to the phonon sideband. Line  $A$  is evidently not the no-phonon line of the low-temperature band, in contrast to the assignments by Refs. [26, 28]. Below 2 K a very weak line  $F_0$  is resolved at 778.6 meV, 0.25 meV below  $A$ , as shown in the enlarged inset to Fig. 3.1. The ratios of the phonon sidebands  $F_1$  and  $F_2$  are temperature independent, Fig. 3.1, demonstrating that they derive from the same initial state. Their associated no-phonon line is established by the data in Fig. 3.2, where we show the variations with temperature of the intensity ratios of  $A$  to  $F_1$  and of  $A$  to  $F_2$ . Both ratios follow Arrhenius behavior, with activation energies, respectively, of  $0.26 \pm 0.02$  and  $0.26 \pm 0.3$  meV, equal to the energy separations of the no-phonon lines  $A$  and  $F_0$ . The no-phonon line associated with the sidebands  $F_1$  and  $F_2$  is therefore  $F_0$ , not the stronger  $A$ . Similarly, the ratio of  $C$  to  $F_1$  has an activation energy of  $5.8 \pm 0.9$  meV, equal to the spectroscopic splitting of  $F_0$  and  $C$  (5.7 meV). From the data in Fig. 3.2, the intensity ratio of lines  $C$  and  $A$  extrapolated to infinite temperature is

$I_C/I_A = 21 \pm 6$ , similar to the value of 28 measured directly from the ratio of  $I_C/I_A$  by Iqbal *et al* [25]. We also agree with their result that  $I_B/I_A = 0.7 \pm 0.05$ .

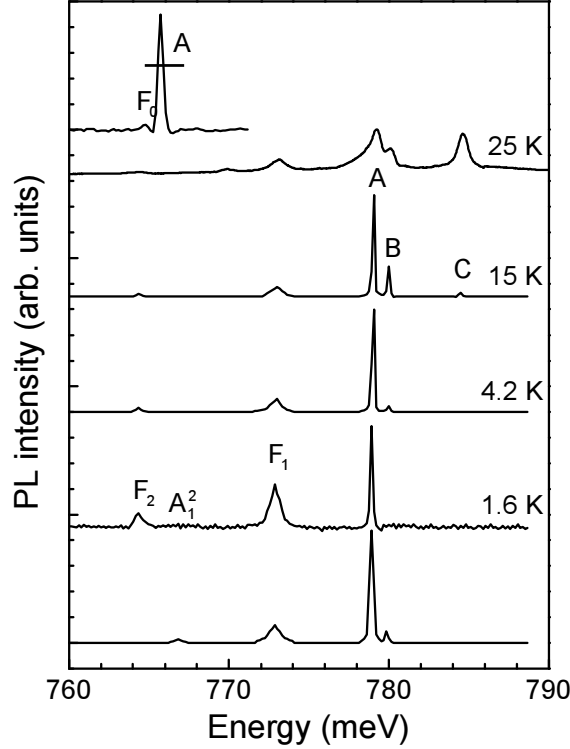


Figure 3.1: The upper four spectra show PL spectra of the 779-meV center in silicon measured at 1.6, 4.2, 15, and 25 K. Two one-phonon resonance modes, labeled  $F_1$  and  $F_2$ , are observed. The no-phonon line A weakens relative to  $F_1$  and  $F_2$  on cooling from 4.2 to 1.6 K. The inset at the top shows an enlarged (and shifted) spectrum of the A and  $F_0$  lines at 1.6 K. The marker is 1 meV long. The lowest curve shows the luminescence spectrum calculated as in Sec. 3.6 and for 4.2 K. The peaks are simulated using Lorentzian line shapes with the widths as determined from experiment and the intensities calculated with the parameters that give the best fit to the energy levels. In the calculation, only the  $F_1$  mode has been considered. The  $F_2$  mode would be produced by the same process as for  $F_1$ .

By extrapolating the measured ratios to infinite temperature, the total transition probabilities in the  $F$  bands ( $F_1 + F_2$ ) relative to A, B, and C are

$$I_F/I_A = 0.68 \pm 0.04, \quad I_F/I_B = 1.0 \pm 0.1, \quad I_F/I_C = 0.032 \pm 0.016. \quad (3.1)$$

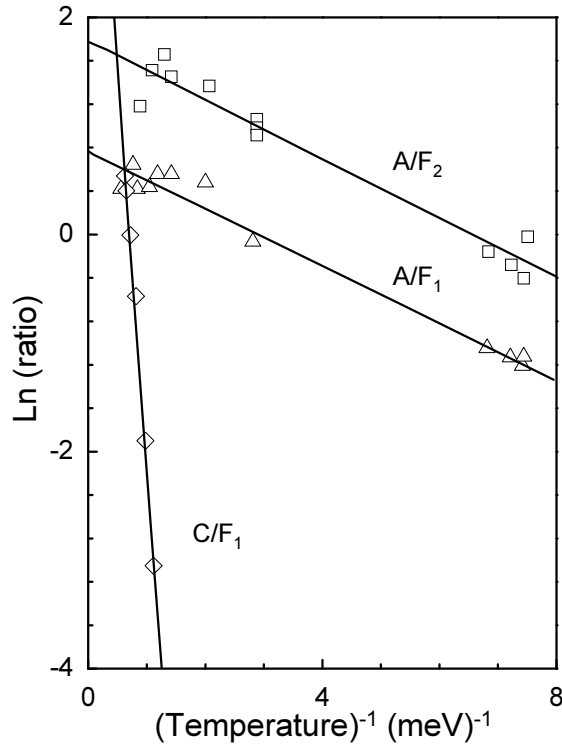


Figure 3.2: Arrhenius plots of the thermal variation of the intensities of line  $A$  relative to  $F_1$  (triangles),  $A$  relative to  $F_2$  (squares), and  $C$  relative to  $F_1$  (diamonds). The activation energy for line  $A$  are  $\sim 0.26$  meV, equal to the spectroscopic separation of  $A$  from the “forbidden” line  $F_0$ . The activation energy for line  $C$  is  $\sim 5.8$  meV, equal to the spectroscopic splitting of  $F_0$  and  $C$ .

The phonon energies of the well-defined sidebands  $F_1$  and  $F_2$ , measured from the no-phonon level  $F_0$ , are, respectively,  $\hbar\omega_1 = 5.8$  meV and  $\hbar\omega_2 = 14.6$  meV. The spectra of Fig. 3.1 show no discernible contributions to the sideband arising from line  $B$ . Lines  $A$  and  $F_0$  are sufficiently close that their phonon sidebands would not be separately resolved. To place an upper limit on the strength of coupling of  $A$  to the 5.8-meV mode, let us suppose that the  $A$  transitions contribute a fraction  $f$  to the phonon sideband  $F_1$ , with the remainder arising from  $F_0$ . Then the ratio of  $I_A/(1-f)I_{F_1}$  should obey a Boltzmann ratio with an activation energy equal to the separation of the lines  $A$  and  $F_0$ . Taking account of experimental uncertainties, a maximum of 15% of the transition from level  $A$  can go to the one-phonon line  $F_1$ , so that to a good approximation transition  $A$  does not couple to *one* quantum of the 5.8-meV mode. The dominant luminescence at low temperature is therefore associated with an essentially forbidden line  $F_0$ . The peak at 767.2 meV, labeled  $A_1^2$  in Fig. 3.1, is assigned to a *two-phonon* assisted transition of the 5.8-meV

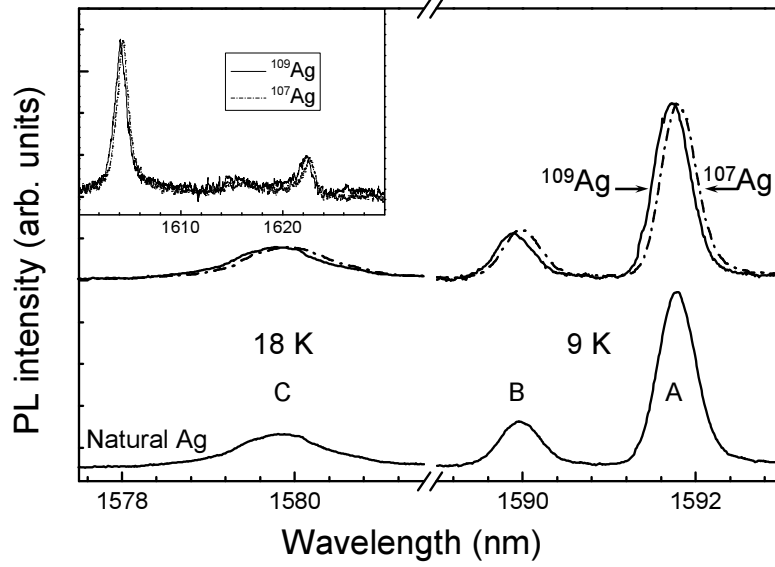


Figure 3.3: *PL spectra recorded from samples doped with single isotopes of  $^{107}\text{Ag}$  or  $^{109}\text{Ag}$ . The main figure shows the effects on the lines A, B, and C in silicon doped with isotopically enriched silver (upper curves) and natural silver (lower curve). The inset shows the effect on the one-phonon lines  $F_1$ ,  $A_1^2$ , and  $F_2$ .*

mode and line A. The mechanism producing these vibronic effects is presented in Sec. 3.6.

### 3.4 Isotope effects

Figure 3.3 compares the high-resolution PL spectra of the 780-meV band recorded for three samples: doped with silver isotope  $^{107}\text{Ag}$ , silver isotope  $^{109}\text{Ag}$  and natural silver (52%  $^{107}\text{Ag}$  + 48%  $^{109}\text{Ag}$ ). While all three spectra show a similar  $A - B - C$  structure, the linewidth for samples doped with a single silver isotope is smaller and the position of lines is shifted by  $\sim -0.017$  meV for  $^{107}\text{Ag}$ -doped silicon and by  $\sim +0.017$  meV for  $^{109}\text{Ag}$ -doped silicon. Also related shifts of the phonon satellites were observed. We note that the  $A - B - C$  lines in the sample containing natural silver are somewhat broader than those observed for  $^{107}\text{Ag}$  or  $^{109}\text{Ag}$  doping. The temperature dependence of the  $A - B - C$  lines in the samples doped with the monoisotopic silver was found to be in agreement with the earlier report [25]. The no-phonon shifts could be caused by different lattice strains, but taken together with the significantly greater one-phonon shifts, the data unambiguously demonstrate the presence of at least one Ag atom in the

optical center.

Isotope shifts of luminescence lines are convenient for identification of the chemical nature of such centers [9]. Heine and Henry [32] gave a quantitative description of isotope shift of no-phonon optical transitions at defects in semiconductors. If the force constant in the initial and/or final electronic state will change on isotopic substitution, an isotope splitting of the no-phonon optical transition will result. In their model, the shift of the no phonon energy  $S$  is related to a softening effect of the electron and hole on the modes of the perfect lattice. When the force constants between the atoms change, the state of the electronic system alters. The effect is related to the temperature dependence of the band gap of the pure material. The presence of a carrier  $c$  ( $c = e$  for an electron and  $c = h$  for a hole) on an atom lowers the interatomic elastic constant  $\Lambda$  by a fraction  $\gamma_c P_c$ :

$$\Lambda' = \Lambda[1 - \gamma_c P_c], \quad (3.2)$$

where  $P_c$  is the probability of the carrier being at the impurity atom and  $\gamma_c$  is the effect of the carrier.

The sum of the effects of a free  $e - h$  pair  $\gamma = (\gamma_e + \gamma_h)$  can be found from the temperature dependence of the band gap energy. At temperatures well above the Debye temperature this is given as [33]:

$$-\frac{dE_g}{dT} = \frac{3}{4}k(\gamma_e + \gamma_h), \quad (3.3)$$

where  $T$  denotes temperature and  $k$  is Boltzmann's constant. From analysis of the data for several defects, Heine and Henry concluded that

$$\gamma_h = (3.6 \pm 1.0)\gamma_e. \quad (3.4)$$

The presence of either a hole or an extra electron will soften lattice modes, the effect of a hole being significantly larger than that of an electron. The total value of the isotope shift can then be given by [32]:

$$S = \frac{2\hbar\omega_D}{5} \left(\frac{M_0}{M}\right)^{1/2} \frac{\Delta M}{M} \frac{\gamma_c}{\gamma} \left(-\frac{dE_g}{dT}\right)_{HT} P_c, \quad (3.5)$$

In Eq. 3.5  $\omega_D$  is Debye cutoff frequency, (for silicon  $\hbar\omega_D = 55.6$  meV),  $M_0$  is the atomic mass of a host semiconductor,  $M$  is the mass of a particular impurity atom ( $M \approx 108$  for silver with natural isotopic composition) and  $\Delta M$  is the mass difference introduced by isotope substitution:  $\Delta M = \pm 1$  for  $^{109}\text{Ag}$  and  $^{107}\text{Ag}$  impurities, respectively.

In order to calculate  $P_c$ , one must determine the wave function of the carrier bound to the defect center in either the initial or the final state (or both). Assuming

that the 780-meV band originates from recombination at an isoelectronic center with a local hole binding potential [21], we roughly estimate the probability  $P_c$  to be about 1. Further, we take  $dE_g/dT$  for silicon to be  $-2.1k$  at room temperature [34], and from Eq. 3.3 we have

$$\gamma_e + \gamma_h = 2.8. \quad (3.6)$$

Finally, substituting the mentioned values into Eq. 3.5 we evaluate the difference in no-point energy to be:

$$S = 0.015 \pm 0.001 \text{ meV}, \quad (3.7)$$

in good agreement with the experimentally measured value of 0.017 meV.

### 3.5 Perturbations of the no-phonon lines by magnetic and stress fields

The effects of magnetic fields on the lower-energy lines were measured at 4.2 and 20 K by PL (Fig. 3.4) and by optical absorption at 4.2 K for the higher-energy transitions near 796 meV (Fig. 3.5). Line  $C$  is not affected by the field. The effects of uniaxial stresses are shown for the lower-energy lines in Fig. 3.6, using luminescence at 4.2 and 20 K to enhance these low-energy transitions, and in Fig. 3.7, using absorption measurements to monitor also the higher-energy states.

The magnetic perturbations are isotropic within measuring accuracy and so contain no information about the point group of the center. This result supports the proposal that the hole is tightly bound [24], because then its orbital angular momentum is quenched, leaving only its spin angular momentum, which responds isotropically to the magnetic field at the resolution available optically.

The effects of stress are most easily seen for line  $C$  (Figs. 3.6 and 3.7). The line splits under  $\langle 001 \rangle$  stress at the rate of  $79 \pm 62$  meV/GPa, similar to the splitting of the conduction-band minima (92.5 meV/GPa, Ref. [35]), while there is little splitting under  $\langle 111 \rangle$  stress. These results confirm the effective-mass nature of the electron. The electron state is derived from the six conduction-band minima and so transforms as  $A_1$ ,  $E$ , and  $T_2$  states in  $T_d$  symmetry. In a basis set ordered as  $A_1$ ,  $E_\theta$ ,  $E_\epsilon$  and  $T_2^x$ ,  $T_2^y$ ,  $T_2^z$ , these valley orbit states are perturbed under stress

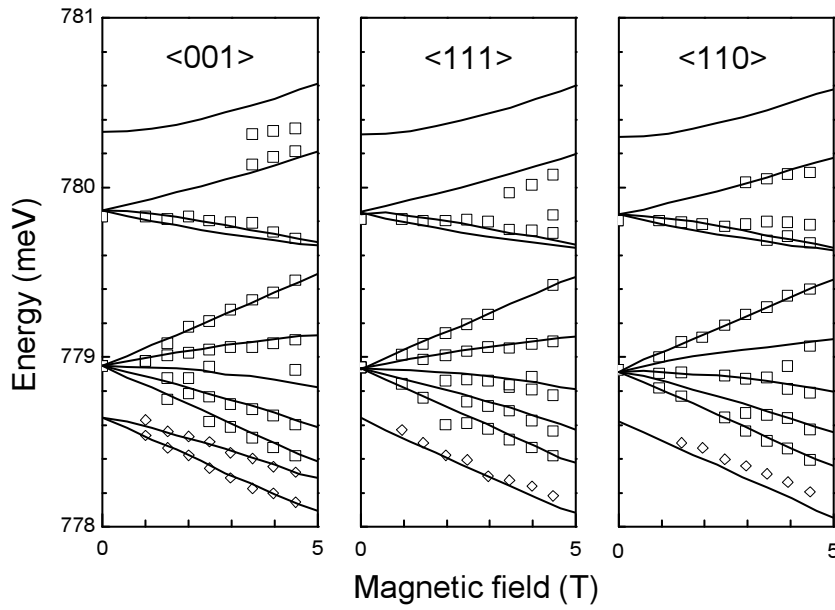


Figure 3.4: The squares show the Zeeman effect measured for the no-phonon lines  $A$  and  $B$ , and the diamonds show transitions induced from  $F_0$ . Line  $C$ , which is not shown, does not shift, as expected from the model of Sec. 3.5. The lines are calculated as in Sec. 3.5 with parameters  $\lambda = -0.46$  meV,  $g_S = 1.9 \pm 0.1$ , and  $g_L = 0$ . The lines close to the data for  $F_0$  have been obtained by downshifting the fits to the lowest-energy components of line  $A$ .

according to the symmetric matrix [36]

$$\begin{pmatrix} -\gamma(5 + \delta) & ps_\theta & ps_\epsilon & 0 & 0 & 0 \\ & -Bs_\theta + \gamma(1 - \delta) & Bs_\epsilon & 0 & 0 & 0 \\ & & Bs_\theta + \gamma(1 - \delta) & 0 & 0 & 0 \\ & & & C(\sqrt{3}s_\epsilon - s_\theta) & 0 & 0 \\ & & & & -C(s_\theta + \sqrt{3}s_\epsilon) & 0 \\ & & & & & 2Cs_\theta \end{pmatrix}, \quad (3.8)$$

Here  $6\gamma$  is the energy separation of the  $E$  state from the  $A_1$  state and  $2\delta\gamma$  is the displacement of the  $T_2$  state from  $E$ . The terms  $s_\theta$  and  $s_\epsilon$  are the stress combinations

$$s_\theta = 2s_{zz} - s_{xx} - s_{yy}, \quad s_\epsilon = \sqrt{3}(s_{xx} - s_{yy}),$$

where the stress tensor components  $s_{ij}$  are written in terms of the Cartesian coordinates  $i, j = x, y, z$  of the crystal and compressive stress is defined to be positive. Hydrostatic stress terms, which would appear down the diagonal of the matrix, are omitted (and will be introduced below).

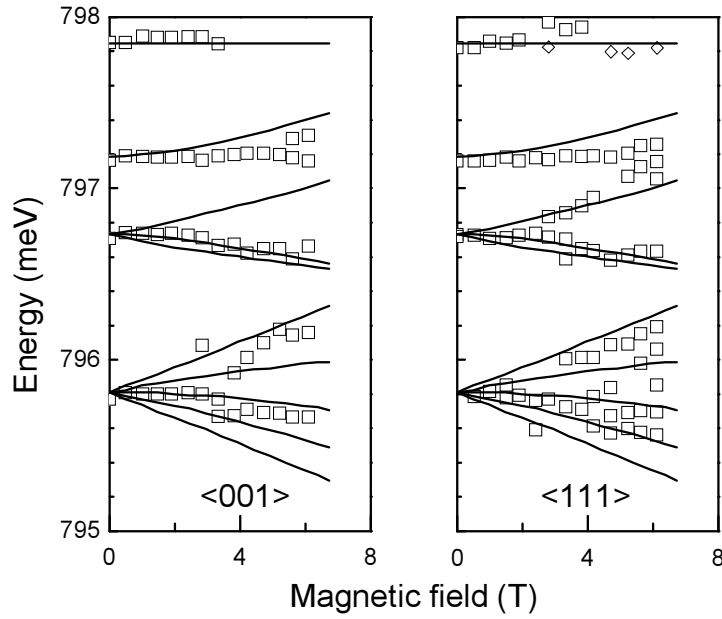


Figure 3.5: Zeeman effect of the higher excited states, labeled as  $1s(E+T_2)$  in Ref. [18], with the magnetic field along  $\langle 001 \rangle$  and  $\langle 111 \rangle$  directions. The squares are the experimental data, and the lines are calculated using the spin-orbit parameter  $\lambda = -0.46$  meV derived from the fit of the Zeeman effect on the lines A and B (Fig. 3.4 and a spin  $g$  factor  $g_s = 1.3$ ). The line at 797.9 meV is assigned to the transition from the singlet state, analogous to line C.

An  $A_1$  state is perturbed only by hydrostatic stresses and by coupling through the terms  $ps_\theta$  and  $ps_\epsilon$  to the  $E$  state, Eq. 3.8. The considerable splitting of line C under  $\langle 001 \rangle$  stress and the linearity of the splitting establishes that C does not have an  $A_1$  state, as is central to existing descriptions of the excited states of the center [21]. Line C derives from the  $T_2$  component of Eq. 3.8.

Under stress, the matrix shows that the  $T_2$  state splits into two components under  $\langle 110 \rangle$  stress and is not split under  $\langle 111 \rangle$  stress. Consequently, to obtain the two components seen in  $\langle 001 \rangle$  stress, two in  $\langle 111 \rangle$ , and at least three in  $\langle 110 \rangle$  stress, the hole must not be split under  $\langle 001 \rangle$  stress and must be perturbed into two states by  $\langle 111 \rangle$  stress and by  $\langle 110 \rangle$  stress. These splittings are only expected for an orbitally nondegenerate state in a trigonal local symmetry [37], which defines the environment of the hole.

Having determined the environment of the electron and hole as independent particles, we now need to consider their interaction. In an isoelectronic model, the ground state of the system is the “vacuum” state with no particles. It therefore has a spin of  $S = 0$ , and optical transitions are only allowed to it from the singlet

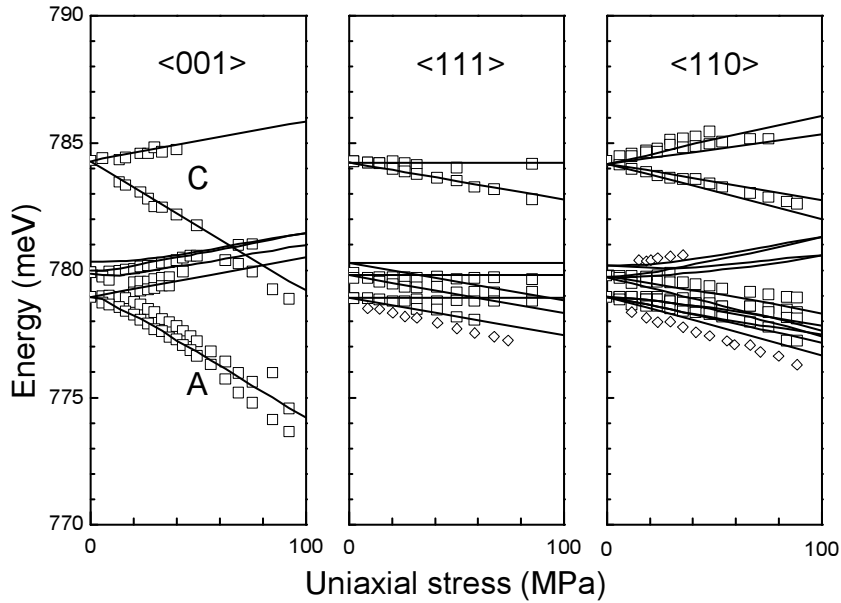


Figure 3.6: The squares show the data for the splittings of the no-phonon lines under stress along the  $\langle 001 \rangle$ ,  $\langle 111 \rangle$ , and  $\langle 110 \rangle$  crystal directions, measured in luminescence at 4.2 and 20 K. Experimental data for the transitions induced by the stresses are shown by diamonds. The lines are the fits derived from the model described in Sec. 3.5. Dashed lines originating near 780.2 meV show the predicted energies of the  $J = 0$  state.

excited states. Line  $C$  is not perturbed by the magnetic fields and so has an  $S = 0$  excited state. It also has a relatively high transition probability [Eq. 3.1]. The excited state of line  $C$  can be conveniently labeled  ${}^1T_2$  in a  $T_d$  notation. If the spins of the electron and hole can combine to give  $S = 0$ , then  $S = 1$  combinations are also expected. Line  $A$  splits isotropically into five components in a magnetic field (Fig. 3.4). Borrowing atomic physics notation, a  $T_2$  state has orbital angular momentum  $L = 1$ , which combines with  $S = 1$  to give  $J = 2, 1$ , and  $0$ ; the  $J = 2$  state would split into five components in a magnetic field, as does line  $A$ . Using a spin-orbit coupling  $H_{so} = \lambda \mathbf{L} \cdot \mathbf{S}$  and assigning the triplet state to line  $B$  predicts the  $J = 0$  state 0.3 meV above  $B$ . This state can be observed in luminescence when it is induced by  $\langle 110 \rangle$  uniaxial stresses, Fig. 3.6. The same splittings are observed for the 796-meV group of lines (Fig. 3.5), and here the line ascribed to  $J = 0$  can be observed at zero field at 797.2 meV. As required, it is not split by the magnetic field. The lines near 796 meV could therefore originate from the same electronic states as lines  $A$ ,  $B$ , and  $C$ , with a hole state 16.9 meV higher than that involved in those lines.

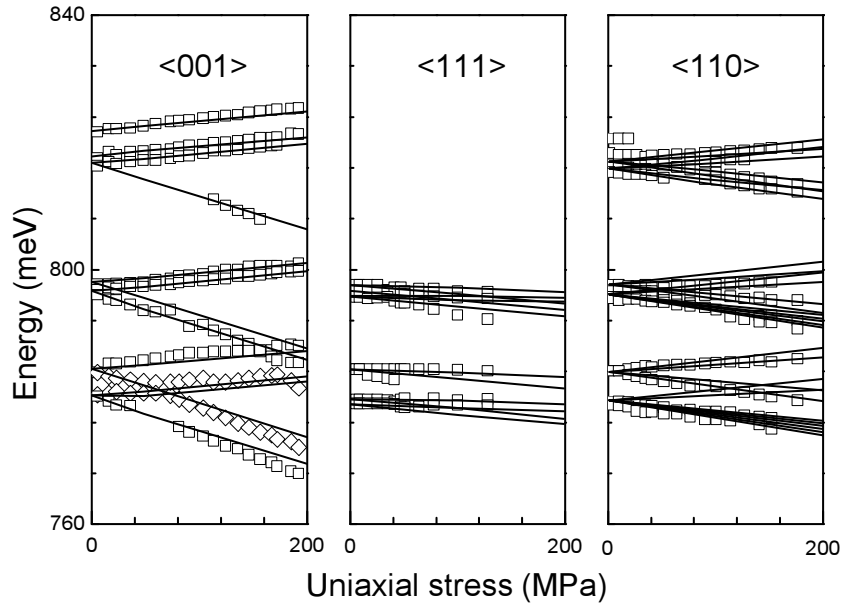


Figure 3.7: The squares show the data for the splittings of the no-phonon lines under stress along the  $\langle 001 \rangle$ ,  $\langle 111 \rangle$ , and  $\langle 110 \rangle$  crystal directions, measured in absorption at 4.2 K. The lines are the fits derived from the model described in Sec. 3.5.

For a more detailed description, it is convenient to write the  ${}^3T_2$  states in the angular momentum form

$$|1 \rangle = (T_2^x + iT_2^y)/\sqrt{2}, \quad |0 \rangle = T_2^z, \quad |-1 \rangle = (T_2^x - iT_2^y)/\sqrt{2}.$$

The perturbation caused by the magnetic field is

$$\Delta H_z = \mu_B(g_L \mathbf{L} + g_S \mathbf{S}) \cdot \mathbf{B}. \quad (3.9)$$

The combined stress and Zeeman perturbation matrix for the spin triplet states is given in the Appendices. The best fit to the Zeeman data for lines  $A$  and  $B$  gives  $\lambda = -0.46$  meV,  $g_S = 1.9 \pm 0.1$ , and  $g_L = 0$  (Fig. 3.4). Transitions induced from line  $F_0$ , shown by the diamonds in Fig. 3, are described well by simply downshifting the fits to the lowest-energy components of line  $A$ . The value  $g_L = 0$  is as required for valley-orbit states. The same scheme also fits the overall splitting of the lines near 797 meV, with the same parameters  $\lambda = -0.46$  meV and  $g_L = 0$ , but with a slightly reduced  $g_S = 1.3 \pm 0.1$ , Fig. 3.5.

To fit the stress data requires the inclusion of the hole state, moving in trigonal symmetry, with the  $C_{3v}$  point group. To define the notation we consider a particular orientation of the  $C_{3v}$  optical center with the  $C_3$  axis parallel to  $[111]$  and

with one of the reflection planes perpendicular to  $[1\bar{1}0]$ . The hole is perturbed as

$$\Delta V_h = a_1(s_{xx} + s_{yy} + s_{zz}) + a_2(s_{yz} + s_{zx} + s_{xy}), \quad (3.10)$$

where the  $a_i$  are electronic operators [37]. Only two parameters  $A_1$  and  $A_2$  are required to describe the effect of stresses on the hole state, corresponding to the effect of each of the operators  $a_1$  and  $a_2$  of Eq. 3.10. From an optical transition we only measure the *difference* in energy between states. Consequently, we can measure the difference in their perturbations by totally symmetric stresses, but not the absolute perturbations. We therefore absorb the perturbation by hydrostatic stresses of the electron state into that of the hole state. The best fit to the effect of uniaxial stresses on the transitions  $A$ ,  $B$ , and  $C$  is shown by the lines in Fig. 3.6. For the singlet states, the  $T_2$  level is perturbed as in Eq. 3.8. The perturbations of the optical transitions have been defined as the difference between the electron energies and the hole energies, and the compressive stress is positive. With these conventions, the best-fitting values are, with  $\pm 15\%$  uncertainty,  $A_1 = 6.5$  meV/GPa and  $A_2 = 3.7$  meV/GPa. The one parameter for the electron state is  $C = -11.2 \pm 1.5$  meV/GPa. This value is very similar to that of -11 meV/GPa found at the well-known 789-meV carbon-oxygen center [38] and is comparable to the free-electron parameter of -15.4 meV/GPa [35].

We have noted the close similarity in the no-field splitting and magnetic field perturbations of the multiplet near 796 meV and lines  $A$ ,  $B$ , and  $C$ . The stress data for these lines can also be fitted using the same stress parameters as for  $A$ ,  $B$ , and  $C$ , Fig. 3.7. Similarly, the higher-energy multiplet near 820 meV splits with the same shift rates as the corresponding components of line  $C$  (Fig. 3.7).

The model presented here describes a considerable amount of perturbation data using an electron state derived from the  $T_2$  valley-orbit states. The excited state of the line  $F_0$  does not form part of this scheme. We have not been able to determine the nature of that state since the  $F_0$  line is so weak. However, we note that the  $E$  valley-orbit states may be expected to be of a similar energy to the  $T_2$  states, and they *could* form the electron component of the exciton. The degeneracy  $g_F$  of the triplet  $E$  state would then be  $g_F = 6$ ; its exact value is not critical in its use below in Sec. 3.7.

### 3.6 Electron-phonon coupling

The phonon sidebands  $F_1$  and  $F_2$  are associated with a forbidden no-phonon line  $F_0$ , Sec. 3.3. This situation arises when a vibration of the optical center couples the electronic state from which transitions are forbidden to one from which optical transitions are allowed. The simplest case is when the Hamiltonian of the center

contains a term that is linear in the displacement of the relevant vibrational mode. The molecular deformation produced by a vibration is expected to perturb the orbital parts of the states rather than their spins and so will only couple states of the same spin. The line  $F_0$  is not readily detectable, but magnetic fields induce and shift the lower-energy components as for line  $A$  (Fig. 3.4), suggesting that the excited state of  $F_0$  is effectively another quintuplet. However, a definite assignment cannot be made to  $F_0$  since we do not see a full Zeeman splitting, and so we will allow  $F_0$  to interact with the excited states of either  $A$  or  $B$ . However, we can exclude coupling of  $F_0$  with the spin-singlet excited state of line  $C$ . The vibrational modes will be represented by one effective vibrational mode (with quantum energy of  $\hbar\omega$ ). In the absence of the vibronic coupling, the states can be represented by Born-Oppenheimer products of the *electronic states*  $\phi_X(r)$  ( $X = F, A, B$ ) and the harmonic vibrational states  $\chi_i(Q)$ :

$$\psi_{Xi} = \phi_X(r)\chi_i(Q), \quad (3.11)$$

where  $r$  represents the coordinates of the electrons,  $Q$  is the vibrational coordinate, and  $i = 1, 2, \dots, \infty$  indicates the vibrational state. These states are coupled by an electron-phonon term  $\hat{d}Q$  that is linear in the mode displacement  $Q$ , where  $\hat{d}$  is an electronic operator. We define the strengths of these interactions as

$$c_1 = \langle \phi_A | \hat{d} | \phi_F \rangle = \langle \phi_F | \hat{d} | \phi_A \rangle, \quad (3.12a)$$

$$c_2 = \langle \phi_B | \hat{d} | \phi_F \rangle = \langle \phi_F | \hat{d} | \phi_B \rangle. \quad (3.12b)$$

Since there are negligible phonon sidebands originating from no-phonon lines  $A$  and  $B$ , the effect of  $\hat{d}Q$  on the states  $\phi_A$  and  $\phi_B$  themselves is approximately zero:

$$\langle \phi_A | \hat{d} | \phi_A \rangle = \langle \phi_B | \hat{d} | \phi_B \rangle = 0. \quad (3.13)$$

Similarly, we have no evidence for any phonon sidebands occurring through simple relaxation of the state  $F$ , and so

$$d = \langle \phi_F | \hat{d} | \phi_F \rangle = 0. \quad (3.14)$$

The state  $\psi_{Fi}$  is mixed with  $\psi_{Aj}$  and  $\psi_{Bk}$  by the coupling, producing new eigenstates  $\Psi_{Fp}$ ,  $\Psi_{Aq}$ , and  $\Psi_{Br}$ , which lie in the space spanned by  $\psi_{Fi}$ ,  $\psi_{Aj}$ , and  $\psi_{Bk}$ :

$$\Psi_{Xp} = \sum_i f_{Xpi} \psi_{Fi} + \sum_j a_{Xpj} \psi_{Aj} + \sum_k b_{Xpk} \psi_{Bk}. \quad (3.15)$$

The coefficients  $f_{Xpi}$ ,  $a_{Xpj}$ , and  $b_{Xpk}$  may be found from the secular matrix, which has a very simple form. For each state  $X = F, A$ , and  $B$  with the same vibrational

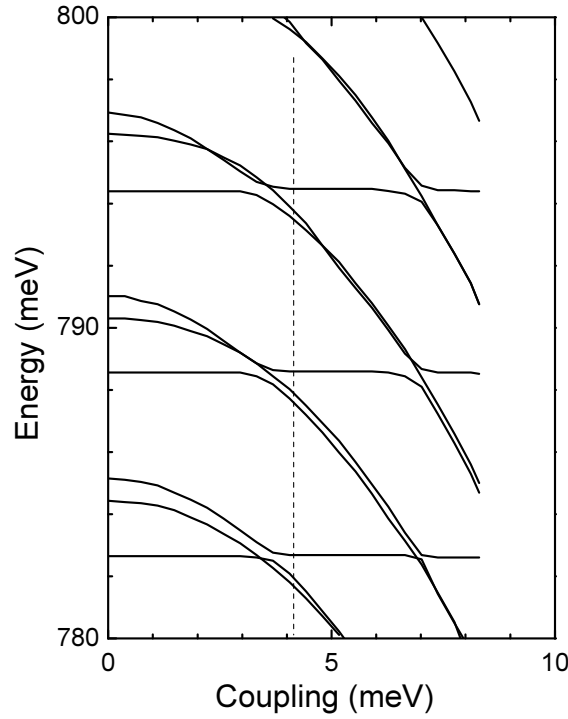


Figure 3.8: *The energies of the lowest vibronic levels of the electronic states  $F$ ,  $A$ , and  $B$  as a function of the coupling  $c_1\sqrt{\hbar/2m\omega}$ , calculated with  $c_2/c_1 = 0.06$ . The phonon energy has been taken as 5.8 meV. The vertical dashed line shows the value of the coupling that gives the best fit to the energy separations of  $F_0$ ,  $A$ , and  $B$ . The resulting predicted spectrum is shown by the simulated spectrum at the bottom of Fig. 3.1. The ground vibronic states are assumed to involve harmonic vibrations of the same 5.8-meV quantum.*

quantum state  $p$ ,

$$\langle \psi_{Xp} | H | \psi_{Xp} \rangle = E_X^0 + \left(\frac{1}{2} + p\right)\hbar\omega, \quad p = 0, 1, 2, \dots, \quad (3.16)$$

where  $H$  is the Hamiltonian, including the vibronic coupling, and  $E_X^0$  is the energy of the (uncoupled) electronic state  $X$ . All the other elements of the matrix are zero except where those pairs of states are coupled by  $\hat{d}Q$ . The effect of  $\hat{d}$  on the electronic part of the Born-Oppenheimer products is defined by Eqs. 3.12a, 3.12b and 3.13. Since the coupling term  $\hat{d}Q$  is linear in  $Q$ , it only couples vibrational states that differ by  $\pm 1$  in the quantum number. The coupling therefore has the form

$$\langle \psi_{Fi} | \hat{d}Q | \psi_{Aj} \rangle = \langle \phi_F | \hat{d} | \phi_A \rangle \langle \chi_i | Q | \chi_{i\pm 1} \rangle$$

$$= c_1 \sqrt{\frac{\hbar}{2m\omega}} \sqrt{i+1} \delta_{j,i+1} + c_1 \sqrt{\frac{\hbar}{2m\omega}} \sqrt{i} \delta_{j,i-1}, \quad (3.17)$$

with corresponding expressions for the coupling of  $\psi_{Fi}$  to  $\psi_{Bj}$ .

The eigenvalues and eigenvectors of the secular matrix can be found numerically. The variable parameters in the matrix are the differences between the three energies of the electronic states  $E_X^0$  without vibronic coupling, the coupling  $c_1/\sqrt{m\omega}$  between states  $F$  and  $A$ , and the coupling  $c_2/\sqrt{m\omega}$  between  $F$  and  $B$ . The measured data are the energies of the no-phonon states,  $E_F = 778.6$  meV,  $E_A = 778.9$  meV, and  $E_B = 779.85$  meV, the quantum  $\hbar\omega$  (which we set equal to the quantum of the mode of  $\hbar\omega = 5.8$  meV, since it is seen most strongly in the spectra), and the relative transition probabilities of line  $A$  to line  $F_1$  and  $A$  to  $B$ ; we may also set the transition probability for the no-phonon line  $F_0$  equal to zero. The energy levels of the lowest vibronic states are shown in Fig. 3.8 as a function of the coupling term  $c_1\sqrt{\hbar/2m\omega}$ .

It is found that a good fit can only be obtained when  $F_0$  couples predominantly with *either* state  $A$  *or* state  $B$ . The coupling is to the state  $A$  since the two-phonon line at 767.2 meV is observable as a result of the vibronic coupling, and its energy—and also the fact that it can be observed at temperatures when the no-phonon line  $B$  is very weak (Fig. 3.1)—implies that it is produced by the  $A$  state. A least-squares fit to the data then gives

$$c_1 \sqrt{\hbar/2m\omega} = 4.2 \text{ meV}, \quad c_2/c_1 = 0.06, \quad (3.18)$$

and the energies of  $F$ ,  $A$ , and  $B$  in the absence of vibronic coupling are obtained as  $E_F^0 = 781.5$  meV,  $E_A^0 = 782.2$  meV, and  $E_B^0 = 779.7$  meV.

The PL band shape, calculated for  $T = 4.2$  K, is shown in Fig. 3.1. It is very similar to the measured spectrum with the exception that the line  $F_2$  is omitted, since our model uses only one mode. The coupling produces a strong one-phonon transition  $F_1$  associated with the no-phonon line  $F_0$ , but one-phonon transitions from both  $A$  and  $B$  are forbidden. The weak coupling between the states  $F$  and  $B$  leads to undetectable two-phonon transitions from the  $B$  state. The calculation shows that the phonon line at 767.2 meV ( $A_1^2$ ) reported as a local mode with energy of 12 meV [26], in fact, is produced by a two-phonon transition involving the 5.8-meV mode and occurs as a consequence of the electron–phonon coupling between states  $A$  and  $F$ .

In this section we have seen that the luminescence band shape is unusual in that the phonon sidebands are not linked directly to the dominant no-phonon lines. This type of vibronic coupling appears to have been reported for only one other point defect in silicon [39]. We have shown that the spectral shape is produced by

a vibronic interaction between the lowest observed state  $F_0$  and the next observed state  $A$ . Confirmation of the model would be provided by an independent assessment of  $c_1$ . From Eq. 3.18, evaluation of  $c_1$  requires knowledge of the effective mass  $m$  of the vibration. This information is provided by isotope doping.

With natural Ag, the modes that produce the bands  $F_1$  and  $F_2$  have well-defined quanta of  $E_1 = 5.8$  meV and  $E_2 = 14.6$  meV (Sec. 3.3). If we assume that the non-phonon level  $F_0$  changes with isotopes in the same way as the closely adjacent line  $A$ , then the fractional changes in phonon energies are  $\Delta F_1 \sim 0.012$  and  $\Delta F_2 \sim 0.01$  from  $^{107}\text{Ag}$  to  $^{109}\text{Ag}$ . A very simple model of a heavy ion vibrating in a lattice shows that the frequency of vibration is approximately inversely proportional to the mass difference  $\Delta M$  of the heavy (Ag) ion and the host lattice (Si) (Ref. [40]); this model provides a qualitative understanding of the resonance modes of heavy ions in diamond [41]. Applied to  $^{107}\text{Ag}$  and  $^{109}\text{Ag}$  in  $^{28}\text{Si}$ , it gives a fractional shift of -0.012, consistent with the observed changes.

The appropriate mass to use in evaluating  $c_1$  is therefore that of the Ag atom. Then,

$$c_1 = 1.1 \times 10^{-10} \text{ J/m.} \quad (3.19)$$

Converting  $c_1$  to strain,

$$c'_1 = bc_1 = 0.2 \text{ eV/strain,} \quad (3.20)$$

where  $b$  is the interatomic spacing of the Si crystal (0.234 nm). Strain parameters in silicon are typically of the order of 1 eV/strain, confirming that  $c_1$  has a sensible order of magnitude. The line  $F_0$  is induced by stresses applied along the  $\langle 111 \rangle$  and  $\langle 110 \rangle$  directions, but not the  $\langle 001 \rangle$  direction, Fig. 3.6. This suggests that the shear stresses  $s_{yz} + s_{zx} + s_{xy}$  of Eq. 3.10 couple  $F_0$  to  $A$ . The coupling cannot, in practice, be determined from the data in Fig. 3.4. However, the value of the shear parameter  $A_2 = 3.7$  meV/GPa corresponds to a strain parameter of  $c_{44}A_2 = 0.3$  eV/strain, again of a similar magnitude to  $c'_1$ .

### 3.7 Thermal quenching of the luminescence

We have examined the decay characteristics of the  $A-B-C$  system. The measured decay times were found to be exponential over the entire temperature range and identical within the experimental error for all the components. This serves as an independent confirmation that the whole band corresponds to transitions at the same center. Figure 3.9 illustrates intensity decay of the lines  $A$ ,  $B$ , and  $C$  experimentally measured at 15 K. A lifetime of  $\sim 150 \mu\text{s}$  can be determined.

As one can see from Fig. 3.10, a strong variation of the decay times with temperature has been determined in the experiment. From a comparison with the

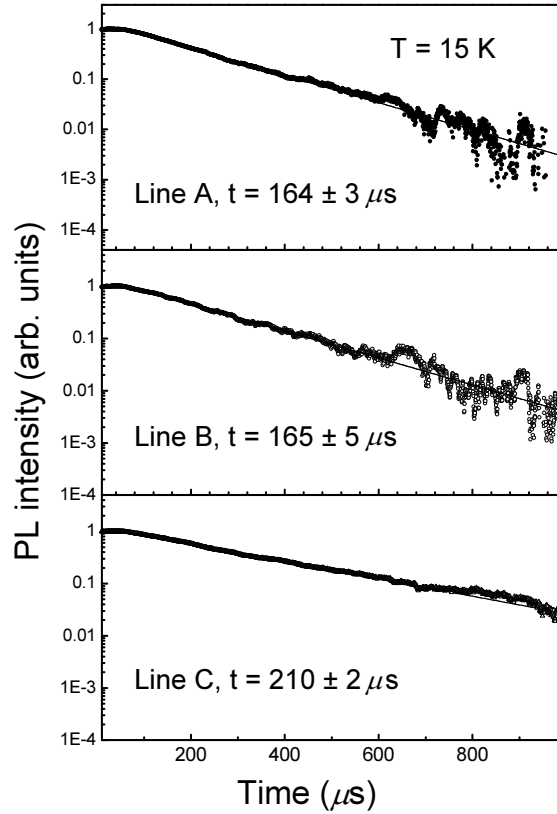


Figure 3.9: *Decay time characteristics for the lines A, B, C of the 780-meV PL band measured at 15 K.*

temperature dependence of the PL intensity, it seems natural to assume that the high-temperature decrease ( $T \geq 30$  K) of the lifetime is due to the dissociation of the exciton. From the experiment we can conclude that the decay times of the *A* and *B* lines are identical. Also the decay time of line *C*, whose intensity allowed accurate measurements for  $T \geq 10$  K, has a similar value. Such a situation is in agreement with the hypothesis that the *A*, *B* and *C* PL lines are due to transitions originating from three thermalizing states of the same center [25]. At low temperatures, we obtain long decay times of about  $250 \mu\text{s}$ . This value is large when compared with the lifetimes of donor or acceptor bound excitons in silicon, which are in the nanosecond range. For excitons bound to a donor or to an acceptor, the lifetime strongly depends on the impurity binding energy  $E_i$ . Experimentally, approximate dependencies  $\tau \propto E_i^{-4.6}$  for an acceptor or  $\tau \propto E_i^{-3.9}$  for a donor were reported and the lifetime shortening was attributed to a localized phononless Auger recombination process [42, 43]. For example, for excitons localized at In acceptors in silicon with  $E_i = 154$  meV, a lifetime of  $\tau = 2.7$  ns has

been determined [44]. The lifetimes measured in this study are longer by factor of  $10^5$ . This indicates that nonradiative lifetime shortening processes are absent, or heavily suppressed, in this case. For silicon such a situation would occur for an exciton trapped at an isoelectronic center [45, 46, 47, 48].

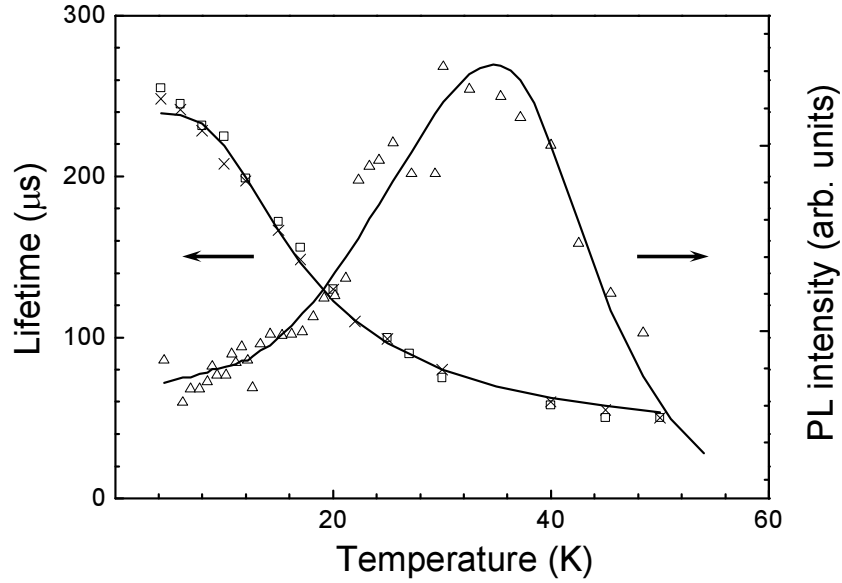


Figure 3.10: The intensity (arbitrary units) of the total luminescence from the band as a function of temperature is shown by the triangles. The temperature dependencies of the measured radiative decay times of lines A and B are shown by the squares and crosses, respectively. The lines are the least-squares fit of Eqs. 3.21 and 3.22.

Figure 3.10 shows, as functions of temperature, the luminescence intensity integrated across all the band (triangles) and the radiative decay times of lines A (squares) and B (crosses), measured in independent samples. As the temperature increases to  $\sim 35$  K, the total intensity increases with the increasing population of state C, from which transitions are strongly allowed (Sec. 3.3). The decrease at high temperature occurs generally for luminescence centers in silicon, Sec. 3.1. We know from Sec. 3.3 that all the excited states of the center reach thermal equilibrium before the PL transition occurs and so the intensity is expected to follow

$$I(T) \approx \frac{I(0) \left[ 1 + \sum_i (\tau_F g_i / \tau_i g_F) \exp(-E_i/kT) \right]}{1 + \sum_i (g_i/g_F) \exp(-E_i/kT) + (g/g_F) T^{3/2} \exp(-E_a/kT)}. \quad (3.21)$$

Here the sums are over all the states  $i = A, B,$  and  $C$  and  $1/\tau_i$  is the mean transition probability for the radiative transitions originating each of the  $g_i$  degenerate states of the state at an energy  $E_i$  above  $F_0$ . The thermal quenching of the excited states has an activation energy  $E_a$  and an effective degeneracy of  $(g/g_F)T^{3/2}$  relative to state  $F_0$ .

The decay times as measured for lines  $A$  and  $B$  from 4 to 50 K are also shown in Fig. 3.10. Lines  $A, B,$  and  $C$  decay exponentially with time after a pulse of excitation. Since their excited states are in thermal equilibrium, Sec. 3.3, their decay times are equal at each temperature. Corresponding to Eq. 3.21, the decay time  $\tau$  is given by

$$\frac{1}{\tau(T)} = \left( \frac{g_F}{\tau_F} \right) \left[ \frac{1 + \sum_i (\tau_F g_i / \tau_i g_F) \exp(-E_i/kT) + (r g / g_F) T^{3/2} \exp(-E_a/kT)}{1 + \sum_i (g_i / g_F) \exp(-E_i/kT) + (g / g_F) T^{3/2} \exp(-E_a/kT)} \right]. \quad (3.22)$$

Here the term  $r$  determines the rate of ionization into the continuum.

In Eqs. 3.21 and 3.22, the values of  $E_i$  are known from the optical spectra, and  $g_F = 6, g_A = 5, g_B = 3,$  and  $g_C = 1,$  from Secs. 3.5 and 3.6. From the measured ratio of the probabilities of transitions  $F, A,$  and  $B,$  Eq. 3.1, we know the ratios  $\tau_F/\tau_A$  and  $\tau_B/\tau_A$ :  $\tau_F/\tau_A = (I_A g_F / I_F g_A) = 1.8$  and  $\tau_B/\tau_A = (I_A g_B / I_B g_A) = 0.9$ . The thermal-quenching energy  $E_a$  is best found from the luminescence data. It is not sensitive to the other parameters, and a least-squares fit gives  $E_a = 33.3 \pm 1$  meV. This value is in agreement with the threshold of photo-ionization from the excited states ( $E_a = 33$  meV, Ref. [49]). It is also comparable to the value of 41.7 meV for the binding energy relative to state  $C,$  derived indirectly by assuming that the transition at 816 meV involves an effective mass electron in a  $2p_0$  state, which can be compared to the energy levels of a donor [28]. The value of  $E_a$  has been fixed at 33.3 meV. A least-squares fit of Eqs. 3.21 and 3.22 to all the data in Fig. 3.10 can now be made with five adjustable parameters. They are determined as  $\tau_A = 1020 \mu\text{s}, \tau_C = 6.3 \mu\text{s}, g = 490 \text{ K}^{-3/2},$  and  $r = 435,$  plus the physically insignificant  $I(0) = 60$ . Variations in the fitting strategy can change  $\tau_A$  and  $r$  by 50%, while  $\tau_C$  and  $g$  appear to be stable to  $\pm 10\%$ . Radiative decay times in the microsecond range are typical for centers in silicon with diffuse excited states. From the parameters, we have  $I_F/I_C = (g_F \tau_C)/(g_C \tau_F) = 0.02 \pm 0.01,$  confirming the value in Eq. 3.1.

We can now clarify why in our fitting procedure we first obtained the quenching energy  $E$  from the luminescence intensity. If there was no quenching, the luminescence would increase and saturate as state  $C$  became populated. The quenching therefore has a major effect on the total luminescence. In contrast, it has a smaller absolute effect on the lifetime, which is already severely reduced by the relatively

short lifetime of the excited state of line *C*. By combining the data, we can estimate the rate of thermal ionization, which does not appear to have been presented for any pseudodonor in silicon. In Eq. 3.22 the term  $(r_g/\tau_F)T^{3/2}\exp(-E_a/kT)$  represents the thermally activated quenching of the luminescence, which consists of a Boltzmann term and the usual preexponential, which is temperature dependent. At 50 K, the prefactor has the value  $4 \times 10^{10}$  Hz, surprisingly slower than the frequency ( $\sim 10^{12}$  Hz) of the dominant 5.8-meV phonon.

### 3.8 Summary

We have reported the results of a detailed phenomenological study of the optical properties of a silver-related center in silicon. Perturbations of the optical transitions by uniaxial stresses and magnetic fields have been accurately described in terms of an effective-mass electron, orbiting the center in a triply degenerate orbital state in effectively  $T_d$  symmetry, and a tightly bound hole, which has its angular momentum quenched by the local trigonal field of the center (Sec. 3.5). These particles couple through their spin. At a slightly lower energy than these readily observed states, a state exists from which optical transitions are strongly forbidden, but which is phonon-coupled to the other electronic states. As a result, the vibronic sidebands observed at low temperature derive from the forbidden no-phonon line (Sec. 3.6). Using an effective mass for the vibrational mode derived from isotope data (Sec. 3.4), we have shown that the required magnitude of the electron-phonon coupling is of a reasonable magnitude. With this energy-level scheme, the total luminescence and the radiative decay time have been fitted over the temperature range 4 - 50 K, and it has been shown that the data can give an estimate of the time taken to thermally ionize an electron from an effective-mass state (Sec. 3.7). A highly detailed phenomenological understanding of the optical properties can therefore be achieved, even though the molecular structure of the core of the center has not been determined.

# Chapter 4

## Two-Color FEL Spectroscopy of Isoelectronic Center in Silicon

*Time-resolved “two-color” photoluminescence is reported from the 944 meV band produced by a low concentration of copper in silicon. Photoluminescence has been generated by a pulsed pump beam, and then partially quenched by a probe beam from a free-electron laser. The kinetics of the quenching allow the absorption cross section for photo-ionization of the center to be determined without knowing its concentration in the sample. The time-resolved data demonstrate a partial recovery of the luminescence after photo-ionization, due to repopulation of the ionized traps.*

### 4.1 Introduction

As in other indirect-gap semiconductors, luminescence from pure silicon is weak. If the excitation energy is localized on an impurity, the luminescence yield may be increased by overcoming the wavevector selection rule. At low temperature, the radiative lifetime of the luminescence from most optical centers in silicon is usually long, of the order of 100  $\mu\text{s}$ . Consequently, most of the strongly luminescent centers are in the neutral charge state, isoelectronic with the lattice, because a charged center could preferentially de-excite by an Auger emission of the excess charge. A very simple picture has been developed for the excited states of the majority of the isoelectronic centers. Excitation of the center is equivalent to exciting one charge (hole or electron) to a higher energy state at the center, leaving the core of the center charged (negative or positive, respectively). The high permittivity of silicon and the low effective masses of the electrons and holes result in the excited charge moving into an effective-mass state. The effective-mass particle may be the hole, for example at the carbon-related “T” center [12], or the electron, as in the example discussed in this Chapter. By using the known properties of the extremes of the

valence or conduction bands, it is possible to understand in detail many properties, such as the response of the states to perturbations [50], or to link the relative optical transition probabilities of different excited states to the electron-phonon coupling at the center [14]. The partial separation of the electron and hole states results in the long radiative lifetimes and, consequently, in very weak absorption strengths, but the localization of the energy produces apparently high quantum efficiencies. Photoluminescence (PL) spectroscopy associated techniques have therefore been the preferred optical probes of the centers. For example, for some centers, the Rydberg-like series of excited states have been detected by photoluminescence excitation spectroscopy [38]. The long lifetimes in the excited states also favor two-color spectroscopy, in which one “pump” beam (of photon energy of the order of the band gap) excites the center, and a second mid-infrared “probe” beam (with photons of the order of 10 to 100 meV) excites transitions within the effective-mass states [51, 52]. Precision measurements of the effective-mass states have been reported, using high spectral resolution in the probe beam. Additionally, we note that in a “two-color” experiment the selection rules for transitions induced by the probe allow states to be investigated that are not observed by direct PL measurements.

To date, the two-color experiments have used steady-state excitation (strictly, low-frequency modulated for lock-in detection). This approach allows high spectral resolution. However, the concentrations of the optical centers are usually not known with any precision, and the fraction of them in the excited states is also unknown, so that data cannot be obtained on the kinetics of the processes. In this Chapter we report time-resolved two-color excitation, in which a pulsed probe beam has been obtained from a free-electron laser (FEL). These measurements allow the photo-excitation cross section of transitions from the excited states to be determined without knowing the concentration of the excited optical centers. The data also show evidence for the recapture of a carrier photo-ionized from the optical center.

We consider here a luminescence center produced by copper in silicon. Copper doping of silicon is of relevance for technology. Here a considerable boost has been provided by applications of copper interconnects in recent generations of microchips [53]. The behavior of copper in silicon has been extensively studied and a lot of information has been gathered [54]. In an isolated form, Cu has been found to take a somewhat distorted substitutional position [55]. Due to its high solubility and rapid diffusion (as a positively charged species) copper is one of major contaminations of silicon. At low temperatures it precipitates and clusters with other defects. Many of these centers exhibit electrical activity; some are involved in radiative recombinations. The most familiar PL system it produces

has a zero-phonon line (ZPL) at 1014.7 meV. This band is highly characterized. It occurs from a center of trigonal symmetry [9], and the excited states can be described in terms of an effective-mass electron orbiting in the local trigonal field [56]. The binding energy of the electron is estimated to be 32 meV from the thermal quenching of luminescence from the center [9]. In the positive charge state, the tightly bound hole state is observed in deep level transient spectroscopy (DLTS) at  $E_v + 0.1$  eV [57]. The vibronic sideband is characterized by a low energy resonance phonon of 7 meV, identified as a highly-localized, in-phase motion of the nearest-neighbor substitutional-interstitial copper pair forming the center [58]. We consider here a lesser investigated center, known as  $\text{Cu}^*$  that is produced by a lower contamination with Cu. The PL band has a very similar shape to that of the 1014 meV band, and only differs by having its ZPL shifted by 70 meV to lower energy to 944 meV [59]. Correspondingly, we expect that the deep hole state will be shifted deeper into the gap by the same amount, because, for this type of center, the sum of the hole level, the energy of the ZPL, the binding energy of the electron (again assuming  $\sim 30$  meV for an effective-mass electron in silicon), and the exciton binding energy (15 meV) will be close to the indirect energy gap (1170 meV at low temperatures). The associated hole level is located at  $E_v + 0.185$  eV [60]. Recent *ab initio* calculations suggest that the  $\text{Cu}^*$  center consists of a substitutional Cu atom with an interstitial Cu atom located near the third neighbor tetrahedral site [61]. This assignment disagrees with published uniaxial stress perturbations of the line, but those data were measured only for low stresses and they are not fully understood [62]. For present purposes it is sufficient to know (from the DLTS data) that the center has a deep-hole, shallow-electron structure, and that the center is produced with low metallic contamination.

## 4.2 Experimental details

The samples for the current study were prepared by evaporating copper on both sides of a sample. The metal was in-diffused by heating for 4 h at 1150 °C in a closed quartz ampoule containing 100 mbar of argon. After the diffusion step, the ampoule was quenched to room temperature in water and the samples were etched to remove 70  $\mu\text{m}$  of the surface layers. The PL spectra of the resulting samples showed exclusively the  $\text{Cu}^*$  band.

For the two-color measurements reported here, the pump beam was the second harmonic of a Nd:YAG laser (532 nm) with a repetition rate of 5 Hz and a pulse duration of 100 ps. A mid-infrared (MIR) probe pulse with duration of  $\sim 5$   $\mu\text{s}$  was provided by the FEL. The wavelength of the FEL is tunable and can be activated with a selected time delay  $\Delta t_F$  with respect to the Nd:YAG laser pulse.

Measurements were carried with the sample fixed on the cold finger of a flow cryostat resulting in a sample temperature of 16 K.

### 4.3 Results and discussion

Figure 4.1 shows the decay of the 944 meV after excitation by the pump pulse. The figure also shows the effect on the decay curves of FEL pulses applied with delay times of 100  $\mu\text{s}$  and 400  $\mu\text{s}$ . For these data, the FEL pulse had a photon energy set to  $E_{\text{ph}} = 60$  meV, and a relatively low power (with 10 dB attenuation). Using only the pump pulse, the PL intensity decays exponentially with a decay rate of  $W_1 = 4.4 \times 10^3 \text{ s}^{-1}$ . Applying a FEL probe pulse produces a strong quenching of the PL, Fig. 4.1. The quenching effect is not observed when the FEL photons are applied prior to the pump excitation pulse, ruling out sample heating by the FEL pulse as the cause of the quenching. Fig. 4.1 also shows that after a rapid decrease during the FEL pulse, the decay curve continues with the same exponential decay time as without the FEL pulse: PL quenching takes place only during the FEL pulse. For a fixed photon energy  $E_{\text{ph}}$  and a photon flux  $\phi$  of the FEL, the fraction of the PL signal that is quenched is independent of the delay time, that is, the quenching is proportional to the concentration of the emitting centers available at the moment when the FEL is fired. All data have been taken in the regime where the PL quenching effect depends linearly on the pump power (no saturation effects are considered). In the absence of the FEL pulse the decay of the population  $N$  in the luminescing state therefore follows the usual rate equation  $dN/dt = -W_1N$ . During the FEL pulse, this becomes modified to  $dN/dt = -W_1N - W_qN$ , where  $W_q$  is the decay rate induced by the FEL pulse. This induced decay rate is found to be proportional to the FEL photon flux  $\phi$ ,  $W_q = \sigma\phi$ , at a fixed photon energy  $E_{\text{ph}}$ . The physical meaning of  $\sigma$  is therefore that the cross section for the absorption of photons from the excited state at each of the centers. We define  $R$  as the “time-integrated” ratio of the PL intensity observed with and without the FEL pulse, where the integral is from the time chosen for the pulse to infinity. We approximate the FEL pulse by a square pulse of duration  $\tau$ . Then, we expect that the quenching ratio, measured from the time of switching off the FEL pulse ( $t = 0$ ), is given simply by

$$R = \frac{\exp[-W_q\tau] \int_0^\infty \exp[-W_1t] dt}{\int_0^\infty \exp[-W_1t] dt} = \exp[-W_q\tau]. \quad (4.1)$$

However, there is a further complication in that when the power of the FEL pulse is increased so that there is almost complete quenching of the Cu signal, a recovery is observed, commencing after the quenching (Fig. 4.1, inset). Integrating

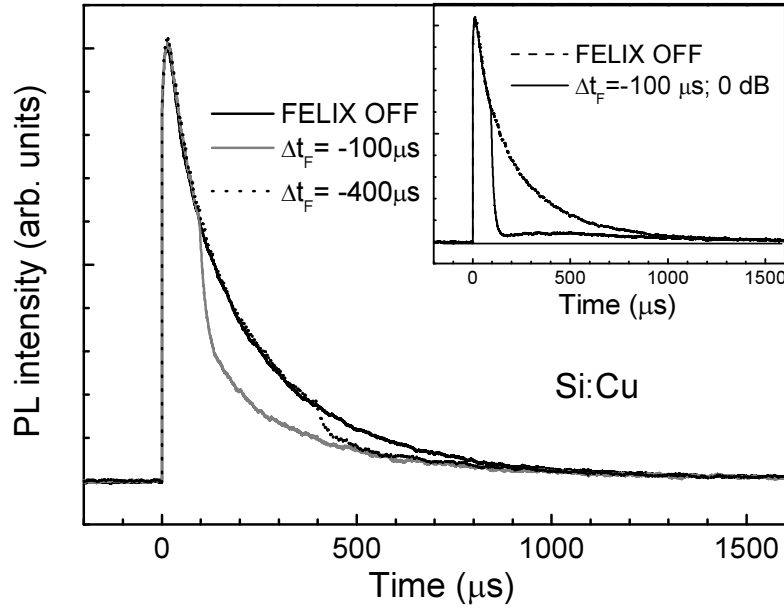


Figure 4.1: The quenching of Cu-related PL band (944 meV) by the FEL probe pulse. The effect is illustrated for a photon energy of 60 meV with the probe pulse applied 100 and 400  $\mu\text{s}$  after the YAG-laser excitation (denoted by  $\Delta t_F = -100, -400 \mu\text{s}$ ). The inset shows the recovery of the PL signal after termination of the probe pulse (set to a maximum intensity of the MIR probe photons).

the PL to long time shows that  $29 \pm 3 \%$  of the quenched Cu signal recovers after the FEL pulse. This fraction is found to be independent of the photon energy and also of flux of the FEL beam. It is proportional to the signal level after the FEL pulse, and so in the simple description employed here it increases the numerator of Eq. 4.1 by a constant factor.

The origin of the quenching is established by Fig. 4.2, where the FEL quenching rate is plotted as a function of the FEL photon energy  $E_{\text{ph}}$  for three different FEL fluxes, all sufficiently low that the quenching rate is linearly dependent on the flux. The quenching rate  $W_q$  is known directly as  $-\ln(R)/\tau$ , Eq. 4.1, and has been normalized to constant FEL flux density. (We assume that the signal recovered after the FEL pulse is constant and equal to 29 % of the quenched signal).

The threshold, near the energy expected for ionization of the effective-mass electron, establishes that the quenching process is simply the photo-ionization of the electron. The photo-ionization cross section  $\sigma$  into a continuum of states is expected to depend on the photon energy  $E_{\text{ph}}$  as

$$\sigma(E_{\text{ph}}) \propto \frac{(E_{\text{ph}} - E_{\text{D}})^{3/2}}{(E_{\text{ph}})^{3+2\gamma}}, \quad (4.2)$$

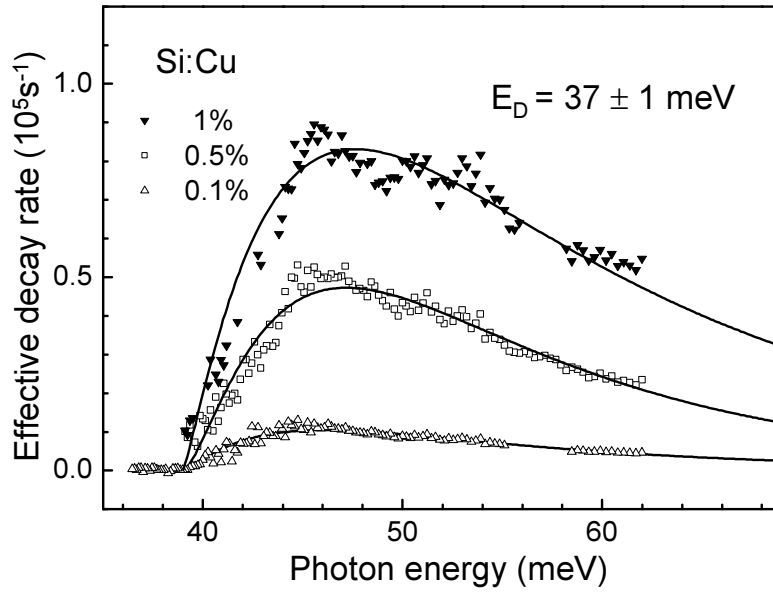


Figure 4.2: *The effective decay rate  $W_q$  induced by the FEL pulse of Si:Cu sample as a function of FEL photon energy, for three different values flux of the MIR photon.*

where  $E_D$  is the threshold energy for the ionization, and  $\gamma$  is an adjustable parameter of the order of unity. The lines on Fig. 4.2 are a fit of Eq. 4.2 with  $\gamma = 1.6$  and define the threshold as  $E_D = 37 \pm 1$  meV. For a silver-doped silicon material, which forms a similar bound exciton optical center giving rise to PL band at 780 meV, a fit to photo-ionization data produces  $E_D = 39 \pm 1$  meV – see, Fig. 4.3.

Figure 4.4 plots the quenching ratio  $W_q$  against the FEL flux  $\phi$  for three values of the FEL photon energy  $E_{ph}$ . Since  $W_1$  and  $\tau$  are known, a least-squares fit to  $W_q$  ( $= \sigma\phi$ ) gives  $\sigma$  for each value of  $E_{ph}$ . The values of  $\sigma$  decrease from  $\sigma = 1.1 \times 10^{-16}$  cm<sup>2</sup> at  $E_{ph} = 45$  meV to  $8.7 \times 10^{-15}$  cm<sup>2</sup> and  $5.6 \times 10^{-15}$  cm<sup>2</sup> at 54 and 62 meV respectively, where allowance has been made for reflection losses at the surface of the sample. (The magnitudes may be underestimated by about 30% by neglect of partial reflection of the beam from the surface of the sample.)

The ratios of the values for  $\sigma$  are in close agreement with the ratios of the cross sections at those photon energies shown in Fig. 4.3. To check the order of magnitude of the cross sections, we note that the absorption coefficient  $\mu$  is related to the cross section  $\sigma$  by  $\mu = \sigma N$  where  $N$  is the concentration of the optical center. The excited state of the Cu center consists of an effective – mass electron orbiting a positive hole – a configuration very similar to an electron orbiting a phosphorus donor. The ionization continuum of the P donor has a cross

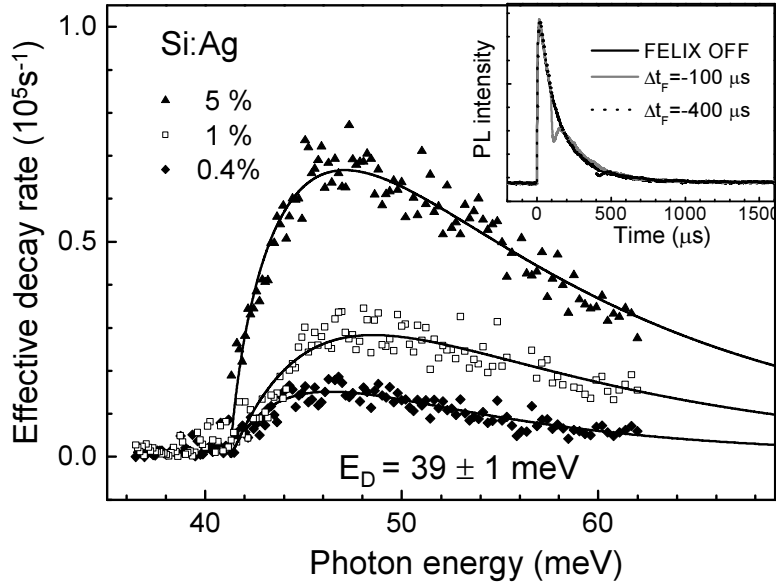


Figure 4.3: The effective decay rate  $W_q$  induced by the FEL pulse as a function of FEL photon energy, for three different values flux of the MIR photon for Si:Ag sample. The inset shows the quenching of Ag-related 780-meV PL band by the FEL probe pulse with a photon energy of 60 meV and the probe pulse applied 100 and 400  $\mu\text{s}$  after the YAG:Nd laser excitation.

section of  $\sigma = \mu/N \sim 2 \times 10^{-15} \text{ cm}^2$  [63], of the same order as the values obtained here for  $\text{Cu}^*$ .

We have noted that the fraction of the signal that recovers after the FEL pulse is independent of the properties of the FEL pulse, but is proportional to the signal after the pulse – that is, it is proportional to the effect of the pump beam. It could therefore be an intrinsic property of the center, or it could be an effect of the pump beam ionizing other centers. A similar effect has been observed for Si:Ag, – Fig. 4.3, inset [64]. A time-dependent measurement allows the recovered fraction to be observed, in contrast to a steady-state measurement, such as when measuring the loss of PL as the temperature is increased, where the recovered fraction is simply observed as an indistinguishable part of the total signal.

One of the unanswered questions concerning the class of isoelectronic centers is the ionization mechanism. Thermal quenching of the PL may have an activation energy equal to the ionization of the shallow particle, for example at the 780 meV Ag center [65], or it may be equal to the binding energy of the tightly-bound particle, as at the sulfur-related centers [66], or it may equal the exciton binding energy. We have seen that following photo-ionization of the  $\text{Cu}^*$  center, there is

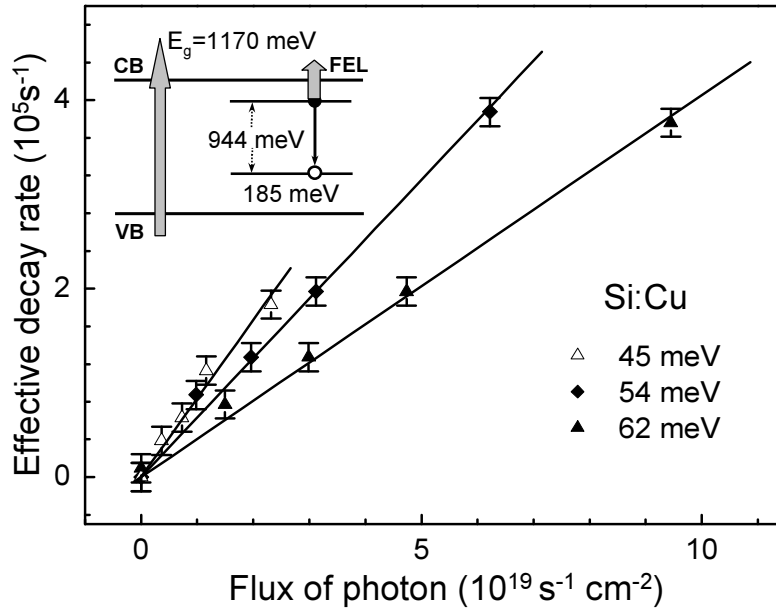


Figure 4.4: The flux dependence of the MIR-induced quenching PL for photon energies of 45, 54, and 62 meV and a delay time of  $\Delta t_F = -200 \mu\text{s}$ . The inset shows the model for the quenching effect.

a transient increase in the PL signal (Fig. 4.1, inset). In contrast to ionizing a gas atom, where by definition the electron travels away from the ion, an electron ionized from a center in a crystal can lose energy as it comes to thermal equilibrium with the lattice. For example, an electron of mass  $0.1 m_e$  and kinetic energy 20 meV would travel a total distance of about 100 to 1000 atomic spacings in  $10^{-13}$  to  $10^{-12}$  s, which we take as the time to come to thermal equilibrium. The Coulomb potential attracting the electron to the ionized center is then at least 5 to 0.5 meV in magnitude, comparable with the thermal energy of about 1.4 meV (16 K). With no externally applied electric field, recapture of the ionized electron is quite probable. With increasing temperature, the probability that the electron will escape increases, and indeed the experimental results show that the magnitude of the PL recovery process is strongly temperature-dependent and does not occur for  $T > \sim 40$  K. With a weak Coulomb potential, as at the 780 meV center, recapture is likely to affect predominantly the emission rate, and so is not obvious in a steady-state measurement. With a deep potential, as at the sulfur-related centers with electron binding energies of about 60 meV, thermal ionization of the shallow particle alone may be prohibited.

The situation is different for high concentration of centers. For this case we note that the cross section for electron capture in cascade process, as applicable

for a shallow, effective-mass state, has a relatively high value, of an order of  $\sigma \approx 10^{-11} \text{ cm}^2$ . Assuming a reasonable value of average thermal velocity of electrons in Si at cryogenic temperature,  $\langle v_{th} \rangle \approx 10^6 \text{ cm s}^{-1}$  we get the characteristic time constant of the recapture process of  $\tau_{cap} = [N\sigma_{cap} \langle v_{th} \rangle]^{-1} \approx 0.1 \text{ ns}$  for concentration of the Cu centers of  $10^{15} \text{ cm}^{-3}$  [67]. We further note that at this concentration the average distance between the centers would be of an order of  $d = 100 \text{ nm}$ , comparable to the effective capture radius  $r_{eff} = e^2/\kappa kT \approx 50 \text{ nm}$ , for the Si dielectric constant  $\kappa = 12$  and  $kT = 3 \text{ meV}$ . Therefore optical ionization would be in that case a transient phenomenon, taking place only during the FEL pulse, with the full recovery of the PL signal upon termination of the pulse. At higher temperatures, the capture cross section decreases leading, accordingly, to a decrease of the effective capture radius and the increased capture time. However, we point out that while in the present study the concentration of the investigated copper center is not exactly known, the PL band in question is reported to appear upon low copper doping levels. If we assume the concentration to be  $10^{13} \text{ cm}^{-3}$ , then the inter impurity distance will increase to  $d \approx 4 \mu\text{m}$  and recapture probability of the opto-ionized electron at the copper center will diminish.

## 4.4 Conclusions

Using a Cu center in silicon, we have demonstrated that the ionization cross section can be measured for unknown concentrations of centers from the kinetics of the two-color excitation measurements. We have verified the value by comparison with the absorption coefficient reported using known concentrations of shallow donors. Further, we have presented evidence of the recapture of charge photo-ionized from the center.



# Chapter 5

## The First Observation of Zeeman Effect in Photoluminescence of Si:Er

*A successful observation and a preliminary analysis of the Zeeman effect on the  $\lambda \approx 1.54 \mu\text{m}$  photoluminescence band in Er-doped crystalline MBE-grown silicon are presented. The symmetry of the dominant optically active centers is conclusively established as orthorhombic-I ( $C_{2v}$ ) with  $g_{\parallel} \approx 18.39$  and  $g_{\perp} \approx 0$ . In this way the long standing puzzle as regards the paramagnetism of optically active Er-related centers in silicon is settled. Preferential generation of a single type of an optically active Er-related center confirmed in this study is essential for photonic applications of Si:Er.*

### 5.1 Introduction

Rare earth doping of semiconductors is known to result in formation of luminescent centers suitable for applications in optoelectronic devices [68,69,70]. Among the various rare earth elements, Er has attracted particular attention because the  ${}^4I_{13/2} \rightarrow {}^4I_{15/2}$  transition involving nonbonding  $4f$  shell electrons of the  $\text{Er}^{3+}$  ion ( $4f^{11}$ ) occurs at the technologically important wavelength of  $1.54 \mu\text{m}$ , matching the absorption minimum of silica-based optical fibers. The Si:Er system is of special interest in view of the success and versatility of silicon technology. Also, Si:Er light emitting structures are attractive in association with potential applications for optical interconnects in future photonic chip technology. As a result of a continuing research effort Si:Er-based light emitting diodes have now been successfully developed - for an up-to-date review, see, e.g., [71]. A further increase of emission

efficiency and thermal stability by materials engineering is, however, obstructed by the apparent lack of understanding of more fundamental aspects related to the optical activity of  $\text{Er}^{3+}$  ions in Si. In contrast to previously mentioned impressive developments toward practical devices, the Si:Er system remains poorly understood and even controversial as regards the microstructure of the optically active Er-related centers and the relevant energy transfer mechanisms [72]. This situation is all the more unfortunate, when bearing in mind the prominent position of Si:Er with respect to applications.

The microscopic structure of Er dopants in Si has been investigated using extended X-ray-absorption fine structure (EXAFS), and the presence of oxygen in the immediate surrounding of the optically active Er atom was concluded [73]. The formation of an Er-related cubic center has been found in channeling experiments [74], which identified an isolated Er atom at a tetrahedral interstitial site as the dominant center generated in crystalline silicon by Er implantation. The findings are in accordance with theoretical calculations for isolated Er in Si [75]. Unfortunately, these techniques can not directly distinguish between optically active and non-active Er-related centers. Having in mind that only a small percentage (1 to 10%) of Er dopants in silicon exhibit optical activity [70], [76], there exists a large probability that above-mentioned studies concern the nonactive species and therefore are not relevant for the issues related to light emission from Si:Er. Also electron paramagnetic resonance (EPR), the experimental technique for the identification of the microstructure of defects, failed to detect the optically active Er-related centers in crystalline silicon [77]. Microscopic information on centers responsible for Er-related  $1.5 \mu\text{m}$  emission in Si was revealed by high-resolution photoluminescence (PL) study which identified more than 100 emission lines related to several Er-induced centers [76].

Microscopic aspects of the Er-related emitting center would best be provided by the magneto-optical study of the main features of the emission spectrum. However, due to the inhomogeneous character of PL bands, application of magnetic field results in broadening and thus subsequent vanishing of the emission lines. Consequently, in spite of repeated claims [78], no successful observation of Zeeman effect in PL has been reported for Si:Er until now. The situation is dramatically different for Si:Er material grown recently by the sublimation molecular beam epitaxy (SMBE) technique. In this case, the PL spectrum (depicted in Fig. 5.1) contains only a few lines of a very small width  $\Delta E < 10 \mu\text{eV}$ . Based on crystal field analysis, there were assigned to a single type of center, labeled Er-1, of noncubic symmetry [79, 80]. Taking advantage of the small linewidth of the Er-1 spectrum a successful observation of Zeeman effect in PL was possible. In this Chapter we present results of the magneto-optical investigation of the main PL band ( $\lambda \simeq 1.54$

$\mu\text{m}$ ) of the Er-1 spectrum, indicated with an arrow in Fig. 5.1. We note that also the (broad) PL spectra observed in Er-implanted samples usually have maxima located at this wavelength [71, 76]. Consequently, our findings are important for understanding of the optical activity of Si:Er in general.

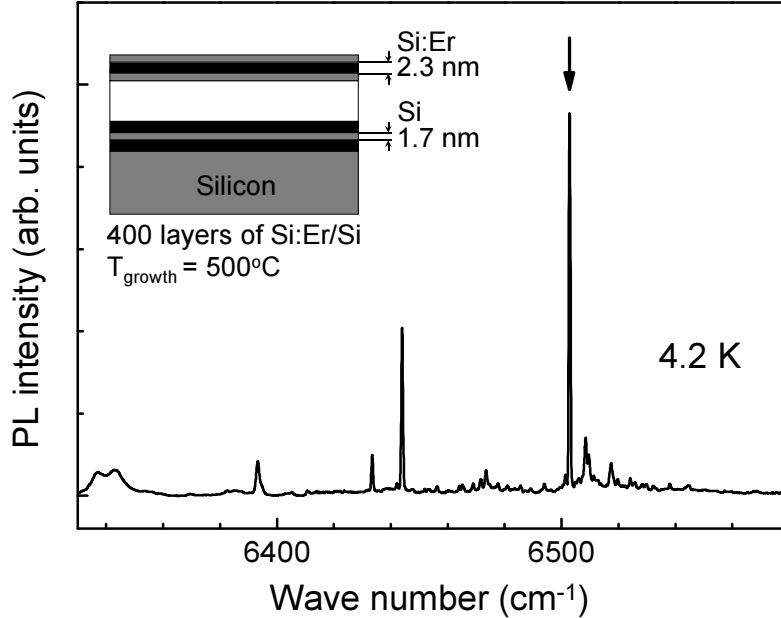


Figure 5.1: *Photoluminescence spectra of the multilayer Si/Si:Er structure used in the current study (see inset), as measured at  $T = 4.2$  K. The arrow marks the most intense emission line for which the Zeeman effect was subsequently investigated.*

## 5.2 Experimental details

The inset to Fig. 5.1 shows a cartoon of the structure used in the current study. It comprises 400 interchanged Si and Si:Er layers of a few nanometers thickness stacked along the  $\langle 100 \rangle$  growth direction. Magneto-optical experiments were performed at 4.2 K using a cw  $\text{Ar}^+$ -ion laser operating at 514.5 nm for excitation. The sample was placed in a split-coil superconducting magnet with optical access. The emerging luminescence was dispersed by a high-resolution 1.5 m  $f/12$  monochromator (Jobin Yvon THR-1500 equipped with a 600 grooves/mm grating blazed at 1.5  $\mu\text{m}$ ), and detected with a liquid-nitrogen cooled Ge detector (Edinburgh Instruments). For polarization measurements a quarter-lambda plate and a linear polarization filter were used.

### 5.3 Results and discussion

In the tetrahedral environment the  ${}^4I_{13/2}$  first excited state of the  $4f^{11}$  shell of the  $\text{Er}^{3+}$  ion splits into a series of  $2\Gamma_6 + \Gamma_7 + 2\Gamma_8$  sublevels and the ground  ${}^4I_{15/2}$  state splits into the sequence  $\Gamma_6 + \Gamma_7 + 3\Gamma_8$  [81]. Consequently, at low temperatures five PL lines are expected. A lower symmetry crystal field splits the remaining quartets into doublets. In this case eight spectral components will appear, with each PL line corresponding to a transition between effective spin doublets. Application of a magnetic field splits the doublets further due to the Zeeman effect, in a pattern reflecting the symmetry of the  $\text{Er}^{3+}$  - related optically active center. The Hamiltonian describing the Zeeman splitting is given by:

$$\mathcal{H} = \mu_B \mathbf{B} \cdot \mathbf{g} \cdot \mathbf{S}, \quad (5.1)$$

with  $\mathbf{S}=1/2$ ,  $\mu_B$  being the Bohr magneton, and the effective  $\mathbf{g}$  tensor exhibiting the symmetry of the center. In general, every PL line corresponding to a transition between two doublets will split into four components, with  $\Delta E = \pm 1/2(|\mathbf{G} - \mathbf{g}|)\beta\mathbf{B}$  for  $\Delta M_S = 0$  transitions and  $\Delta E = \pm 1/2(|\mathbf{G} + \mathbf{g}|)\beta\mathbf{B}$  for  $\Delta M_S = \pm 1$  transitions, where  $\mathbf{G}$  and  $\mathbf{g}$  are the effective  $g$  tensors of the upper and lower doublets, respectively. Figure 5.2 shows the Zeeman effect for the PL line indicated with an arrow in Fig. 5.1. In magnetic fields of up to 5.25 T, the splitting into three components for  $\mathbf{B} \parallel \langle 100 \rangle$  and seven components for  $\mathbf{B} \parallel \langle 011 \rangle$  can be concluded.

Keeping the magnetic field fixed at 5.25 T and rotating its direction in the  $\{011\}$  and  $\{100\}$  planes, we observe a pronounced angular dependence of the line positions. This tells us that the symmetry of the optically active center is lower than cubic. Figure 5.3(a) shows the positions of PL bands for the magnetic field rotated in the  $\{011\}$  plane. As can be concluded, the center has four nonequivalent orientations for an arbitrary direction of  $\mathbf{B}$ . The position of one them is nearly constant for all field orientations – for this line the effective  $g$ -factors of the upper and lower states must be almost equal. Although the angular dependence is complicated by anticrossings among the sublevels, it can be clearly concluded that the center possesses orthorhombic- $I$  ( $C_{2v}$ ) symmetry. For this symmetry type, two of the main tensor axes are oriented along the nonequivalent  $\langle 011 \rangle$  directions, taken as  $x$  and  $y$ , while the  $z$  axis is the  $\langle 100 \rangle$  oriented intersection of the planes perpendicular to  $x$  and  $y$ . We adopt here a description where the spin quantization  $z$  axis is chosen along the tensor axis with the greatest  $g$ -value, in this case one of the  $\langle 011 \rangle$  directions.

It is important to check whether the particular form of the sample, a  $\langle 100 \rangle$ -grown stack, has no influence on the local symmetry of the Er-related center responsible for the observed emission. Figure 5.3(b) illustrates the positions of PL

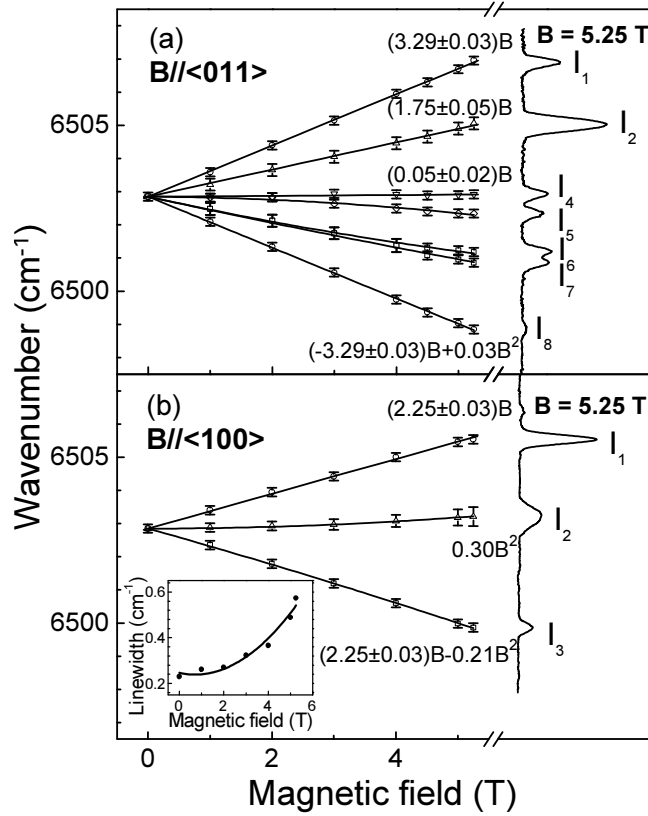


Figure 5.2: Magnetic field induced splitting of the main PL line at  $T=4.2$  K for (a)  $\mathbf{B} \parallel \langle 011 \rangle$  and (b)  $\mathbf{B} \parallel \langle 100 \rangle$ . In the inset, the linewidth of the  $I_2$  component is shown as a function of magnetic field.

bands split by the magnetic field rotated in the  $\{100\}$  plane, from the  $\langle 100 \rangle$  direction perpendicular to the sample surface (the growth direction), through the  $\langle 011 \rangle$ , and again to the  $\langle 100 \rangle$ , but now within the plane of the sample. As can be seen, the observed pattern is fully symmetric within the  $90^\circ$  rotation. We conclude that the layer stacking procedure and the thin-layer form of the sample do not affect the symmetry of the Er-related optically active center, thus making the results of the present study relevant for the Si:Er system in general.

A closer inspection of the angular dependencies in Fig. 5.3 reveals that the splitting towards higher and lower emission energies is not symmetric. This is due to the fact that at high magnetic fields the magnitude of the Zeeman splitting becomes comparable with the crystal field effect and therefore mixing between individual sublevels in the  $J = 15/2$  and  $J = 13/2$  manifolds appears. In the particular case of the investigated PL line, only transitions from lower lying level of the excited state doublet to the lower lying level of the ground state doublet will

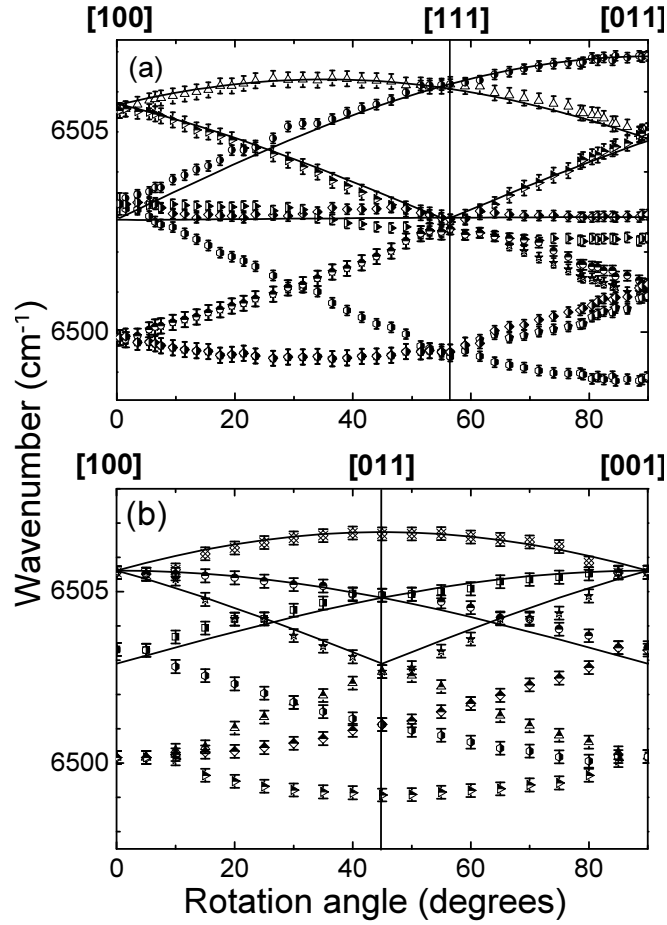


Figure 5.3: Angular dependence of the Zeeman effect of the main PL line (marked with an arrow in Fig. 5.1) at  $B = 5.25$  T for (a) the  $\{011\}$  and (b) the  $\{100\}$  crystallographic planes. Solid lines correspond to simulations see text for the further explanation.

be unaffected, since these are not disturbed by presence of other Er-related levels. In contrast, other lines will show higher order contributions in  $\mathbf{B}$ , complicating the pattern. The transitions occurring from the lower level of the Zeeman split lowest doublet of the excited state are easily identified since their intensity is higher due to partial thermalization. As can be seen from Fig. 5.2, more intense lines occur at higher energies, which thus gives us the additional information that  $|\mathbf{G}| < |\mathbf{g}|$ .

The values of the effective  $g$  tensor  $\mathbf{g}_{eff} = |\mathbf{g} - \mathbf{G}|$  can be determined from the Zeeman splitting shown in Fig. 5.2. For  $\mathbf{B} \parallel \langle 011 \rangle$  - Fig. 5.2(a) - we get  $\Delta g_z = |g_z - G_z| = 3.29 \pm 0.03$ . This value is determined quite accurately since for  $\mathbf{B}$  oriented along the  $z$  tensor axis there are no anticrossing effects. For the components related to  $\Delta g_y$  [ $I_4$  and  $I_5$  lines in Fig. 5.2(a)], the relative intensity of

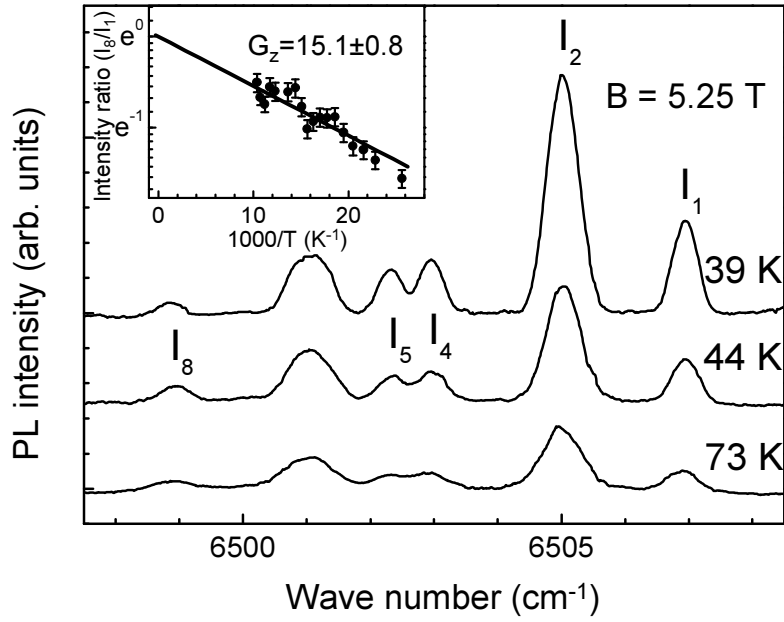


Figure 5.4: Magnetic field induced splitting of the main PL line for  $B = 5.25$  T,  $\mathbf{B} \parallel \langle 011 \rangle$  at temperatures of  $T = 39, 44,$  and  $73$  K. The inset shows the intensity ratio  $I_8/I_1$  fitted assuming thermalization within the upper doublet.

line  $I_4$  does not change with magnetic field and the peak position stays constant, whereas the lower one ( $I_5$ ) shifts towards lower energy as  $B^2$ . The  $\Delta g_y$  value estimated from the linear part of the splitting is less than 0.05. For the central branch [ $I_2$  in Fig. 5.2(a)], we obtain  $g_{eff} = 1.75 \pm 0.05$ . This value is much less accurate as we are in fact dealing with two superposed branches, as can be seen by the growth of the linewidth with increasing  $\mathbf{B}$ , especially for the lower-energy component for which second order effects are considerable. The lowest accuracy is obtained with  $\mathbf{B} \parallel \langle 100 \rangle$  [Fig. 5.2(b)]: the central line broadens strongly with  $\mathbf{B}$  but does not split. The inset to Fig. 5.2(b) shows that the dependence of the linewidth on magnetic field for the central line is not linear with  $\mathbf{B}$ . When rotating magnetic field out of the main direction  $\langle 100 \rangle$ , this feature splits into four lines, of which two do not change with magnetic field, i.e.,  $\Delta g_x = 0$ . We therefore conclude that the angular dependence shown in Fig. 5.3 can be described with the following effective  $g$ -tensor  $\Delta \mathbf{g} = |\mathbf{g} - \mathbf{G}| = [0 \pm 0.02, 0.05 \pm 0.02, 3.29 \pm 0.03]$ . As can be seen from the solid lines in Fig. 5.3, simulation with the Hamiltonian 5.1 gives in this case good agreement with the experimental data.

Unfortunately, one cannot use angular dependencies depicted in Fig. 5.3 to determine the individual  $g$  tensors of the upper and lower doublets  $\mathbf{g}$  and  $\mathbf{G}$ . Assuming full thermalization, these can be estimated from the temperature de-

pendence of the intensity ratio of the high and the low energy components at high field. We note that the components  $I_1$  for  $\mathbf{B}\parallel\langle 100\rangle$  and  $\mathbf{B}\parallel\langle 011\rangle$  increase in intensity with magnetic field, while components  $I_3$  and  $I_8$  for  $\mathbf{B}\parallel\langle 100\rangle$  and  $\mathbf{B}\parallel\langle 011\rangle$ , respectively, decrease due to thermalization within the upper doublet. The intensity ratio of these components follows Boltzmann's distribution, with the activation energy equal to the splitting within the upper doublet. The PL spectra for  $B = 5.25$  T and  $\mathbf{B}\parallel\langle 100\rangle$  at  $T = 39, 44,$  and  $73$  K are illustrated in Fig. 5.4. As shown in the inset to the figure, the temperature dependence of individual PL components allows an estimate of  $|G_z| \cong 15.1 \pm 0.8$  to be made (this is done for a higher temperature range  $T \geq 40$  K, in order to assure full thermalization [82]). The intensity ratio of two components related to  $\Delta g_y = 0.05$  ( $I_4, I_5$ ) is not changing with temperature indicating  $|G_y| \cong 0$ . For components corresponding to  $\Delta g_x = 0$  at  $\mathbf{B}\parallel\langle 100\rangle$ , the central line does not split with magnetic field. We notice that the line remains fully symmetric upon increasing temperature, so that also  $|G_x| \cong 0$ . Therefore both  $|G_x|$  and  $|G_y|$  are very small: i.e., the  $|G_\perp|$  value for the excited state is close to zero. Hence, we are dealing with a particular situation where  $|g_\perp|$  is close to zero for both the ground and the excited state doublets. This gives us the  $\mathbf{g}$  tensor for the ground state doublet  $g_\parallel \cong 18.39 \pm 0.81$  and  $g_\perp \cong 0$ , and results in trace of  $\text{Tr}(\mathbf{g}) \cong 18.4 \pm 1.5$ . The fact that  $g_\perp \cong 0$  implies a low probability of spin transitions within the ground state. This result provides an explanation as to why the  $\text{Er}^{3+}$  - related optically active centers in crystalline silicon have not been detected using magnetic resonance. The situation is similar to that treated by Watkins *et al.* [83] for Au dopant in Si. (When  $g_\perp \cong 0$ , there are no magnetic field dependent off-diagonal terms and no  $\Delta m = \pm 1$  transitions can be induced by microwave field).

If only small axial distortions are present, the average  $g_{av}$  factor can be related to the isotropic cubic  $g_c$  factor [84]  $g_{av} = g_c = \frac{1}{3}(g_\parallel + 2g_\perp)$ . In the present case the average  $g_{av}$  value as defined by is  $6.13 \pm 0.5$ , similar as found for Er in different host materials [77, 84, 85]. For isotropic centers the  $g$  tensors of  $\Gamma_6$  and  $\Gamma_7$  are 6.8 and 6.0, respectively [84, 85]. Therefore in the present case the ground state is likely to be of a  $\Gamma_6$  character, which is in agreement with the previous interpretation of experimental data [76, 77]. The observed orthorhombic- $I$  symmetry is likely to arise from a distortion of a tetrahedrally coordinated  $\text{Er}^{3+}$  ion. This was also recently considered in total energy calculations for the most stable configuration of  $\text{Er}^{3+}$  ion in the crystalline silicon host [86].

## 5.4 Conclusions

In summary, we have provided the most direct microscopic information on the structure of a prominent center responsible for optical activity of Er in crystalline silicon. From a clear Zeeman effect observed on the main line of the Er-1 PL spectrum, the lower than cubic symmetry of the emitting center is confirmed and conclusively identified as orthorhombic- $I$  ( $C_{2v}$ ) with  $\mathbf{g}$  tensor of the ground state  $g_{\parallel} \cong 18.39 \pm 0.81$ ,  $g_{\perp} \cong 0$ . On the basis of these findings, the paramagnetism of the  $\text{Er}^{3+}$ -related center emitting at  $\lambda \simeq 1.5 \mu\text{m}$  is unambiguously established, and our understanding of the important and notoriously difficult Si:Er system has been significantly advanced.

We note that the preferential formation of one type of Er-related optically active center, as confirmed by the success of the reported Zeeman effect study, is a necessary prerequisite for development of efficient photonic devices based on Si:Er.



## Chapter 6

# Microscopic Structure of a Single Type of Optically Active Center in Si/Si:Er Nanostructures

*We present the results of high-resolution photoluminescence and magneto-optical spectroscopy of selectively doped Si/Si:Er nanolayer structures grown by sublimation molecular beam epitaxy method. We show that the annealing of such samples results a preferential formation a single type of optically active Er-related center. Detailed information on the microscopic structure of this center has been revealed from the investigation of the Zeeman effect. Its symmetry is found to be orthorhombic-I ( $C_{2v}$ ) and several  $g$ -tensors of the ground and excited states are determined. The consequences of current findings for the microscopic model of the Er-related center preferentially generated in Si/Si:Er nanolayers are discussed.*

### 6.1 Introduction

The optical properties of rare-earth (RE) atoms in semiconductors are the subject of a considerable amount of research due to the potential applications in optoelectronics [68, 69, 70, 72, 87]. The large interest in this field is motivated by the fact that these ions exhibit sharp, atomic-like, intra- $4f$  optical transitions with temperature-independent wavelengths. Optical excitation of RE ions incorporated into glasses and ceramic materials is commonly used for lasers and optical amplifiers. In contrast to insulators, the major advantage of placing a RE ion in a semiconductor matrix is the possibility to excite its intra- $4f$  transition electrically through a carrier-mediated process. In particular, erbium-doped silicon has attracted much attention. This is for two main reasons. Firstly, the transition of

the erbium ion from the first excited state to the ground state is in the  $1.5 \mu\text{m}$  range which coincides with the optical window of glass fibers currently used for telecommunications. Secondly, this system can be easily integrated with devices manufactured using the highly successful standard silicon technology. Also, Si:Er light emitting structures are attractive in association with potential applications for optical interconnects in future photonic chip technology. As a result of a continuing research effort Si:Er-based light emitting diodes have now been successfully developed – for an up-to-date review, see, e.g., [71, 88].

Unlike the well - investigated Yb in InP,  $\text{Er}^{3+}$  ion in a semiconductor matrix tends to form a variety of centers, resulting in multiplicity of photoluminescence (PL) spectra and, consequently, inhomogeneous broadening of emission lines. GaAs:Er prepared by ion implantation or by molecular beam epitaxy (MBE) exhibits a broad emission band around  $\lambda = 1.5 \mu\text{m}$  indicating simultaneous generation of several Er-related centers rather than formation of a single center with a well-defined structure [89]. A preferential production of one of the centers, however, was obtained for GaAs:Er by adjusting the MBE growth parameters. Zeeman effect [90] and PL excitation [91] studies revealed low-symmetry of this Er-related center. Selective development of a different Er-related center in GaAs was reported upon co-doping with oxygen in the ambient during the MOCVD growth. Also in this case, the spectral linewidth was sufficiently narrow to allow for structural investigations, and an  $\text{ErO}_2$  cluster was proposed as a microscopic model for the relevant optical center [92]. This model was further corroborated by observation and analysis of the Zeeman effect [93, 94].

In contrast to GaAs:Er, very little is known on the microscopic structure of  $\text{Er}^{3+}$ - related optically active centers in silicon. This is very unfortunate, when bearing in mind the prominent position of Si:Er with respect to applications. Some information on microscopic structure of centers responsible for Er-related  $1.5 \mu\text{m}$  emission in Si was revealed by a high-resolution PL study which identified more than 100 emission lines [76]. These were assigned to several, simultaneously present Er-related centers. In contrast to GaAs:Er, and also to GaN:Er, individual centers in Si:Er cannot be separated by excitation spectroscopy. The microscopic structure was investigated also using extended X-ray-absorption fine structure (EXAFS), and the presence of oxygen in the immediate surrounding of the optically active Er atom was concluded [73]. Formation of an Er-related cubic center was found in channeling experiments [74], which identified an isolated Er ion at a tetrahedral interstitial site as the main center generated in crystalline silicon by Er implantation. This finding was in agreement with theoretical calculations predicting tetrahedral interstitial location of an isolated Er in Si [75]. Unfortunately, neither channeling experiments nor total energy calculations have shown whether

the identified high-symmetry Er centers are responsible for the emission observed in PL measurements. Also electron paramagnetic resonance (EPR), the experimental technique commonly applied to identify the microstructure of defects, has not been, so far, particularly successful in the case of the optically active Er-related centers in crystalline silicon [77].

Structural information on optically active centers could be provided by magneto-optical studies. Unfortunately, in spite of numerous attempts, no successful observation of Zeeman effect in PL has been reported for Si:Er. Due to the aforementioned inhomogeneous character of the linewidth, application of magnetic field results in broadening and subsequent vanishing of emission lines. Realization of preferential formation of a single type of optically active Er-related centers is decisive for the future of Si:Er as photonic material. This goal is not achieved in “standard” Si:Er materials prepared by ion implantation, where a large variety of Er-related optically active centers are simultaneously generated [76]. Recently, we have confirmed [95] that the preferential production of a single type of optically active Er-related centers can be realized in Er-doped Si nanolayers grown by sublimation MBE (SMBE) [79, 80]. Using this technique, a sandwich structure of interchanged Si/Si:Er nanolayers can be grown. In this case, a high concentration of a specific center (labeled Er-1) was found. One can expect that in SMBE-grown multilayer structures of alternating Si and Si:Er layers [79, 80], conditions necessary for realization of efficient PL, i.e. high  $\text{Er}^{3+}$  ions concentration and efficient exciton generation, can be met simultaneously. Upon illumination with a laser beam, excitons generated in undoped Si spacer regions diffuse into doped layers and provide excitation of  $\text{Er}^{3+}$  ions. Moreover, we have established that spectral characteristics of emission related to the Er-1 center indicate a possibility  $\sim 10^3$  higher value of absorption cross section, when compared to the implanted Si:Er materials used so far. Therefore the Er-1 center emerges as a plausible candidate for realization of optical gain in Si:Er.

In this Chapter we present an investigation of the Zeeman effect of the Er-1 center - the first Er-related optical center which can be preferentially produced in silicon. Highlights of the preliminary analysis of results of this study have been given in the preceding Chapter [95].

## 6.2 Sample preparation and experiment

The SMBE method is a modification of MBE, in which fluxes of Si and dopants are produced by sublimation of appropriate current-heated sources [96]. SMBE allows to grow both uniformly and selectively doped Si:Er structures with a minimum number of defects and a high concentration of dopants. We investigate here a

Table 6.1: Sample labels, sample parameters and annealing treatments for the investigated samples

Sample label	$d_{\text{Si:Er}}$ (nm)	$d_{\text{Si}}$ (nm)	$N$	$\Sigma d_{\text{Si:Er}}$ ( $\mu\text{m}$ )	$I_{\text{Si:Er}}$ (normalized)
#51	2.3	1.7	400	0.92	6.6
#52	2.3	6.5	196	0.45	11.4
#53	50	50	16	0.80	6.8
#54	6.2	31.3	44	0.27	30.5
#56	5.0	100	19	0.095	49.3
#37	1800	-	1	1.8	2.9
J900	200	-	-	-	1

novel type of selectively doped Si/Si:Er/Si/Si:Er/.../Si multilayer structures of thin ( $\delta$ ) Si:Er layers alternating with Si spacers. The extraordinary properties of this material and, in particular, the strong enhancement of PL will be discussed.

The Si:Er layers used in this study were grown by SMBE on Si(100)  $p$ -type substrates ( $\rho \approx 10 - 20 \Omega\text{cm}$ ) under pressure of  $2 \times 10^{-7}$  mbar. The growth temperatures ( $T_{gr}$ ) were 430 – 700 °C. The PL intensity in a uniformly doped SMBE layer (a single layer) is most intense at a growth temperature of about 560 °C. To grow Er-doped silicon layers, polycrystalline Si plates intentionally doped with Er were used as a source for both Er and Si fluxes. The growth rate was varied from 0.3 to 5  $\mu\text{m}/\text{h}$  and uniformly doped Si:Er layers with a thickness from 0.2 to 6  $\mu\text{m}$  were obtained. For the selectively doped Si/Si:Er/Si/Si:Er/.../Si multilayer structures, a thickness of Er-doped Si layers,  $d_{\text{Si:Er}}$ , was 2.0 – 50 nm, the thickness of Si space layers,  $d_{\text{Si}}$ , was 1.7 – 100 nm and the number of periods was  $N = 16 - 400$ . Following the SMBE growth procedure, an additional annealing of the structures was carried out in a nitrogen or hydrogen flow at 800 °C for 30 minutes [79, 80]. The concentration of Er in Si:Er layers was determined to be  $3.5 \times 10^{18} \text{ cm}^{-3}$ . Table 6.1 shows the list of samples used in this research. For comparison, an implanted sample (labeled J900) has been added. This sample has been prepared by Er (energy 320 keV, dose  $3 \times 10^{12} \text{ cm}^{-2}$ ) and O (energy 40 keV, dose  $3 \times 10^{13} \text{ cm}^{-2}$ ) implantations followed by 900 °C/30 min. anneal in nitrogen.

In the experiments, samples were excited using a cw argon-ion laser operating at 514.5 nm or 488 nm. All spectra were obtained with either a 1.0 m or 1.5 m F/8 monochromator (Jobin-Yvon THR-1000/THR-1500 equipped with a 900 grooves/mm grating blazed at 1.5  $\mu\text{m}$ ) and detected by a high sensitivity germa-

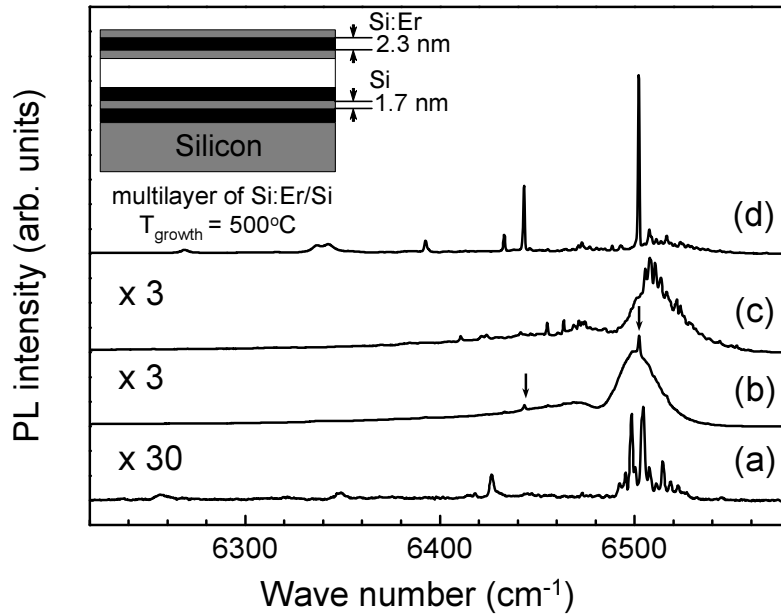


Figure 6.1: PL spectra of a Si:Er sample prepared by implantation (a), the uniformly doped SMBE layer grown at 560 °C (b), the selectively doped SMBE as grown at 520 °C (c), and following a short annealing at 800 °C for 30 min. (d). All the spectra have been recorded at 4.2 K under Ar<sup>+</sup>-ion laser excitation. In the inset, the multilayer structure of the SMBE grown sample is schematically illustrated.

nium detector (Edinburgh Instruments). Optical measurements were performed using a variable temperature continuous flow cryostat accessing the 1.5 – 300 K range (Oxford Instruments Optistat CF). For the Zeeman experiments, the sample was placed in a split-coil superconducting magnet with optical access (Spectromag 8). The magnetic field was varied from 0 up to 6 T.

## 6.3 Photoluminescence

Figure 6.1 compares the 6500 cm<sup>-1</sup> Er-related emission band from a “standard” J900 sample prepared by ion implantation (trace a) with that observed in the SMBE grown samples (traces b, c, d).

We used a uniformly doped SMBE sample (#37) with the highest total intensity of the integrated PL signal, a selectively doped SMBE sample (#51), and the sample #51 following a short annealing. The measurements were taken at 4.2 K under identical conditions for all the samples. We point out that the preparation conditions of the ion-implanted sample were optimized in such a way as to obtain

maximal PL signal [97]. Nevertheless, the Si:Er layers grown by the SMBE method show stronger emission.

The PL spectrum of the uniformly doped SMBE layer is shown in Fig. 6.1, trace b. As can be seen, the PL intensity obtained in the SMBE grown sample (#37) exceeds considerably that of the ion implanted one. A broad spectral band is seen around the energy of  $6506 \text{ cm}^{-1}$  with the width about  $25 \text{ cm}^{-1}$ . It was suggested to originate from Er complexes of the so-called  $\text{SiO}_2$ -precipitate type center [97]. Along with the precipitate center, also the PL spectrum of the Er-1 center (marked by arrows in Fig. 6.1) can be distinguished. This spectrum has been reported before [79, 80] and assigned to a low-symmetry Er-related center.

The sample #51 consists of 400 Si:Er layers of 2.7 nm thickness interlaced by 1.7 nm Si spacers. The structure is schematically depicted in the inset to Fig. 6.1. The PL spectrum of the as grown sample #51 is presented in Fig. 6.1, trace c. It has high intensity and shows multiple sharp features superimposed on a relatively broad band.

Detailed investigations revealed that at low temperature, the integrated intensity of the Er-related PL in optimized multilayer structures can be an order of magnitude higher than from a single Si:Er layer of an equal Er-doped volume. The intensity increase was found to depend strongly on the thickness and number of the undoped Si spacer layers. Table 6.1 lists the structure parameters for several of the investigated samples together with the integrated PL intensity ( $I_{\text{Si:Er}}$ ) normalized for the same volume of Er doped layers and scaled with respect to the implanted sample. This is obtained by dividing the PL intensity over the total thickness  $\Sigma d_{\text{Si:Er}}$  and the intensity of J900. It can be seen that  $I_{\text{Si:Er}}$  increases with increasing thickness of the spacer layer up to 50 nm, at which point it exceeds the  $I_{\text{Si:Er}}$  intensity of the uniformly doped Si:Er layer by more than an order of magnitude. The enhancement of the luminescence intensity in the multilayer structures as compared to uniformly doped layers may be related to more efficient Er excitation. As known, the maximum values for quantum efficiency and PL intensity in Si:Er structure are reached at low temperatures when excitation of  $\text{Er}^{3+}$  occurs through of an intermediate state with participation of an exciton. One may speculate that in a multilayer structure, excitons efficiently generated in Si spaces have long lifetime and can subsequently diffuse towards Er doped regions. In that way they provide an excitation additional to that by excitons induced in the Si:Er layer.

Annealing considerably alters PL characteristics of the multilayer structure - see trace d in Fig. 6.1. While the total intensity of emission changes only slightly, the spectrum undergoes an important transformation: the broad band disappears and a small number of sharp and intense lines of the Er-1 PL spectrum remain.

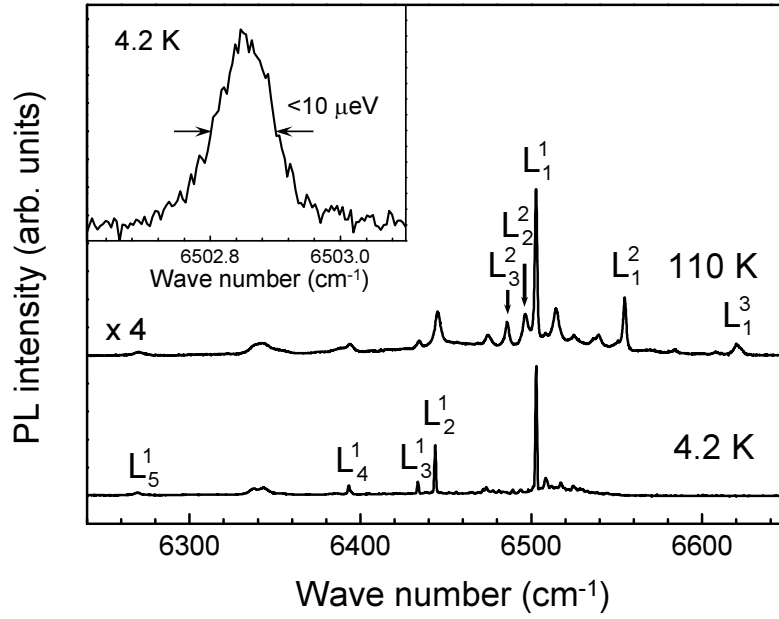


Figure 6.2: *PL spectra of the annealed #51 sample as measured at 4.2 and 110 K. For line positions, symbols, and halfwidths, see Table 6.2. The inset shows a high-resolution scan of the most intense,  $L_1^1$  line, of the Er-1 spectrum.*

This is illustrated in Fig. 6.2, for measurements taken at 4.2 and 110 K. The inset shows a high-resolution scan of the main feature of the Er-1 spectrum. As can be seen, the real width of this PL line is measured to be extremely small  $\Delta E \leq 0.08 \text{ cm}^{-1}$  ( $10 \mu\text{eV}$ ). To our best knowledge, this is among the smallest values ever measured for any emission band in a semiconductor matrix. At low temperature, below 25 K, the Er-1 spectrum consists of a set of narrow intense lines at energies of 6502.85, 6443.72, 6433.59, 6393.17  $\text{cm}^{-1}$ . For further reference we label these line 1 ( $L_1^1$ ), line 2 ( $L_2^1$ ), line 3 ( $L_3^1$ ), and line 4 ( $L_4^1$ ), respectively. At higher temperatures other lines, labeled hot line 1 ( $L_1^2$ ), hot line 2 ( $L_2^2$ ), hot line 3 ( $L_3^2$ ), and a second hot line 1 ( $L_1^3$ ), appear at 6554.82, 6496.03, 6485.65, and 6620.97  $\text{cm}^{-1}$ , respectively. The intensities of these lines rapidly increase with increasing temperature while, at the same time, the intensities of the lines  $L_1^1$ ,  $L_2^1$ ,  $L_3^1$ ,  $L_4^1$  decrease. These details of the spectra are presented in Table 6.2. We note that the hot lines are displaced by about 52  $\text{cm}^{-1}$ .

Temperature dependence of luminescence has been investigated in more detail in order to determine the electronic level scheme of the optically active center responsible for the Er-1 spectrum. The temperature was varied between 4.2 K and 160 K. The intensity ratios of the lines  $L_1^2$ ,  $L_2^2$ ,  $L_3^2$  to that of  $L_1^1$ ,  $L_2^1$ ,  $L_3^1$ , obtained from the measurements, are plotted as a function of temperature in Fig.

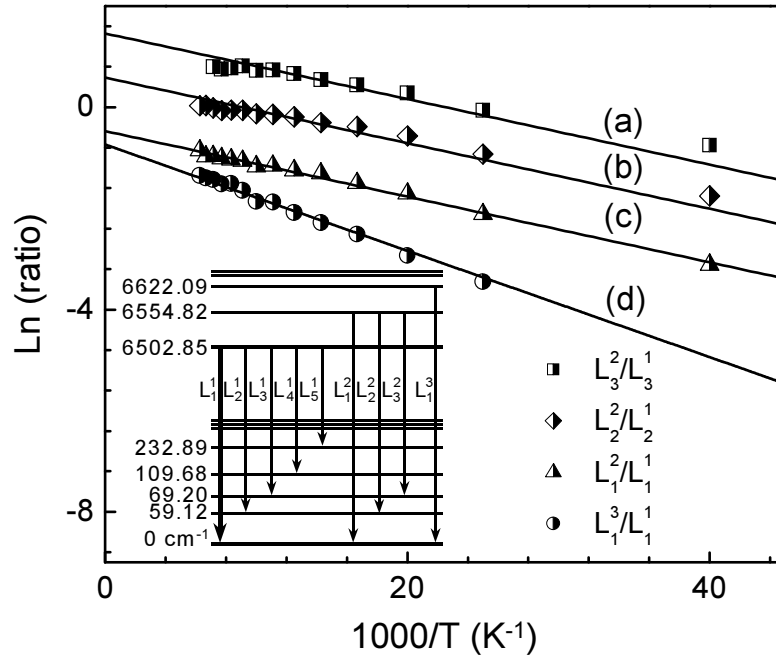


Figure 6.3: Arrhenius plots of the temperature variation of the intensity ratios of the hot line 1 ( $L_1^2$ ) relative to the line 1 ( $L_1^1$ ) (triangles); the hot line of line 2 ( $L_2^2$ ) relative to the line 2 ( $L_2^1$ ) (diamonds); the hot line of line 3 ( $L_3^2$ ) relative to the line 3 ( $L_3^1$ ) (squares). The activation energies are found to be  $\Delta E \simeq 50 \text{ cm}^{-1}$ , equal to the spectroscopic splitting. The intensity ratio of the second hot line  $L_1^3$  relative to line 1 ( $L_1^1$ ) (circles) is shown as trace d; it has an activation energy of  $72 \pm 8 \text{ cm}^{-1}$ , equal to the  $L_1^3$  to  $L_1^2$  energy separation.

6.3 (trace c, b, and a, respectively). From the Arrhenius plot, we conclude the same activation energy of  $49 \pm 3 \text{ cm}^{-1}$  for all of them. This value is in good agreement with separation of lines  $L_1^2, L_2^2, L_3^2$  to the lines  $L_1^1, L_2^1, L_3^1$ , ( $51.97, 52.31, 52.06 \text{ cm}^{-1}$ , respectively). Also, the intensity ratio of the lines  $L_1^3$  to that of  $L_1^2$  has an activation energy of  $72 \pm 8 \text{ cm}^{-1}$  (trace d), very similar to the spectroscopic splitting of  $L_1^3$  and  $L_1^2$ , ( $66.51 \text{ cm}^{-1}$ ).

Based on the PL investigation we can interpret the observed structure of the spectrum at low temperature as transitions from the lowest excited state to the crystal field split ground state. At elevated temperatures satellites of these lines can be detected, as shown in Fig. 6.2. They are shifted by 52 and  $118 \text{ cm}^{-1}$  (6.4 and 14.6 meV) towards higher energies for each transition, and can be associated with transitions originating at the second and the third crystal field split levels of the excited state. Such an energy level diagram responsible for PL of the Er-1 center is shown in the inset to Fig. 6.3.

Table 6.2: Labeling and spectroscopic parameters of the Er-related photoluminescence lines.

Transition	Label	$h\nu$ ( $\text{cm}^{-1}$ )	Displacement ( $\text{cm}^{-1}$ )
Line 1	$L_1^1$	6502.85	
Line 2	$L_2^1$	6443.72	- 59.13 from $L_1^1$
Line 3	$L_3^1$	6433.59	- 69.26 from $L_1^1$
Line 4	$L_4^1$	6393.17	- 109.68 from $L_1^1$
Line 5	$L_5^1$	6269.96	- 232.89 from $L_1^1$
Hot line 1	$L_1^2$	6554.82	51.97 from $L_1^1$
Hot line 2	$L_2^2$	6496.03	52.31 from $L_2^1$
Hot line 3	$L_3^2$	6485.65	52.06 from $L_3^1$
Second hot line 1	$L_1^3$	6620.97	66.51 from $L_1^2$

## 6.4 Zeeman splitting of the PL lines

### 6.4.1 Introduction: theoretical considerations

The electronic configuration of  $\text{Er}^{3+}$  is  $4f^{11}$  with a ground state  $^4I_{15/2}$  and a first excited state  $^4I_{13/2}$ . In a crystal field with  $T_d$  symmetry the ground state ( $^4I_{15/2}$ ) will split into two doublets,  $\Gamma_6$  and  $\Gamma_7$ , and three  $\Gamma_8$  quadruplets, whereas the first excited state ( $^4I_{13/2}$ ) splits into  $2\Gamma_6 + \Gamma_7 + 2\Gamma_8$ . This splitting is described by the crystal field Hamiltonian [98]:

$$\mathcal{H} = B_4(O_4^0 + 5O_4^4) + B_6(O_6^0 - 21O_6^4), \quad (6.1)$$

where  $O_l^m$  are Steven's equivalent operators and the  $B_l$  are adjustable parameters related to the strength of the crystal field components. Alternatively, the Hamiltonian can be expressed in the notation introduced by Lea, Leask, and Wolf (LLW) [81, 99]:

$$\mathcal{H} = \frac{Wx}{F(4)} (O_4^0 + 5O_4^4) + \frac{W(1-|x|)}{F(6)} (O_6^0 - 21O_6^4). \quad (6.2)$$

The parameters  $W$  and  $x$  are related to  $B_4$  and  $B_6$  as  $B_4F(4) = Wx$ ,  $B_6F(6) = W(1-|x|)$ .  $W$  is an energy scale factor. The dimensionless parameter  $x$  can take values from 0 to  $\pm 1$ , which covers the range of the  $B_4/B_6$  ratios between 0 and  $\pm\infty$ . Negative values of  $x$  correspond to tetrahedral coordination, whereas positive values of  $x$  occur for octahedral coordination. The factors  $F(4)$  and  $F(6)$  are introduced to keep the eigenvalues in the same numerical range for all ratios

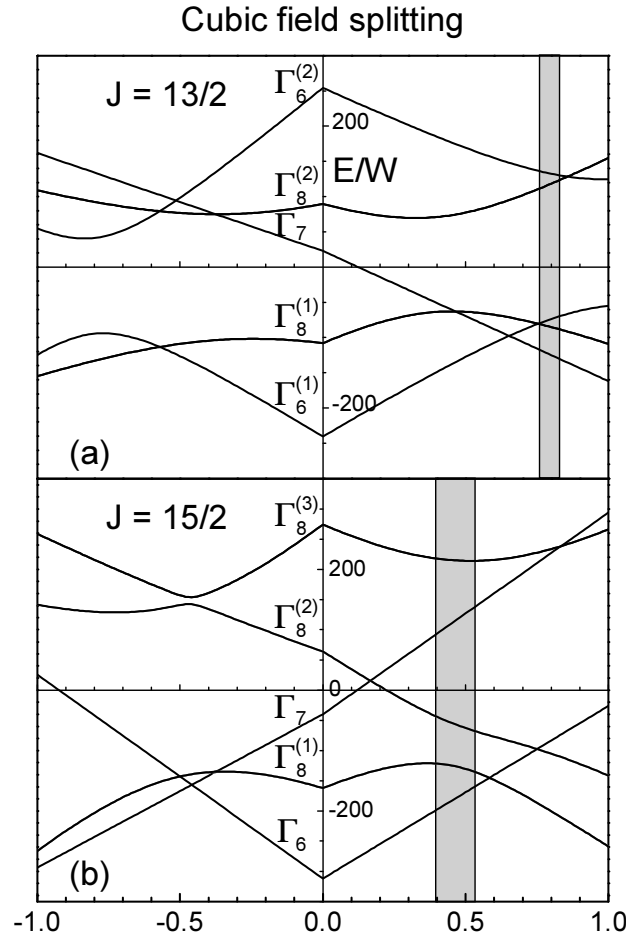


Figure 6.4: The energy-level splitting of a  $J = 15/2$  (a) and a  $J = 13/2$  (b) manifold by a cubic crystal field of  $T_d$  symmetry Ref. [81]. Possible locations of the ground and the first excited states of the Er-1 center are indicated.

of the 4<sup>th</sup>- to 6<sup>th</sup>- degree terms. For  $J = 15/2$ ,  $F(4) = 60$ ,  $F(6) = 13860$  and for  $J = 13/2$ , they are 60 and 7560, respectively [81]. In Fig. 4 we reproduce the LLW calculations of the eigenvalues for  $J = 15/2$  and  $J = 13/2$ . The state labeling is that for  $T_d$  symmetry [85]. Note that all matrix elements, and hence all eigenvalues, are proportional to  $W$ ; in Fig. 6.4 they are presented with the energy scale parameter set to  $W = 1 \text{ cm}^{-1}$ , and are functions of  $x$  only.

The eigenfunctions expressed in the basic states  $|M_J\rangle$  are either of the form:

$$|\psi_1, \mp\rangle = \mp (a_1 |\pm \frac{15}{2}\rangle + a_2 |\pm \frac{7}{2}\rangle + a_3 |\mp \frac{1}{2}\rangle + a_4 |\mp \frac{9}{2}\rangle) \quad (6.3a)$$

for  $J = 15/2$ , and

$$|\psi_2, \mp\rangle = \mp (b_1 |\pm \frac{7}{2}\rangle + b_2 |\mp \frac{1}{2}\rangle + b_3 |\mp \frac{9}{2}\rangle) \quad (6.3b)$$

for  $J = 13/2$ , or

$$|\psi_3, \mp\rangle = \mp (c_1 |\pm \frac{13}{2}\rangle + c_2 |\pm \frac{5}{2}\rangle + c_3 |\mp \frac{3}{2}\rangle + c_4 |\mp \frac{11}{2}\rangle) \quad (6.4)$$

for both  $J = 15/2$  and  $13/2$ . In an external magnetic field the degeneracy of the crystal-field split levels is lifted. The splitting of the doublet states can be described by an effective spin  $\tilde{S} = 1/2$  and labeling of the state  $|\mp\rangle$ . If the Zeeman interaction is much smaller than the crystal field splitting, the Zeeman interaction has the form:

$$\mathcal{H} = g\mu_B \mathbf{B} \cdot \tilde{\mathbf{S}}, \quad (6.5)$$

where  $\mu_B$  being the Bohr magneton, and  $g$  the effective  $g$ -value.

The coefficients in Eqs. 6.3a and 6.3b can be uniquely determined for the  $\Gamma_7$  doublets and those in Eq. 6.4 for the  $\Gamma_6$  doublet. The effective  $g$ -factors of these states can be easily calculated ( $g = 2g_J \sum_{M_J} a_J^2 M_J$ , where  $g_J$  is the Landé factor). The Landé  $g$ -factor of the free  $\text{Er}^{3+}$  ions is  $g_J = \frac{6}{5}$  for the pure ground state  $^4I_{15/2}$ , and  $g_J = \frac{72}{65}$  for the pure first excited state  $^4I_{13/2}$ . In  $T_d$  symmetry the (isotropic) effective  $g$ -factors are thus 6.80 and 6.00 for the  $\Gamma_6$  and  $\Gamma_7$  symmetry doublets, respectively, of a pure  $^4I_{15/2}$  manifold, while for the  $\Gamma_7$  doublet of the  $^4I_{13/2}$  multiplet  $g = 5.54$ . For all the other states the coefficients in the wavefunctions, and hence the effective  $g$ -factors, depend on crystal field parameters.

The quadruplets  $\Gamma_8$  can be described by an effective spin of  $\tilde{S} = 3/2$ , where the  $M_{\tilde{S}} = \mp \frac{1}{2}$  states have the form given by Eqs. 6.3a and 6.3b and the  $M_{\tilde{S}} = \mp \frac{3}{2}$  states have the form given by Eq. 6.4. The Zeeman interaction for a  $\Gamma_8$  quadruplet is more complicated than that for the ordinary  $J = 3/2$  quadruplet, as there are nonvanishing matrix elements between the  $M_{\tilde{S}} = \mp \frac{3}{2}$  wavefunctions. The Hamiltonian describing the Zeeman interaction within a  $\Gamma_8$  quadruplet can be expressed by [100]:

$$\mathcal{H} = g_J \mu_B \left( a \mathbf{B} \cdot \tilde{\mathbf{S}} + b \left( B_x \tilde{S}_x^3 + B_y \tilde{S}_y^3 + B_z \tilde{S}_z^3 \right) \right). \quad (6.6)$$

The parameters  $a$  and  $b$  can be expressed also as:  $a = -P/12 + 9Q/4$ ,  $b = P/3 - Q$ , where  $P$  and  $Q$  are the expectation values of  $\left( a \mathbf{B} \cdot \tilde{\mathbf{S}} + b \left( B_x \tilde{S}_x^3 + B_y \tilde{S}_y^3 + B_z \tilde{S}_z^3 \right) \right)$  for  $|+\frac{3}{2}\rangle$  and  $|+\frac{1}{2}\rangle$  states, respectively. In an ordinary  $J = 3/2$  quadruplet  $P = 3Q$  and, in consequence,  $b = 0$ .

In a free ion electric dipole (ED) transitions between the levels of the  $4f^n$  configuration are parity forbidden and only magnetic dipole transitions (MD) are expected. However, the crystal field of the host material may break the inversion symmetry and admix states of opposite parity via odd terms in the crystal field potential, which makes ED transitions partly allowed. The selection rules governing optical transitions between Zeeman split levels of  $\text{Er}^{3+}$  are the following: MD

Table 6.3: The selection rules of the ED and MD transitions

	$\Gamma_6  +\rangle$	$\Gamma_6  -\rangle$	$\Gamma_7  +\rangle$	$\Gamma_7  -\rangle$
$\Gamma_6  +\rangle$	MD	MD	ED	0
$\Gamma_6  -\rangle$	MD	MD	0	ED
$\Gamma_7  +\rangle$	ED	0	MD	MD
$\Gamma_7  -\rangle$	0	ED	MD	MD
$\Gamma_8 \left +\frac{3}{2}\right\rangle$	MD+ED	MD+ED	MD+ED	0
$\Gamma_8 \left +\frac{1}{2}\right\rangle$	MD+ED	0	MD+ED	MD+ED
$\Gamma_8 \left -\frac{1}{2}\right\rangle$	0	MD+ED	MD+ED	MD+ED
$\Gamma_8 \left -\frac{3}{2}\right\rangle$	MD+ED	MD+ED	0	MD+ED

transitions can occur between states of  $\Delta J = 0, \pm 1$ ,  $\Delta M_J = 0, \pm 1$ , whereas ED transitions can occur between states with  $\Delta J \leq 6$ ,  $\Delta M_J = 0, \pm 1$ . The  $T_d$  symmetry imposes further restrictions on the selection rules: transitions between two doublets of the same symmetry are only MD allowed, whereas those between  $\Gamma_6$  and  $\Gamma_7$  doublets are only ED allowed. Moreover, in the latter case only  $|\pm\rangle \leftrightarrow |\pm\rangle$  transitions can occur. Transitions to and from a  $\Gamma_8$  quadruplet are both ED and MD allowed [101]. The allowed transitions in pure  $T_d$  symmetry are summarized in Table 6.3. According to these selection rules, for  $\text{Er}^{3+}$  in a site of  $T_d$  symmetry we should expect, assuming that the initial state is a doublet, the following number of Zeeman components: 2 for emission terminating on a doublet of the other symmetry, 4 for a doublet of the same symmetry and 6 components for the emission terminating on either of the 3 quadruplets. We will refer to Table 6.3 frequently in the following sections, as it will turn out that the optical transitions of the Er center under investigation closely follow the selection rules for the cubic symmetry.

In a crystal field of lower than cubic symmetry the  ${}^4I_{15/2}$  and  ${}^4I_{13/2}$  will split into 8 and 7 Kramers' doublets, respectively. In particular, in an orthorhombic- $I$  ( $C_{2v}$ ) crystal field all the doublets would be of the same  $\Gamma_5$  symmetry and optical transitions between them would be MD and ED allowed. The crystal field splitting is described by the following Hamiltonian:

$$\mathcal{H} = B_2^0 O_2^0 + B_2^2 O_2^2 + B_4^0 O_4^0 + B_4^2 O_4^2 + B_4^4 O_4^4 + B_6^0 O_6^0 + B_6^2 O_6^2 + B_6^4 O_6^4 + B_6^6 O_6^6. \quad (6.7)$$

Here two of the quantization axes are oriented along nonequivalent  $\langle 011 \rangle$  directions perpendicular to each other, taken as  $x'$  and  $y'$ , while the  $z'$  axis is the  $\langle 100 \rangle$  oriented intersection of the planes, perpendicular to  $x'$  and  $y'$ . The Zeeman interaction Hamiltonian for well separated doublets (where second order effects can be

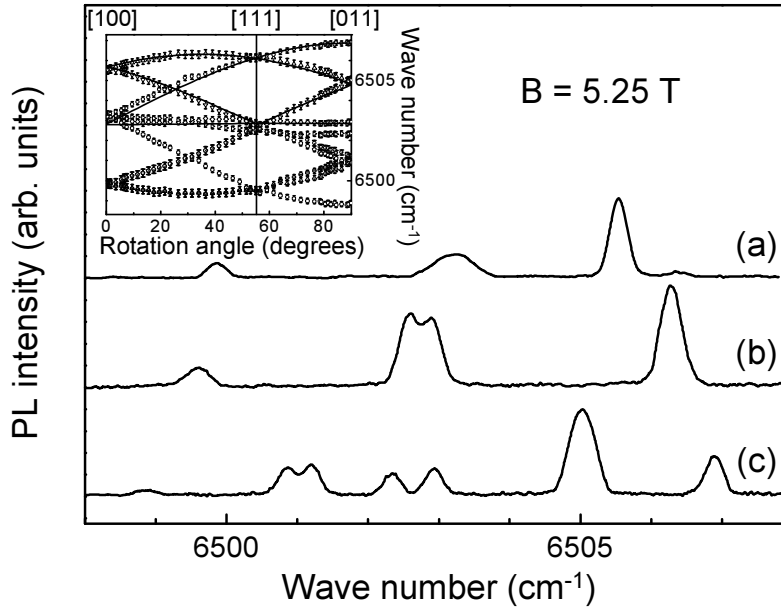


Figure 6.5: Zeeman effect for the main PL line  $L_1^1$  at 4.2 K for magnetic field of 5.25 T oriented along the main crystal directions (a)  $\mathbf{B} \parallel \langle 100 \rangle$ , (b)  $\mathbf{B} \parallel \langle 111 \rangle$ , and (c)  $\mathbf{B} \parallel \langle 011 \rangle$ . Inset to the figure: angular dependence of the Zeeman effect for the line  $L_1^1$  at  $B = 5.25$  T for the (011) crystallographic plane.

ignored) takes the form:

$$\mathcal{H} = \mu_B \mathbf{B} \cdot \mathbf{g} \cdot \tilde{\mathbf{S}}, \quad (6.8)$$

where  $\mathbf{g}$  is now a tensor with the main axes oriented along  $x'$ ,  $y'$ , and  $z'$ .

If the distortion of cubic symmetry is small, *i.e.*, the splitting of the quadruplets is much smaller than the distance to the next “cubic” level, the influence of Hamiltonian (7) on a  $\Gamma_8$  quadruplet can be expressed by the so-called quadrupole term,  $\tilde{\mathbf{S}} \cdot \mathbf{D} \cdot \tilde{\mathbf{S}}$ , which in the defect axes takes the form [98]:

$$\mathcal{H} = D \left( \tilde{S}_z^2 - \frac{1}{3} \tilde{S} (\tilde{S} + 1) \right) + E \left( \tilde{S}_x^2 - \tilde{S}_y^2 \right), \quad (6.9)$$

The total Hamiltonian, which needs to be considered is:

$$\mathcal{H} = \mu_B g_J \left( a \mathbf{B} \cdot \tilde{\mathbf{S}} + b \left( B_x \tilde{S}_x^3 + B_y \tilde{S}_y^3 + B_z \tilde{S}_z^3 \right) \right) + \tilde{\mathbf{S}} \cdot \mathbf{D} \cdot \tilde{\mathbf{S}}. \quad (6.10)$$

### 6.4.2 Splitting of line $L_1^1$

The Zeeman splitting of the main PL line  $L_1^1$  measured at 4.2 K in magnetic field of 5.25 T is shown in Fig. 6.5. For the field oriented along the principal directions, three Zeeman components for  $\mathbf{B} \parallel \langle 100 \rangle$ , four components for  $\mathbf{B} \parallel \langle 111 \rangle$

and seven components for  $\mathbf{B} \parallel \langle 011 \rangle$  can be seen. The angular dependence of the line positions, measured at 5.25 T in the  $\{011\}$  crystal plane from  $[001]$  direction to  $[011]$ , is depicted in the inset of Fig. 6.5. The clearly observed strong dependence of the Zeeman splitting on the orientation of the magnetic field indicates that the center has lower than cubic symmetry. The center has only four nonequivalent orientations for an arbitrary direction of  $\mathbf{B}$  in this plane, with two orientations for  $\mathbf{B}$  along  $\langle 100 \rangle$  and  $\langle 111 \rangle$  directions, and three for  $\langle 001 \rangle$  direction. This is a clear and unambiguous signature of orthorhombic- $I$  ( $C_{2v}$ ) symmetry. As explained in detail in Ref. [95], the angular as well as the magnetic field dependencies can be only described with  $g_x^{(1)} = G_x^{(1)} = 0 \pm 0.1$ ,  $g_y^{(1)} - G_y^{(1)} = 3.3 \pm 0.1$ , and  $g_z^{(1)} = G_z^{(1)} = 0 \pm 0.1$ , where  $\mathbf{g}^{(1)}$  and  $\mathbf{G}^{(1)}$  refer to  $g$ -tensor values for the  $J = 15/2$  and  $J = 13/2$  manifolds, respectively, and the superscript denotes the position of the level in the manifold. For sake of consistency we point out that in our preliminary analysis in Chapter 5 [95] a different tensor axes set was adopted, with the  $z$  axis chosen as the one with the only nonvanishing  $g$ -value. The solid lines in the inset to Fig. 6.5 show the peak positions calculated with use of Eq. 6.8 for  $|\pm\rangle \leftrightarrow |\pm\rangle$  transitions, which were the only ones observed. Hence, the individual  $g$ -tensors of the upper and lower doublets  $\mathbf{g}^{(1)}$  and  $\mathbf{G}^{(1)}$  could not be determined. The values were estimated from the temperature dependence of the intensity ratio of the high and the low energy Zeeman components at high field, under assumption of full thermalization, to be  $\mathbf{G}^{(1)} = [0 \pm 0.1, 15.1 \pm 0.8, 0 \pm 0.1]$ , which implied  $\mathbf{g}^{(1)} = [0 \pm 0.1, 18.4 \pm 0.8, 0 \pm 0.1]$  [95].

The  $g$ -tensor values  $\mathbf{G}^{(1)}$  for the excited state can be determined with a better accuracy from the analysis of the Zeeman splitting of the line  $L_4^1$ , presented in the next subsection, of which transitions with the difference as well as the sum of the effective  $g$ -factors of the ground and excited states were observed. We will, therefore, defer the discussion of the determined  $g$ -tensor values until later. We would only like to point out at this stage that despite the anisotropy of the  $g$ -tensor determined here, the optical transitions remarkably resemble those expected between doublets of different type in  $T_d$  symmetry (Table 6.3).

### 6.4.3 Splitting of line $L_4^1$

The Zeeman splitting of line  $L_4^1$ , as measured at 4.2 K for two orientations of the magnetic field  $\mathbf{B} \parallel \langle 100 \rangle$  and  $\mathbf{B} \parallel \langle 011 \rangle$ , is shown in Figs. 6.6(a) and 6.6(b), respectively. For  $\mathbf{B}$  oriented along the cube axis,  $\mathbf{B} \parallel \langle 100 \rangle$ , four dominant Zeeman components are observed. In addition, weaker Zeeman components originating from a relatively broad shoulder line partly superimposed on  $L_4^1$  are seen. For  $\mathbf{B}$  along  $\langle 011 \rangle$  up to 12 Zeeman components are seen at 5 T. The overall splitting is

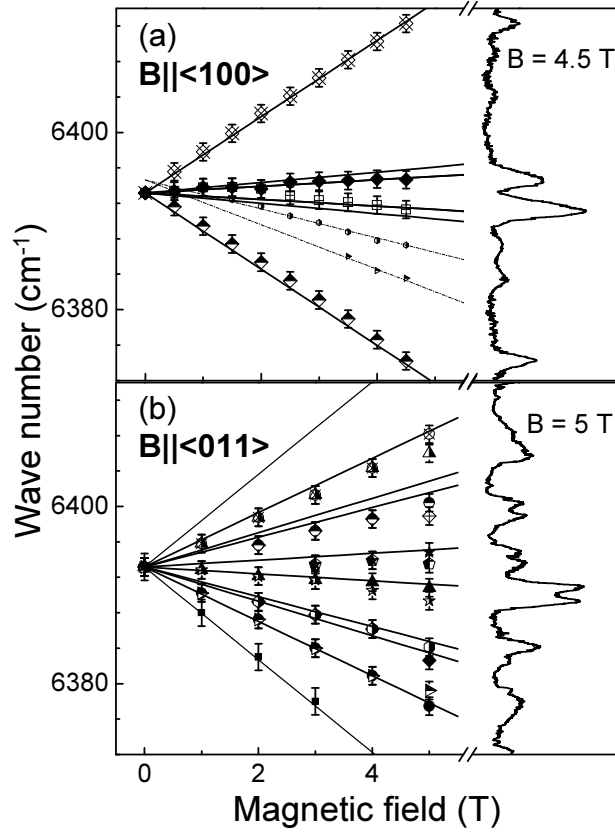


Figure 6.6: Zeeman effect of the line  $L_4^1$ , with the magnetic field along the main crystal directions (a)  $\mathbf{B} \parallel \langle 100 \rangle$ , and (b)  $\mathbf{B} \parallel \langle 011 \rangle$ , at  $T = 4.2$  K.

about an order of magnitude larger than that for  $L_1^1$  [95]. The effective  $g$ -factors for the outer Zeeman components are about 20 for both magnetic field orientations. We conclude that, unlike in the case of  $L_1^1$ , here we observe transitions not only with the difference,  $(G - g)$ , but also with the sum,  $(G + g)$ , of the effective  $g$ -factors of the excited and ground states.

By simulating the line positions with Hamiltonian 6.8 we can determine both the  $g$ -tensor values for the ground state,  $\mathbf{g}^{(4)} = [8.3 \pm 0.5, 7.6 \pm 0.5, 1.6 \pm 0.3]$ , and the excited state,  $\mathbf{G}^{(1)} = [0 \pm 0.1, 14.8 \pm 0.5, 0 \pm 0.1]$ . As can be seen from the solid lines in Fig. 6.6, the simulation gives in this case good agreement with the experimental data for all  $(G - g)$  and  $(G + g)$  transitions and all nonequivalent orientations in  $C_{2v}$  symmetry. Due to the fact that  $G_z = 0$ , i.e., there is no Zeeman splitting in the excited state at  $\mathbf{B} \parallel \langle 100 \rangle$  for the defect configuration with  $\mathbf{B}$  parallel to  $z$ , the  $(G - g)$  and  $(G + g)$  transitions coincide reducing the number of Zeeman components from four to two. For other defect configuration the energies are very close to those of the  $(G - g)$  transitions, with the energy difference falling within

the linewidth (indicated by error bars in Fig. 6.6). In contrast, the lines with the sum ( $G + g$ ) of the effective  $g$ -values can be seen. Hence, for  $\mathbf{B} \parallel \langle 100 \rangle$  only four separated PL lines are observed.

Similarly, since  $G_x = 0$ , for  $\mathbf{B} \parallel \langle 011 \rangle$  ten out of twelve possible components are expected, with one being too weak to be detected. At high fields additional splitting for two configurations appears which indicates some misorientation of the rotation plane. The calculated line positions agree very well with the experimental ones within the whole magnetic field range studied only for the lower energy Zeeman components. The peak energies for the higher energy Zeeman components depend nonlinearly on  $B$  at higher fields, due to interaction with the second, close lying excited state.

The determined  $G_y$  tensor value for the excited state agrees within the experimental error with the value estimated in Ref. [95] from Zeeman splitting of  $L_1^1$ , but it is more accurate. We can now use this value to give the accurate tensor values for the ground state involved in  $L_1^1$   $\mathbf{g}^{(1)} = [0 \pm 0.1, 18.1 \pm 0.5, 0 \pm 0.1]$

#### 6.4.4 Splitting of line $L_1^2$ (the hot line)

The splitting of the hot line, labelled  $L_1^2$  in Table 6.2, in magnetic fields up to 5.25 T at 55 K is shown in Fig. 6.7. Five components are observed for  $\mathbf{B} \parallel \langle 011 \rangle$  and four components are seen for  $\mathbf{B} \parallel \langle 100 \rangle$ . The pattern of the Zeeman splitting is very similar to that of line  $L_1^1$  stemming from transitions between two doublets of ground and excited state. For line  $L_1^1$  three components were seen with the field oriented along  $\langle 100 \rangle$  due to the fact that the  $g_z$  tensor values vanished for both the ground and the excited state, whereas the excited state involved in  $L_1^2$  has nonzero  $g_z$  value. The absolute magnitude of the splitting is also comparable. Moreover, just like in the case of line  $L_1^1$ , only transitions with a difference of the effective  $g$ -factors can be observed.

The splitting of line  $L_1^2$  can be very well described with the following  $g$ -tensor for the second excited state:  $|\mathbf{G}^{(2)}| = [0 \pm 0.1, 11.2 \pm 0.5, 2.0 \pm 0.2]$  (the  $g$ -tensor of the ground state being the same as for  $L_1^1$ ). The simulation of line positions by Eq. 6.8 with these parameters is shown by solid lines in Fig. 6.7. The deviation from linear dependence observed for lower energy Zeeman components is due to the fact that at high magnetic fields the magnitudes of the Zeeman and the crystal field interactions become comparable, resulting in mixing between sublevels in the  $J = 15/2$  manifolds. The higher energy Zeeman components corresponding to transitions from the lower lying level of the excited state doublet to the lower lying level of the ground state doublet are less affected.

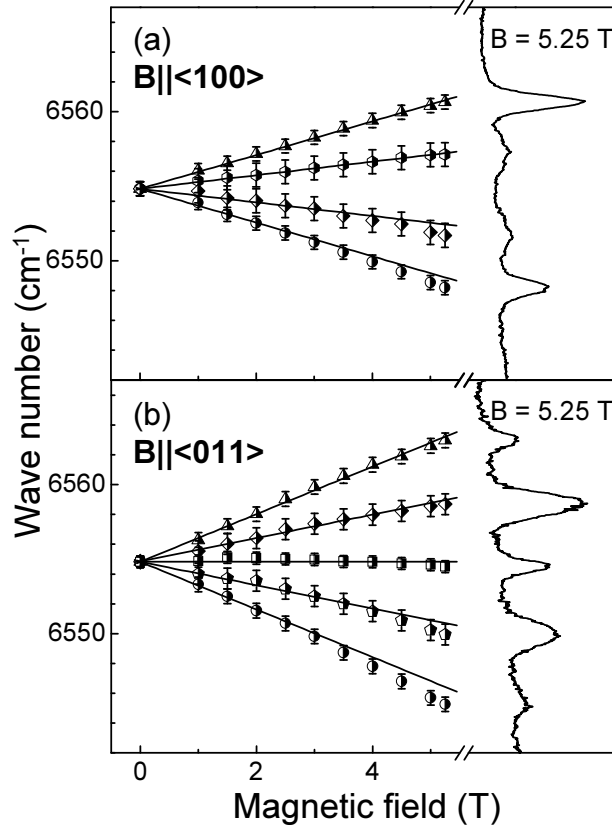


Figure 6.7: Zeeman effect of the line  $L_1^2$  (hot line of line  $L_1^1$ ) with the magnetic field along the main crystal directions (a)  $\mathbf{B} \parallel \langle 100 \rangle$ , and (b)  $\mathbf{B} \parallel \langle 011 \rangle$ , at  $T = 55$  K.

### 6.4.5 Splitting of other spectral components

The Zeeman effect was also investigated for the  $L_2^1$  and  $L_3^1$  PL lines. The experimental peak positions versus magnetic field are shown in Fig. 6.8 for the  $\mathbf{B} \parallel \langle 100 \rangle$  and  $\mathbf{B} \parallel \langle 011 \rangle$  field directions. The Zeeman splitting pattern suggests that we deal in this case with transitions from the excited doublet state to a  $\Gamma_8$  quadruplet split by a lower symmetry crystal field. We can speculate that if the low symmetry distortion is small, the selection rules valid for  $T_d$  symmetry may approximately hold at high magnetic fields, when the states could regain their initial “cubic” character. In other words, any extra Zeeman component in the PL to those determined by Table 6.3 will have lower intensity. Based on that, we can predict the number of “strong” Zeeman components observed in the PL for a center with small  $C_{2v}$  distortion. For  $\mathbf{B} \parallel \langle 100 \rangle$  we should see two nonequivalent defect configurations, one with  $\mathbf{B} \parallel z$  and one with  $\mathbf{B}$  in the plane perpendicular to  $z$ . We should, hence,

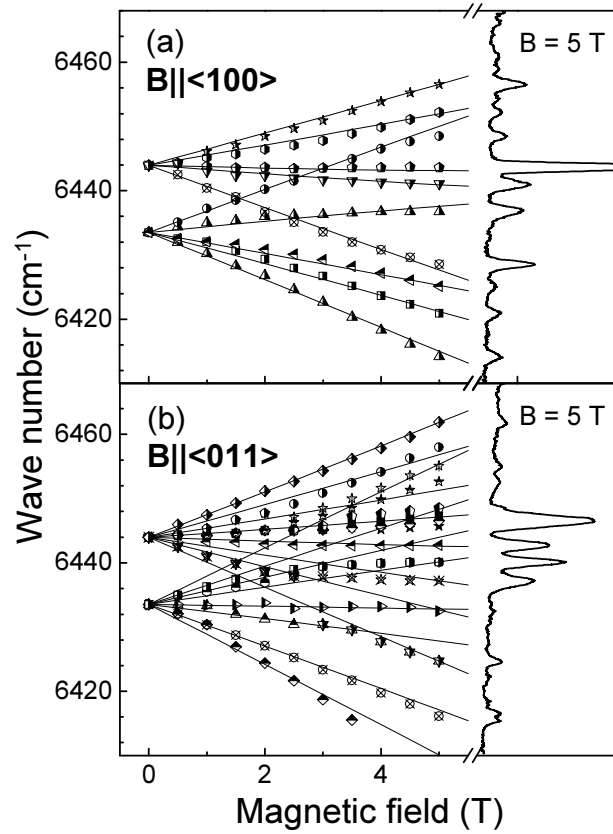


Figure 6.8: Zeeman effect of the line  $L_2^1$  and line  $L_3^1$ , with the magnetic field along the main crystal directions (a)  $\mathbf{B} \parallel \langle 100 \rangle$ , and (b)  $\mathbf{B} \parallel \langle 011 \rangle$ , at  $T = 4.2$  K.

see six components for the latter but only four components for the former, as there is no splitting of the excited state in this configuration ( $G_z^{(1)} = 0$ ). Similarly, for  $\mathbf{B} \parallel \langle 011 \rangle$ , with three nonequivalent defect configurations, we should see  $6+6+4=16$  components. As illustrated by Fig. 6.8, this is exactly what we observed in the experiment.

The solid lines in the Fig. 6.8 are guide for eye only. In order to determine the parameters reliably, additional experiments are necessary, either at low magnetic fields - when the Zeeman interaction is much weaker than the crystal field splitting and doublets can be treated separately, or in the opposite regime - when the Zeeman splitting is much larger than the crystal field splitting.

We have also measured a magnetic field induced splitting of line  $L_5^1$  for  $\mathbf{B} \parallel \langle 001 \rangle$ . The splitting pattern is very similar to that observed for  $L_4^1$ , i.e., the dominant transitions are those with a sum and difference of the effective  $g$ -factors for the two coinciding configurations. Due to the low PL intensity, it was not possible to measure the splitting for  $\mathbf{B} \parallel \langle 011 \rangle$ ; hence the  $g$ -tensor values could not be

Table 6.4:  $g$ -tensor values used for the calculated splitting.

line label	initial state			$G_{av}$	final state			$g_{av}$
$L_1^1$	0	14.8	0	$5.0 \pm 0.5$	0	18.1	0	$6.1 \pm 0.5$
$L_1^2$	0	11.2	2	$4.4 \pm 0.5$	0	18.1	0	$6.1 \pm 0.5$
$L_4^1$	0	14.8	0	$5.0 \pm 0.5$	8.3	7.6	1.6	$5.8 \pm 0.5$

determined. All determined  $g$ -tensor values are listed in Table 6.4.

## 6.5 Discussion

### 6.5.1 Symmetry considerations

On the basis of the experimental data reported here, the following picture can be proposed. The PL spectrum observed in SMBE grown samples is characterized by a small number of very narrow lines. Although sharp emission bands should be expected for Er in view of the very long radiative lifetime of its excited  $^4I_{13/2}$  state ( $\sim$  ms), linewidths of several meV are routinely observed for Er-related optical centers in crystalline silicon. Therefore it appeared that in the present case emission bands are characterized by the truly homogeneous linewidth. This has indeed been confirmed by, and formed a necessary prerogative for, the (first ever for Er in Si) successful observation of the Zeeman effect, as reported in the current study. From analysis of the Zeeman effect we conclude that all the major lines of the observed PL spectrum originate from the same center, the Er-1. Such a conclusion is also consistent with the thermally-induced changes of the PL spectrum, with all the major features - lines  $L_1^1$  to  $L_4^1$  - developing hot lines with identical energy spacings, indicating the common excited state for their origin. In this way the current study unambiguously shows that a preferential formation of one specific type of Er-related optically active center is realized in annealed SMBE-grown multilayer structures.

From the analysis of the angular dependence of the magnetic field induced splitting of PL lines, the  $C_{2v}$  symmetry of the Er-1 center has been established, and individual  $g$ -tensors for several crystal field split levels within ground and excited state multiplets have been determined. These are summarized in Table 6.4.

Although the lower-than-cubic symmetry of the Er-1 center is concluded from experiment, the distortion from cubic symmetry appears to be small. This is evident from the fact that optical transitions follow the selection rules for  $T_d$  sym-

metry rather than those for transitions between  $\Gamma_5$  states of  $C_{2v}$  symmetry, where all the transitions would have equal probability. We could speculate that the observed orthorhombic- $I$  symmetry could arise from a distortion of an tetrahedrally coordinated  $\text{Er}^{3+}$  ion.

If only a small distortion of cubic symmetry is present, the average  $g_{\text{av}}$  factor can be related to the isotropic cubic  $g_c$  factor by [84]:

$$g_{\text{av}} = g_c = \frac{1}{3}(g_x + g_y + g_z). \quad (6.11)$$

In the case of line  $L_1^1$  the average  $g_{\text{av}}$  value for the lowest level of the ground state is  $6.1 \pm 0.5$ , slightly smaller than 6.8 the value characteristic for pure  $\Gamma_6$ , and similar to values found for Er in different host materials [77,84,85,102,103,104]. Therefore the Er-1 center ground state is likely to be of the  $\Gamma_6$  character. The  $g_{\text{av}}$  values of the initial and final states determined from all the investigated transitions are also shown in the Table 6.4.

For the lowest level of the first excited state, the  $g_{\text{av}}$ -value is determined as  $4.9 \pm 0.5$ . It is similar to the (isotropic)  $g$ -factor of the  $\Gamma_7$  states of a pure  ${}^4I_{13/2}$  manifold of 5.54. As can be seen from Table 6.3, this indicates that for line  $L_1^1$  we deal mostly with electric-dipole type transitions, without spin flips. This is to be expected for Er, since the strong spin-orbit coupling, characteristic for rare-earth ions, leads to the admixture of different excited configurations. The  $g$ -values determined here are smaller than these found in more ionic hosts. This can be due to covalent effects, as the results of the Landé factor becomes smaller because of stronger quenching of the orbital momentum. The Zeeman splittings of lines  $L_2^1$  and  $L_3^1$  behave like a transition from a doublet to a distorted  $\Gamma_8$  quadruplet. The splitting of line  $L_4^1$  indicates a doublet to doublet transition. However in that case we can see PL lines corresponding to the sum and the difference of the  $g$ -tensors of the ground and the excited states. Also the hot line  $L_1^2$  appears to arise due to a transition from a doublet, but of a different symmetry. This could be a  $\Gamma_6$  doublet. However, in such case, in addition to transitions corresponding to difference of effective  $g$ -tensors, also PL lines described by the sum of these parameters should be present. This is not observed in the experiment. Another possibility would be that the hot line originates from a doublet split off from the quadruplet due to the lower symmetry component, a situation similar to that in the ground state, as concluded from analysis of lines  $L_2^1$  and  $L_3^1$ .

### 6.5.2 Consequences for the microscopic model of the Er-1 center

Although the microscopic symmetry of the Er-1 center is determined to be orthorhombic  $-I$  ( $C_{2v}$ ), we have seen that lines  $L_2^1$  and  $L_3^1$  can be interpreted as arising from a split quadruplet. This could indicate that orthorhombic- $I$  distortion of the  $T_d$  crystal field is small. It is also consistent with the fact that transition probabilities follow rules of cubic symmetry. Assuming this situation to be true, we can try to place the Er-1 center on the LLW diagram given in Fig. 6.4. Inspection of this figure shows that the ground state is either  $\Gamma_7$ , for  $-1 \leq x \leq -0.46$ , or  $\Gamma_6$ , for  $-0.46 \leq x \leq 0.58$  with  $W$  positive. On the other hand, the lowest level of the excited state is a doublet of either  $\Gamma_6^{(1)}$ , for  $-0.57 \leq x \leq 0.65$ , or  $\Gamma_7$  symmetry, for  $0.65 \leq x \leq 1$ . Now, taking into account splitting of PL lines at low temperature and assuming that lines  $L_2^1$ ,  $L_3^1$  arise from a split quadruplet, the best fit to the experimental data was obtained for three  $x$  values:  $-0.55$ ,  $-0.07$ , and  $0.41$ , resulting in  $W$  values of  $2.046 \text{ cm}^{-1}$ ,  $0.476 \text{ cm}^{-1}$ , and  $0.739 \text{ cm}^{-1}$ , respectively. As can be seen from Fig. 6.4b, the corresponding sequence of the ground state levels would be  $\Gamma_7$ ,  $\Gamma_8$ ,  $\Gamma_6$ ,  $2\Gamma_8$ ;  $\Gamma_6$ ,  $\Gamma_8$ ,  $\Gamma_7$ ,  $2\Gamma_8$ ; and  $\Gamma_6$ ,  $\Gamma_8$ ,  $\Gamma_8$ ,  $\Gamma_7$ ,  $\Gamma_8$ , respectively. Taking into account the symmetry information obtained from the magnetic field induced splitting of PL lines  $L_1^1$ ,  $L_2^1$ ,  $L_3^1$ ,  $L_4^1$  and  $L_1^2$ , the situation with  $x = 0.41$  and  $W = 0.739 \text{ cm}^{-1}$  for  $J = 15/2$  emerges as the most plausible one. The  $x$  value is positive as expected for a tetrahedral interstitial position. It is very close to that for the cubic center observed in implanted Si [76, 77]. The  $x$ -value of the  $J = 15/2$  state obtained in this study differs, however, from that of the tetrahedral interstitial Er center observed in implanted Si,  $x = 0.35$  [76, 77]. The discrepancy may be due to the fact that we deal with low-temperature grown silicon, which might have slightly different properties from the Czochralski grown material typically used for implantation. On the other hand, it should be stressed that our analysis bases on the assumption that the  $C_{2v}$ -symmetry crystal field can be treated as a small distortion of cubic symmetry, which need not be the case. In fact, the strong anisotropy of the  $g$ -tensors indicates rather that the cubic and orthorhombic crystal field potentials may be comparable.

For a cubic symmetry center,  $x$  and  $W$  values of the  $J = 13/2$  state can be determined from these of the  $J = 15/2$ . In the present case, we should also take into account the Zeeman splitting of the hot line. While this is consistent with a doublet-to-doublet transition, no transitions due to sum of the relevant effective  $g$ -tensor values are observed. This indicates the upper state to be arising from a splitting of the quadruplet (in analogy the ground state splitting responsible for lines  $L_2^1$  and  $L_3^1$ ) rather than a  $\Gamma_7$  doublet. The possible position of  $J = 13/2$

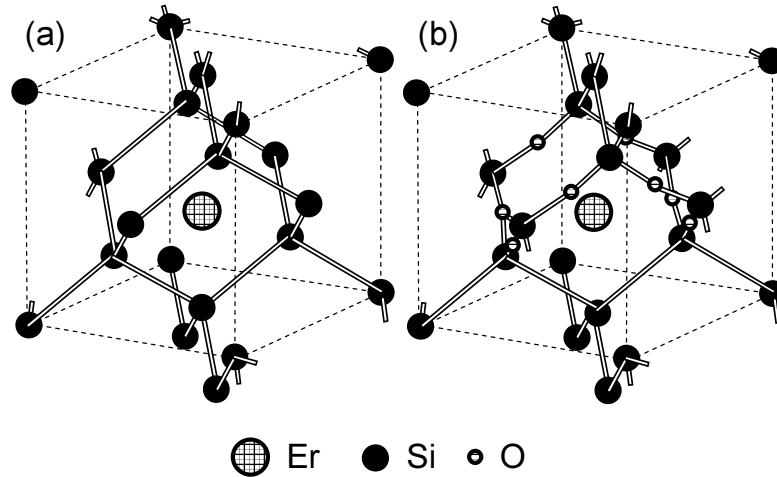


Figure 6.9: *The possible microscopic structure of the Er-1 center: (a) tetrahedral interstitial  $\text{Er}^{3+}$  ion with the  $C_{2v}$  symmetry obtained by a small distortion along the  $\langle 100 \rangle$  direction; (b) tetrahedral interstitial  $\text{Er}^{3+}$  ion - oxygen cluster. The  $C_{2v}$  symmetry lowering can be obtained by lattice distortion or by details of oxygen incorporation.*

multiplet of the Er-1 center on the LLW diagram is also indicated in the Fig. 6.4.

Finally, we would like to comment on the possible microscopic model of the Er-1 center. This issue is of fundamental importance, as the Er-1 center takes a prominent position of the only Er-related optically active center which can be preferentially generated in crystalline Si. Since the observed splitting is consistent with that which can be expected for an isolated  $\text{Er}^{3+}$  ion, we can assume that only one Er ion is involved in the structure of Er-1. Also preferential formation of a single configuration is easier to envisage for a center containing one rather than multiple Er ions. The estimated  $x$  value of the ground state is positive as expected for a tetrahedral interstitial. This site was predicted from total energy calculations as the most stable configuration of  $\text{Er}^{3+}$  ion in the crystalline silicon host [86]. Also, channeling studies identified a  $T_d$  interstitial site as the preferred location of  $\text{Er}^{3+}$  ions implanted into Si [74]. Taking into account all the available information, we propose to identify the Er-1 center with an  $\text{Er}^{3+}$  ion occupying a slightly distorted  $T_d$  interstitial site - see Fig. 6.9a.

From analysis of the Zeeman effect we were able to determine the orthorhombic- $I$  symmetry of the Er-1 center. The origin of the  $C_{2v}$  symmetry distortion is not clear, yet. This relatively high symmetry type is easily realized for defects in crystalline silicon by lifting equivalence of two mutually perpendicular  $\{011\}$  mirror

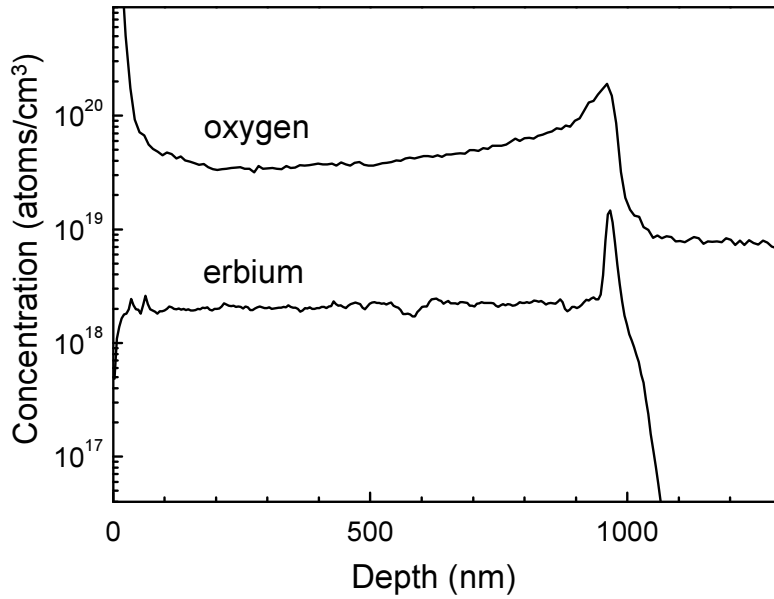


Figure 6.10: *Profile of oxygen and erbium concentrations measured by SIMS for Sample #51.*

planes. Among other possibilities, it can be achieved by a minor distortion of a  $T_d$  site along a  $\langle 100 \rangle$  direction, or by a symmetric (with respect to the  $\langle 100 \rangle$  axis) incorporation of impurities in one of the planes (- see, e.g., microscopic models of negatively charged vacancy center [105], substitutional transition metal atoms [83], thermal donor [106]).

Unfortunately, in contrast to EPR or electron-nuclear double resonance (ENDOR) measurements, no insights on chemical identity or lattice location of ligand atoms can be derived from the present study. We therefore have to rely on the information gathered so far on optical activity of Er in Si. The most prominent conclusion here is that oxygen (as well as other electronegative elements) enhance emission of Si:Er, the effect being optimal for oxygen-to-erbium doping ratio of approximately 10:1. Also EXAFS investigations [73] revealed the presence of six oxygen atoms in the direct surrounding of optically active Er in Czochralski-grown Si. These findings are consistent with results obtained in this study: while no oxygen was intentionally introduced during the SMBE growth process of the multi-layer structures used for Zeeman measurements, secondary ion mass spectroscopy (SIMS) analysis shows a clear increase of O concentration ( $[O] = 1.5 \div 4 \times 10^{19} \text{ cm}^{-3}$ ) in the structure when compared to the substrate, – see Fig. 6.10 [107]. Therefore, based on published reports and on the structural information available for the samples used in this project, we propose that the Er-1 center comprises

at least 8 oxygen atoms in the direct surrounding of a single Er atom at a high symmetry site. A possible atomic model of such a center is depicted in Fig. 6.9b. In this case oxygen atoms have been placed at the usual puckered bonded positions releasing strain on the 4 Si nearest neighbors of the Er. While formation of such a large oxygen complex of specific symmetry might appear not likely at the first glance, we point out that the orthorhombic- $I$  ( $C_{2v}$ ) symmetry is characteristic for silicon thermal donors formed by oxygen aggregation [108]. Note that the sample growth temperature allows thermal donor formation and Er could enhance oxygen aggregation. On the other hand, the Er-1 center is formed during annealing at 800 °C, at which temperature the thermal donors are found to convert into electrically nonactive aggregates [109]. Unfortunately, owing to the particular  $g$ -tensor of the ground state, no EPR or ENDOR measurements are possible for the Er-1 center, and no insight into the chemical identity or lattice location of ligand atoms can be derived by these technique. Therefore the issue of oxygen incorporation in the microstructure of the Er-1 center cannot be concluded at this stage, and will require further investigations.

## 6.6 Summary and conclusions

We present results of a magneto-optical study of multilayer Si/Si:Er structures grown by SMBE technique. We show that the presence of Si spacer regions considerably increases emission intensity when compared to single layers. The PL from annealed multilayer structures is dominated by emission from the particular center, the Er-1 center, which is then preferentially formed. The PL spectrum of this center is characterized by ultra narrow homogeneous lines. Based on analysis of the magnetic field induced, angular dependent splitting of the PL lines, we identify the orthorhombic- $I$  symmetry of the Er-1 center and give  $g$ -tensors for several lower-lying levels of the  $^4I_{15/2}$  ground and the lowest excited  $^4I_{13/2}$  state multiplets. In particular, we identify the original  $\Gamma_6$  and  $\Gamma_7$  characters for the lowest crystal-field split levels of the ground and the excited states, respectively. Based on this analysis, we propose that the microscopic structure of the Er-1 center comprises a single  $\text{Er}^{3+}$  ion at a distorted interstitial  $T_d$  site with multiple oxygen atoms in its direct vicinity.

# Chapter 7

## Optical Properties of the Er-1 Center: A Candidate for Realization of Optical Gain in Si:Er

*In Chapters 5 and 6 we have investigated microscopic structure of the Er-1 center formed in Si/Si:Er nanolayers grown by a modified SMBE technique. In this Chapter we examine specific optical properties of this center in order to evaluate its potential for photonic applications. In particular, we determine its effective excitation cross section and estimate the percentage of Er dopants involved in formation of Er-1.*

### 7.1 Introduction

While crystalline silicon continues to dominate the mainstream integrated circuit device manufacturing, applications of this most important semiconductor material remain electronic rather than photonic. Due to the relatively small and indirect bandgap, silicon is a poor light emitter. Although various approaches to silicon photonics, such as quantum confinement in nanostructures [71] and inhomogeneous Si-based media [110], or optical doping with rare-earth ions [70, 111], have been actively explored, lasing action still has not been demonstrated, and reports on optical gain [112] and intense room temperature emission [113] from Si structures remain controversial. In Chapters 5 and 6, we have confirmed preferential production of a single type of an optically active Er-related center in silicon [95, 114, 115]. High concentration of a specific center (labeled Er-1) was found in Er-doped Si

nanolayers grown by sublimation MBE. We have also established the ultra-small linewidth characteristic of emission related to the Er-1 center which indicates a possibility of a  $10^3 - 10^4$  increase of the expected gain coefficient, when compared to the implanted Si:Er materials used so far. Therefore the Er-1 center emerges as a plausible candidate for achieving population inversion and stimulated emission in Si based materials: a long sought after goal of semiconductor science and technology.

The research on optical properties of silicon continues to be spurred by prospects of a full integration of electronic and photonic components (also on-chip) and by almost unlimited possibilities of the highly developed silicon technology. While an efficient band-to-band recombination is not possible, crystalline silicon shows some typical features of optical materials, such as afterglow and optical memory [116,117], and has properties that are potentially very attractive for optical applications. The most prominent of these is the possibility to suppress nonradiative recombinations, offered by a superior level of impurity control.

Quantum confinement effect can influence the energy band structure. In deed, following this approach optical gain in nanocrystalline silicon [112] and efficient room-temperature (RT) emission from boron inclusions were reported [113]. An alternative approach to improve the photonic properties of silicon is offered by optical doping, i.e. by introduction of efficient radiative recombination centers. Rare-earth ions are especially suited for optical doping as their (core) structure is well screened from external influence. Erbium has become the optical dopant of choice, in view of the fact that its emission wavelength of  $\sim 1.5 \mu\text{m}$  is suitable for telecommunication applications.

In the past decade Si:Er has been intensively investigated for emission optimization [72]. The research revealed several disadvantages of this system, which could not be fully eliminated: a strong emission reduction at higher temperatures, and a low percentage of optically active Er-related centers. Thermal quenching is absent for photoluminescence (PL) of Er ions embedded in a  $\text{SiO}_2$  matrix, but this system, in turn, is characterized by a very small cross section of (direct) excitation. In view of that, a nonhomogenous medium of Si nanocrystals (nc-Si) dispersed in a  $\text{SiO}_2$  matrix is recently investigated as an alternative host for Er doping. In this case, the large bandgap of  $\text{SiO}_2$  provides thermal stability for the Er emission, while Si nanocrystals facilitate efficient excitation. Following this approach, development of RT-operating LED's was proven to be possible. However, recent results indicate that population inversion might be difficult to reach in this system [118, 119].

In view of a low optical activity of Er ions in Si, a high concentration in range of  $10^{19} - 10^{20} \text{ cm}^{-3}$  is necessary. Such high impurity levels exceed by far the

solubility limits, and can only be realized by nonequilibrium methods. For that purpose implantation [71, 70] and MBE [120] are commonly used. The currently obtained quantum efficiencies of RT photo- and electroluminescence from Si:Er are rather low – typically  $10^{-5} - 10^{-4}$ .

Finally, we note that although the Si:Er system exhibits a long excited state lifetime, due to the forbidden character of the intra- $4f$ -electron shell transitions, population inversion and laser action have not been achieved in crystalline Si:Er (while optical amplifiers based on Er-doped insulators are routinely manufactured). Realization of lasing action would provide a major boost for optoelectronic applications of Si. In order to achieve gain, the absorption by  $\text{Er}^{3+}$  ions should be maximized and losses minimized. The latter include absorption of the  $1.5 \mu\text{m}$  radiation in the host and nonradiative recombinations of excited  $\text{Er}^{3+}$  ions. For reliable gain estimation, the value of the absorption cross section  $\sigma$  at  $1.5 \mu\text{m}$  for  $\text{Er}^{3+}$  ions embedded in Si substrate is necessary. This is not known and has to be derived from the linewidth  $\Delta E$  and decay time  $\tau$  of the  $1.5 \mu\text{m}$  Er-related emission band. For the presently used implanted Si:Er materials these are typically  $\Delta E \approx 5 \text{ meV}$  and  $\tau \approx 1 \text{ ms}$ . Using these values and assuming that the  $\tau \approx 1 \text{ ms}$  time constant represents the purely radiative lifetime, the  $\text{Er}^{3+}$  ion excitation cross section can be estimated as  $\sigma \approx 2.5 \times 10^{-19} \text{ cm}^2$ . In order to calculate the gain  $\alpha$  the excitation cross section has to be multiplied by the available concentration of excited  $\text{Er}^{3+}$  ions:

$$\alpha_{\lambda \approx 1.5 \mu\text{m}} = \sigma_{\lambda \approx 1.5 \mu\text{m}} N(\text{Er}^{3+}). \quad (7.1)$$

Assuming a typical concentration of  $\text{Er}^{3+}$  ions in the implanted layer to be  $N(\text{Er}^{3+}) \approx 10^{20} \text{ cm}^{-3}$  and taking into account that usually only 1% of them is optically active, we obtain the gain coefficient of  $\alpha \approx 0.25 \text{ cm}^{-1}$ . On the other hand, losses due to free-carrier absorption at  $1.5 \mu\text{m}$ , non-radiative recombination of  $\text{Er}^{3+}$  ions (Auger effect, upconversion, etc.), are usually estimated as at least  $1 \text{ cm}^{-1}$ . Therefore realization of a Si laser based on Er doping is usually considered unlikely.

Recently a new type of Si:Er optical structures has been proposed [79]. The idea follows from a notion that since the most efficient low temperature excitation mechanism of Er proceeds via excitons, the generation conditions for excitons should be optimized. The requirements of a high  $\text{Er}^{3+}$  ions concentration and efficient exciton generation cannot be met simultaneously. Therefore for heavily Er-doped layers excitons are generated in the substrate rather than in the layer itself. This is evidenced by the fact that PL intensity does not increase above certain thickness of a Si:Er layer. It does increase, however, when a “spacer” of undoped Si is inserted into the Si:Er layer. Therefore, a sandwich structure of interchanged Si/Si:Er nanolayers exhibits superior optical properties. Upon illumination with

a laser beam, excitons generated in spacer regions diffuse into doped layers and provide excitation of  $\text{Er}^{3+}$  ions. Such an “spatially-separated” excitation scheme is in its concept somewhat similar to that utilized in the earlier mentioned inhomogeneous  $\text{SiO}_2/\text{nc-Si:Er}$  samples, where processes of photon absorption (nc-Si) and emission ( $\text{Er}^{3+}$  ions in the  $\text{SiO}_2$  matrix) also take place in different parts of the sample. In addition to the more efficient exciton formation, spatial separation reduces Auger quenching by free carriers generated during the excitation process.

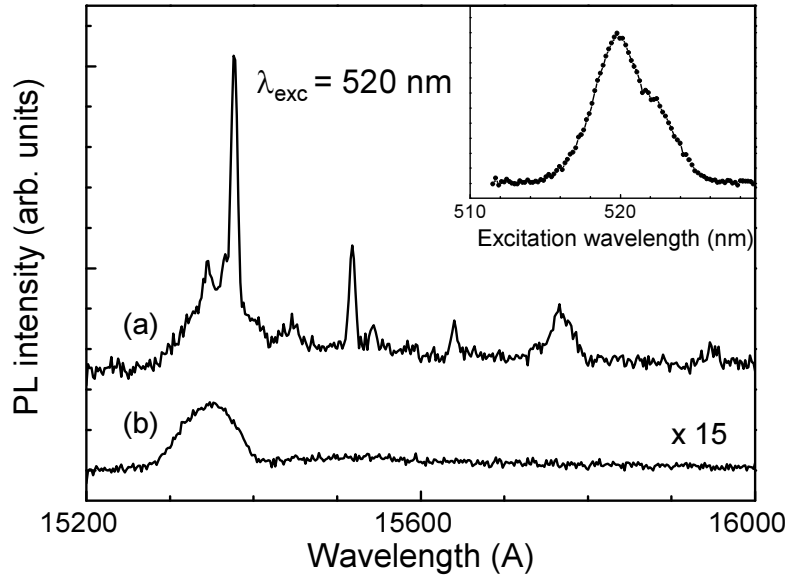


Figure 7.1: *PL spectra measured at 4.2 K for (a) sample of Si:Er and (b)  $\text{SiO}_2\text{:Er}$  under excitation wavelength  $\lambda_{\text{exc}}=520$  nm. The inset shows a PLE spectrum  $\text{SiO}_2\text{:Er}$  sample – see text for details.*

In Chapters 5 and 6, we have conclusively showed that Er-related  $1.5 \mu\text{m}$  emission in such structures is dominated by a single center, the Er-1 center, which is characterized by a homogeneous and ultranarrow bandwidth of  $\Delta E < 10 \mu\text{eV}$ . In this Chapter we investigate potential of the multilayer structures for realization of optical amplification. To this end, we attempt to measure excitation cross section and percentage of Er dopants participating in the optically active centers.

## 7.2 Experimental details

The experiments were performed on two samples: Er-doped silicon grown by sublimation MBE (Si:Er - #51) and Er-doped silica ( $\text{SiO}_2\text{:Er}$ ). The sample #51 has

been investigated in Chapter 6 and comprises 400 interchanged Si and Si:Er layers of a few nanometers thickness stacked along the  $\langle 100 \rangle$  growth direction. The total Er density is found to be  $2 \times 10^{14} \text{ cm}^{-2}$ . The SiO<sub>2</sub>:Er sample has been prepared by a triple Er-implantation:  $1.5 \times 10^{14} \text{ cm}^{-2}$  at 200 keV;  $2.8 \times 10^{14} \text{ cm}^{-2}$  at 500 keV and  $5.6 \times 10^{14} \text{ cm}^{-2}$  at 1000 keV and followed by 30 min. at 1000 °C annealing in nitrogen. The total Er implantation dose was then  $9.9 \times 10^{14} \text{ cm}^{-2}$ . For comparison, data obtained for an implanted sample (labeled J900) have been also included in the study. This sample has been prepared by Er (energy 320 keV, dose  $3 \times 10^{12} \text{ cm}^{-2}$ ) and O (energy 40 keV, dose  $3 \times 10^{13} \text{ cm}^{-2}$ ) implantations followed by 900 °C/30 min. anneal in nitrogen.

The PL experiments were carried out in a variable temperature continuous-flow cryostat accessing the 1.5 – 300 K range (Oxford Instruments Optistat CF). The samples were excited using a cw argon-ion laser operating at 514.5 nm or a tunable Optical Parametric Oscillator (OPO) laser, producing pulses of 5 ns duration at 20 Hz repetition rate. The luminescence was resolved with a 1 m F/8 monochromator (Jobin-Yvon THR-1000) equipped with a 900 grooves/mm grating blazed at 1.5  $\mu\text{m}$  and detected by an infrared photomultiplier with a 35  $\mu\text{s}$  response time. Figure 7.1 shows the PL spectra of the Si:Er (#51) and SiO<sub>2</sub>:Er samples in the 1.5  $\mu\text{m}$  range at 4.2 K under excitation with OPO set to a wavelength of  $\lambda_{exc} = 520 \text{ nm}$ . In this excitation wavelength, the SiO<sub>2</sub>:Er sample was excited resonantly corresponding to the  ${}^4I_{15/2} \rightarrow {}^2H_{11/2}$  transition. The inset shows a photoluminescence excitation (PLE) measurement for SiO<sub>2</sub>:Er sample obtained by scanning the OPO wavelength.

### 7.3 Results and discussion

For determination of the excitation cross section, the excitation power dependence of the PL intensity was measured at 4.2 K - see Fig. 7.2, for all four major components of Er-1 center: line  $L_1^1$  ( $6502.85 \text{ cm}^{-1}$ ) - trace a;  $L_2^1$  ( $6443.72 \text{ cm}^{-1}$ ) - trace b;  $L_2^1$  ( $6433.59 \text{ cm}^{-1}$ ) - trace c and  $L_2^1$  ( $6393.17 \text{ cm}^{-1}$ ) - trace d, under cw argon-ion laser excitation – see Chapter 6 for line labelling. All the measurements were performed with the same experimental settings, so that the PL intensity scale is common for all the data points. As can be seen, the behavior of these lines is similar. Results were fitted by a formula [72] [121]:

$$I_{PL} = \frac{A\sigma\tau\Phi}{1 + \beta\sqrt{\sigma\tau\Phi} + \sigma\tau\Phi}, \quad (7.2)$$

where  $\beta$  is an adjustable parameter representing the physical elements of the luminescence process,  $\sigma$  is a effective excitation cross section of Er<sup>3+</sup> ion,  $\tau$  is the

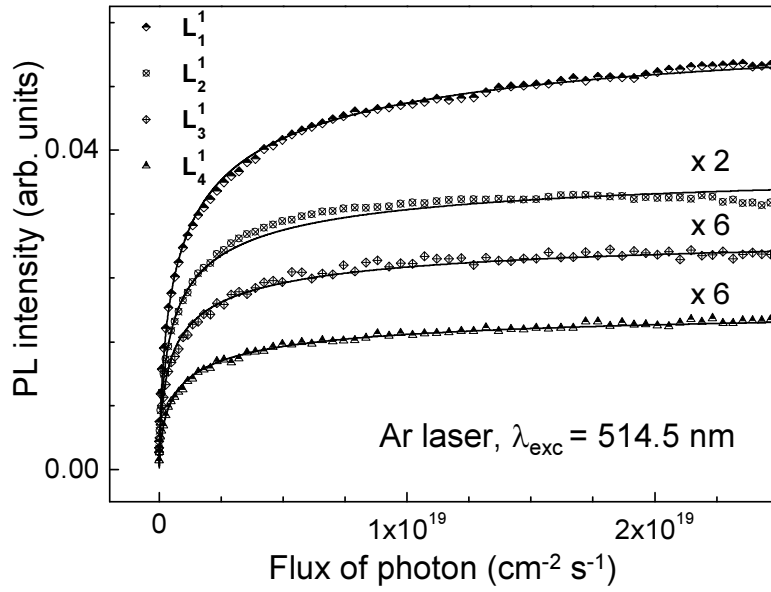


Figure 7.2: *PL intensity, measured at 4.2 K, as a function of excitation power of cw laser for line  $L_1^1$ ,  $L_2^1$ ,  $L_3^1$ , and  $L_4^1$*

effective lifetime of erbium in the excited state and  $\Phi$  is the flux of photons. The appearance of the  $\beta\sqrt{\sigma\tau\Phi}$  term is a fingerprint of the Auger effect hindering the luminescent process [72] [121]. The solid curves are best fits to the experimental data using Eq. 7.2 with parameter  $\beta = 1.9 \pm 0.1$ . In that way, the excitation cross section parameters of Er-1 center are determined as:  $\sigma(\lambda_{exc} = 514.5 \text{ nm}) = 4.9 \times 10^{-15}$ ,  $5.7 \times 10^{-15}$ ,  $8.5 \times 10^{-15}$  and  $5.9 \times 10^{-15} \text{ cm}^2$  for line  $L_1^1$ ,  $L_2^1$ ,  $L_3^1$  and  $L_4^1$ , respectively. With the experimental error of  $\Delta\sigma = \pm 2 \times 10^{-15} \text{ cm}^2$ , the excitation cross sections are identical for all the emission lines. This is consistent with the results of Chapter 6 where we have showed that these lines originate from the same Er-related center.

We have also examined decay characteristics of the  $L_1^1$ ,  $L_2^1$  and  $L_3^1$  lines at 4.2 K under OPO excitation with a wavelength of  $\lambda_{exc} = 520 \text{ nm}$  and  $\Phi = 3 \times 10^{22} \text{ cm}^{-2}\text{s}^{-1}$ . Figure 7.3 shows that under these conditions the decay kinetics is composed of a fast and a slow component. Fitting two exponentials to the measured profiles, we obtained 1/e decay times of  $\tau_F = 150 \mu\text{s}$  and  $\tau_S = 900 \mu\text{s}$  contributing to the signal for all the four lines. The intensity ratio of the fast and the slow component is found to be 1:1, the same for all the lines.

Presence of two components in decay kinetics could indicate the presence of two different centers [122]. To examine this possibility we separated PL spectra for the fast and the slow components by integrating the signal over time windows

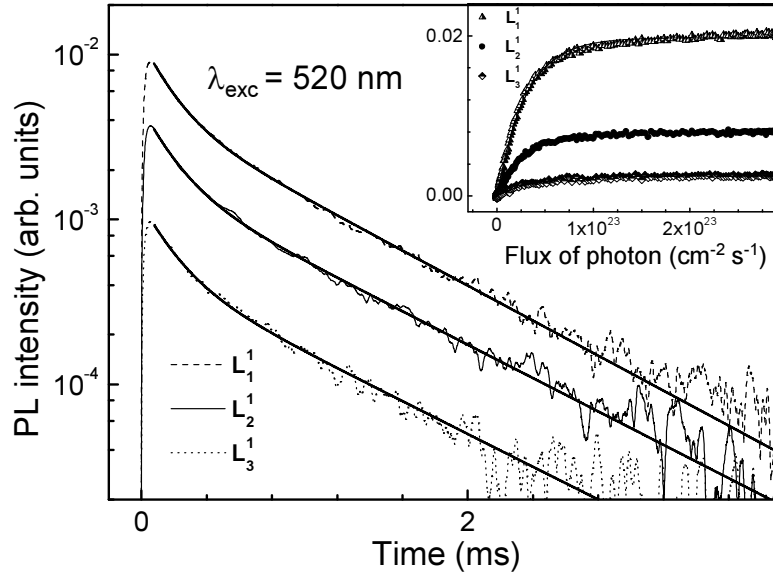


Figure 7.3: *PL decay at 4.2 K for lines  $L_1^1$ ,  $L_2^1$  and  $L_3^1$  under  $\lambda_{exc} = 520$  nm of pulse laser and  $\Phi = 3 \times 10^{22} \text{ cm}^{-2} \text{ s}^{-1}$ . The inset shows the power dependence of these lines with pulse laser*

$t \in [0, 100 \mu\text{s}]$  for the fast and  $t \in [100 \mu\text{s}, 4 \text{ ms}]$  for the slow component. The spectra are found to be identical, regardless of the different decay time constants. Taking into account the very small linewidth of the investigated PL lines, we conclude that a possibility of a co-existence of two different Er-related centers is not consistent with our findings. The PL intensity of these prominent emission lines as a function of excitation density up to  $3 \times 10^{23} \text{ cm}^{-2} \text{ s}^{-1}$  is shown in the inset of the Fig. 7.3. By looking at the decay kinetics at different excitation densities, we find that the intensity ratio of the fast to the slow component increases with the laser power. While this issue is still under investigation, this suggests that two different de-excitation processes take place for the same center. The slow component is likely to represent the radiative decay time of Er ion in silicon which is generally assumed to be around 1 ms. The fast component could be induced by an Auger process with free carriers generated by the excitation pulse.

To obtain quantitative information from the pulsed laser measurements, we use the following rate equation, involving the carrier density  $n$ , the density of exciton  $n_{ex}$ , and the concentration of excited Er center  $N_{Er}^*$ :

$$\frac{dN_{Er}^*}{dt} = \sigma\Phi(N_{Er}^{ex} - N_{Er}^*) - N_{Er}^*\left(\frac{1}{\tau}\right), \quad (7.3a)$$

$$\sigma = \alpha c_A \tau_{ex}. \quad (7.3b)$$

$N_{Er}^{ex}$  is the total concentration of excitable  $Er^{3+}$  ions present in the sample,  $\alpha$  is the absorption coefficient of silicon,  $c_A$  is the capture coefficient of free excitons by erbium-related centers with erbium excitation,  $\tau_{ex}$  and  $\tau$  are the effective lifetime of exciton and  $Er^{3+}$  in the excited state. The exciton lifetime,  $\tau_{ex}$ , is controlled mainly by nonradiative Auger processes associated with presence of Er-related donors or other impurities. We assume that the binding of free carriers into free excitons dominates at low temperatures (for more details see Appendices). The decay time  $\tau$  corresponds to an effective lifetime of  $Er^{3+}$  ions in the excited state due to both radiative and nonradiative recombinations:

$$\frac{1}{\tau} = \frac{1}{\tau_{rad}} + c_{A,Er} n, \quad (7.4)$$

where  $\tau_{rad}$  is the decay time of excited Er centers by radiative transitions and  $c_{A,Er}$  is the coefficient of the Auger process of nonradiative recombination of excited  $Er^{3+}$  ions. Eq. [7.3a] concerns concentration of excited Er centers with two possible de-excitation paths: radiative emission with spontaneous emission time  $\tau_{rad}$  and Auger quenching process which is proportional to the density of free carries. In the present experiment, the duration of the OPO pulse ( $\Delta t = 5$  ns) is much shorter than the characteristic lifetime  $\tau$  of  $Er^{3+}$  in the excited state ( $\Delta t \ll \tau$ ). We assume that recombination does not take place during illumination, and the population  $N_{Er}^*$  reaches the level of:

$$N_{Er}^*(t = \Delta t) = N_{Er}^{ex}[1 - exp(-\sigma\Phi\Delta t)]. \quad (7.5)$$

For low excitation density, when  $\sigma\Phi\Delta t \ll 1$ , this formula gives a linear dependence on flux:  $N_{Er}^* = \sigma\Phi N_{Er}^{ex}\Delta t$ . When  $\sigma\Phi\Delta t \gg 1$ , the saturation regime can be obtained:  $N_{Er}^* = N_{Er}^{ex}$ . Since in the experiment the PL signal is integrated in time, and the PL intensity is proportional to  $N_{Er}^*/\tau_{rad}$ , the result of the experiment is given by  $N_{Er}^*\tau/\tau_{rad}$ . By fitting all the data for  $L_1^1$ ,  $L_2^1$  and  $L_3^1$  in the inset of Fig. 7.3 with Eq. 7.5 we obtain the excitation cross section of  $Er^{3+}$  ions for all these emission lines as  $\sigma = (6 \pm 2) \times 10^{-15}$  cm<sup>2</sup> of the Er-1 center. This value is in a good agreement with that obtained for cw laser measurements - Fig. 7.2, and close to previous reports for Er-implanted silicon [123]. While physical interpretation of this experimentally determined “effective” excitation cross section is cumbersome, this suggests that, in general, the Er-1 center could have a similar excitation mechanism to that of other Er-related optically active centers in Si, e.g. in samples prepared by ion implantation.

Figure 7.4 shows the dependence of PL intensity at  $\lambda = 1.538$   $\mu\text{m}$  ( $L_1^1$ ) as a function of excitation density for photon flux up to  $3 \times 10^{25}$  at  $\lambda_{exc} = 520, 855, 1035$  nm. For  $\lambda_{exc} = 520$  nm the PL intensity increases rapidly with the flux of photons,

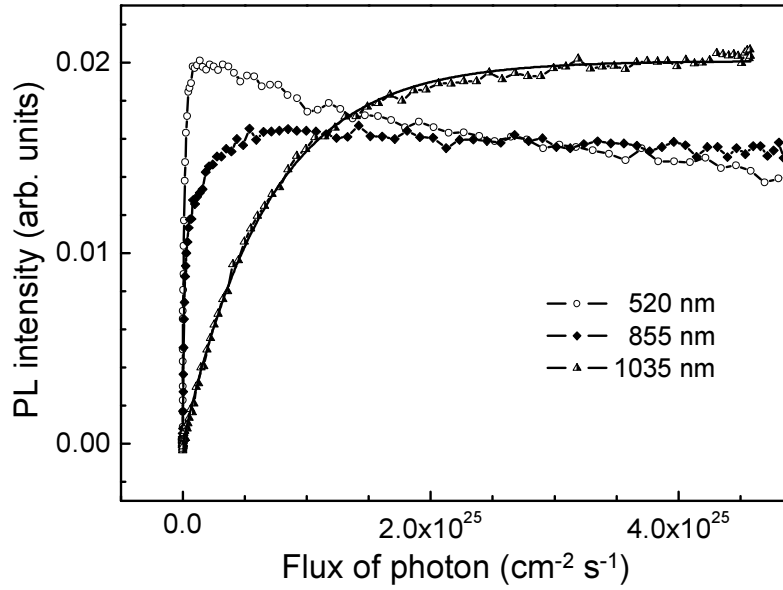


Figure 7.4: *PL intensity at  $\lambda = 1.538 \mu\text{m}$  ( $L_1^1$ ) as function of the pulsed excitation density for three different excitation wavelength  $\lambda_{exc} = 520, 855$  and  $1035 \text{ nm}$*

reaches a maximum, and then quenches for a still higher flux of photons. For  $\lambda_{exc} = 855 \text{ nm}$  excitation, the PL intensity goes up to a saturation level. The saturation level in this case is lower than for  $\lambda_{exc} = 520 \text{ nm}$  excitation, and roughly equal to its level reduced at the high photon flux. For the  $\lambda_{exc} = 1035 \text{ nm}$ , the PL intensity slowly increases with the flux of photons to the saturation level equal to the maximum found for  $\lambda_{exc} = 520 \text{ nm}$ . By fitting the latter curve with Eq. 7.5, we find the excitation cross section for Er ion at  $\lambda_{exc} = 1035 \text{ nm}$  as  $\sigma = (5 \pm 1) \times 10^{-17} \text{ cm}^2$ . In this case, the excitation cross section is lower by two orders of magnitude than the value at  $\lambda_{exc} = 520 \text{ nm}$ . This can be fully accounted for by the fact that the excitation of erbium ions proceeds via Si lattice whose absorption coefficient decreases sharply at longer wavelengths.

In Fig. 7.5a the decay characteristic of the PL intensity at  $\lambda = 1.538 \mu\text{m}$  (line  $L_1^1$ ) for  $\lambda_{exc} = 520 \text{ nm}$  is shown for selected values of photon flux:  $\Phi = 3 \times 10^{22}, 6 \times 10^{22}, 4.5 \times 10^{23}$  and  $3 \times 10^{25} \text{ cm}^{-2}\text{s}^{-1}$ . The ratios of PL intensity of fast and slow components increase with the flux of photons and are determined, respectively, as (1:1), (1.3:1), (1.5:1), (2.2:1). At higher flux of photons the fast component is prominent. This is consistent with a clear quenching PL intensity shown in Fig. 7.4 at high flux values and, again, points to a possible Auger process with free carriers which could become significant at high excitation density, as its origin.

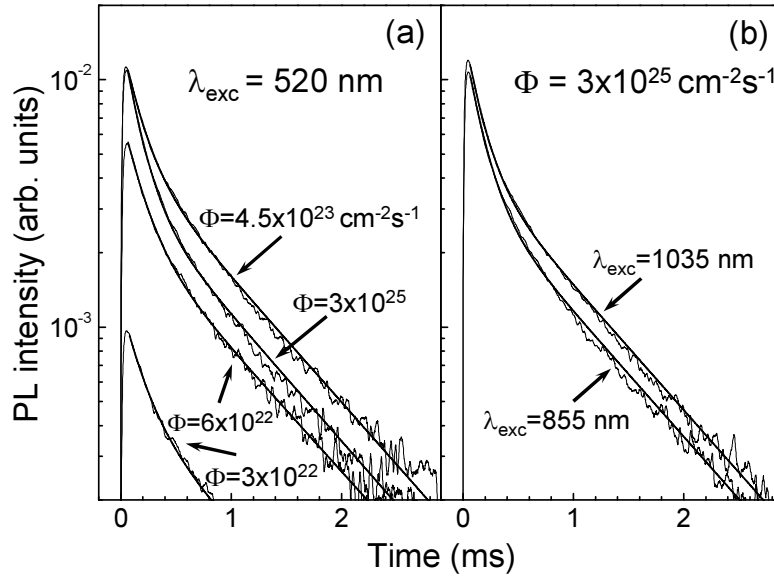


Figure 7.5: PL decay at 4.2 K with (a) -  $\lambda_{exc} = 520$  nm for four different flux of photons; (b) -  $\Phi = 3 \times 10^{25} \text{ cm}^{-2} \text{ s}^{-1}$  for two different excitation wavelengths

For the  $\lambda_{exc} = 855$  nm excitation, the saturation level is not identical to that for  $\lambda_{exc} = 520$  nm. At this wavelength, the penetration depth is of the same order as the thickness of the optically active layer and larger than the penetration depth of  $\lambda_{exc} = 520$  nm excitation. This could promote the Auger process: with a high concentration of carriers in the optically active layer, the Auger process is more probable. In case of  $\lambda_{exc} = 1035$  nm excitation wavelength, the penetration depth considerably exceeds the thickness of the optically active layer: less carriers are generated in the optically active region and so PL intensity increases slowly with the flux of photons. This scenario is also consistent with the results shown in Fig. 7.5b: the ratio of the fast and the slow components at  $\lambda_{exc} = 855$  nm excitation is higher than at  $\lambda_{exc} = 1035$  nm. We note that the decay kinetics of  $\lambda_{exc} = 520$  nm excitation at maximum intensity is identical to that observed for  $\lambda_{exc} = 1035$  nm at maximum flux of photons.

An estimate of the number of emitting centers can be made by comparing the PL intensity of Si:Er Sample #51 with that of the SiO<sub>2</sub>:Er sample measured under the same conditions. Figure 7.6 shows the dependence of PL intensity at  $\lambda = 1.538 \mu\text{m}$  as a function of excitation density for  $\lambda_{exc} = 520$  nm. From the measurements, we conclude that the intensity of emission from SiO<sub>2</sub>:Er sample shows a linear dependence over the whole investigated flux range. In this case, the integrated PL intensity is proportional to  $N_{Er}^*(\tau/\tau_{rad}) = \sigma\Phi N_{Er(SiO_2):Er}^{ex} \Delta t(\tau/\tau_{rad})$ . For the SiO<sub>2</sub>:Er system the values of all the parameters are known:  $\sigma_{SiO_2:Er}^{520 \text{ nm}} = 2 \times 10^{-20}$

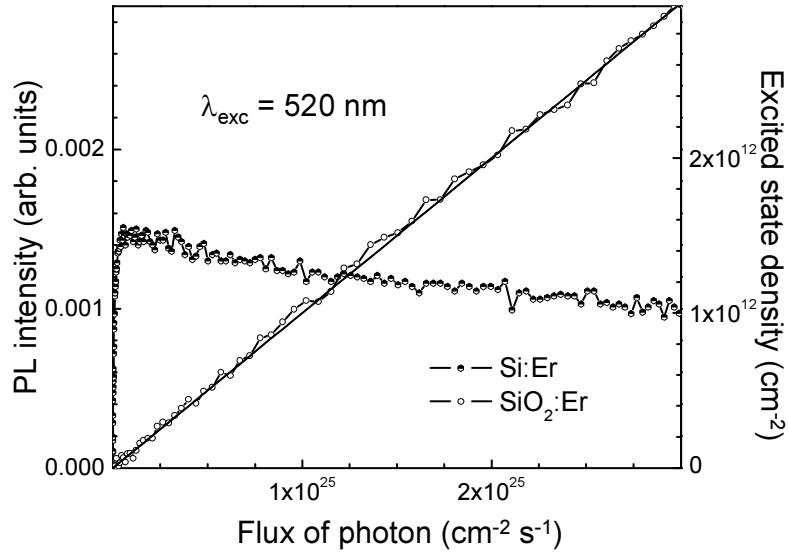


Figure 7.6: *PL intensity at  $\lambda = 1.538 \mu\text{m}$  ( $L_1^1$ ) as function of the pulsed excitation density for Si:Er and SiO<sub>2</sub>:Er samples under excitation wavelength  $\lambda_{exc} = 520 \text{ nm}$ . The right hand scale shows the density of Er<sup>3+</sup> ions in the excited state in SiO<sub>2</sub>:Er sample*

cm<sup>2</sup> [124], and  $N_{Er}^{ex} = 9.9 \times 10^{14} \text{ cm}^{-2}$  (we assume that all the implanted ions are optically active). Further, we take  $\tau/\tau_{rad} = 1$ . Therefore, the well-characterized SiO<sub>2</sub>:Er system can be used to attribute the PL intensity to a particular density (cm<sup>-2</sup>) of excited Er<sup>3+</sup> ions, as given by the right hand scale in Fig. 7.6.

In order to compare emission from the two investigated samples we note that the ratio of time integrated PL intensities is given by:

$$\frac{I_{Si:Er}}{I_{SiO_2:Er}} = \frac{\eta_{out}^{Si} \times a}{\eta_{out}^{SiO_2}} \frac{N_{Er}^* \times (\tau_1/\tau_1^{rad})}{N_{Er(SiO_2:Er)}^* \times (\tau_2/\tau_2^{rad})}, \quad (7.6)$$

where  $\tau_{1,2}$ ,  $\tau_{1,2}^{rad}$ ,  $N_{Er,Er(SiO_2:Er)}^*$ ,  $\eta_{out}^{Si, SiO_2}$  correspond to the effective and radiative decay times, density of excited Er<sup>3+</sup> ions, and the fraction of emitted photons that are collected in the apparatus (extraction efficiency), respectively, for Si:Er and SiO<sub>2</sub>:Er sample.  $a$  indicates photon loss due to surface reflection: the Si surface reflection loss reduces the absorbed power by about 70% while reflection loss for SiO<sub>2</sub> can be neglected. The ratio of the extraction loss can be calculated from the refractive indexes of Si and SiO<sub>2</sub>:

$$\frac{\eta_{out}^{Si}}{\eta_{out}^{SiO_2}} = \frac{\frac{1}{4} \times \frac{n_{air}^2}{n_1^2}}{\frac{1}{4} \times \frac{n_{air}^2}{n_2^2}} \simeq 0.175, \quad (7.7)$$

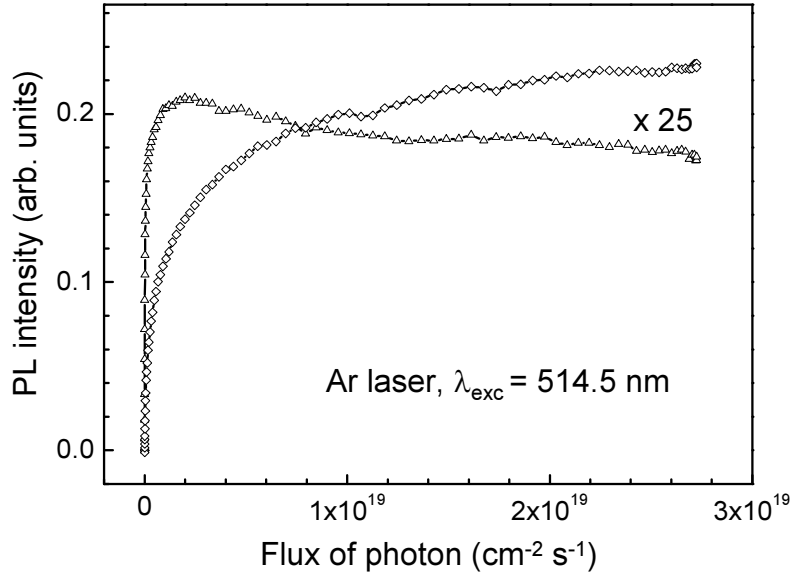


Figure 7.7: *PL intensity at  $\lambda = 1.538 \mu\text{m}$  ( $L_1^1$ ) as function of the pulsed excitation density for sample #51 and sample J900 under cw argon laser  $\lambda_{exc} = 514.5 \text{ nm}$ .*

where  $n_1, n_2$  are the refractive indexes of 3.49 and 1.46 at  $1.5 \mu\text{m}$  emission for Si and  $\text{SiO}_2$ , respectively.

For Si, the  $\text{Er}^{3+}$  excited state population should be corrected due to nonradiative contribution to the effective lifetime. If we assume the slow component in the decay kinetic to represent radiative recombination, the correction of the integrated PL intensities is given by:

$$\frac{I_{\text{Si:Er}}}{I_{\text{total}}} = \frac{A_F \tau_F + A_S \tau_S}{(A_F + A_S) \tau_S} = \frac{A_F/A_S \tau_F + \tau_S}{(A_F/A_S + 1) \tau_S}, \quad (7.8)$$

where  $A_{F,S}, \tau_{F,S}$  correspond to amplitudes and decay time of the fast and the slow components of the signal, respectively. At the saturation level,  $A_F/A_S = 1.5/1$ ,  $\tau_F = 0.15 \text{ ms}$ ,  $\tau_S = 0.85 \text{ ms}$ , and we get  $I_{\text{Si:Er}}/I_{\text{total}} = 1/2$  and  $\tau_1/\tau_1^{rad} = 1/2$ . Consequently, under the same excitation conditions the excited state population in Sample #51 has to be 2 times higher in order to give PL intensity equal to that of sample  $\text{SiO}_2:\text{Er}$ .

Finally, the different spectral shape of the  $1.5 \mu\text{m}$  band in the two samples has to be accounted for: for the same intensity at a selected wavelength, the integrated PL from  $\text{SiO}_2:\text{Er}$  sample is about 3 times higher than for Sample #51. Therefore, the PL saturation observed for Si:Er sample under band to band excitation corresponds to an excited  $\text{Er}^{3+}$  density of:

$$N_{Er}^{ex} = 1.5 \times 10^{12} \times \frac{1}{0.175 \times 0.7} \times 2 \times \frac{1}{3} \approx 8.2 \times 10^{12} \text{ cm}^{-2}. \quad (7.9)$$

This implies that the percentage of the optically active  $\text{Er}^{3+}$  ions in Sample #51 is:  $P(\%) = 8.2 \times 10^{12}/2 \times 10^{14} = (4.1 \pm 0.8) (\%)$ . This value is comparable to the highest level achieved in Si:Er materials prepared by ion implantation

To cross-check this estimation, we performed a comparative measurement using the implanted Sample J900. Fig 7.7 shows the power dependence of PL intensity for the #51 and J900 samples measured under cw argon laser excitation. As can be seen, the intensity of Sample #51 is about 25 times higher than that of sample J900. The percentage of the optically active center in this sample is:

$$\begin{aligned} \frac{I_{\#51}}{I_{J900}} &= \frac{N_{\text{Er},\#51}^* \times (\tau_1/\tau_1^{\text{rad}})}{N_{\text{Er},J900}^* \times (\tau_1/\tau_1^{\text{rad}})}, \\ P = \frac{N_{\text{Er},J900}^*}{N_{\text{Er},J900}} &= \frac{1}{25} \times \frac{1}{2} \times \frac{8.2 \times 10^{12}}{3 \times 10^{12}} = 5.5 (\%), \end{aligned} \quad (7.10)$$

which agrees well with an independent measurement based on absolute number of all the photons emitted from Sample J900 [125].

We therefore conclude that about 5% of all the Er atoms present in Sample #51 are involved in optically active Er-1 centers. That implies that with an optimized sample - see data in Table 6.1, Chapter 6, the maximum percentage of optically active centers which can be realized in Si/Si:Er nanolayers can be estimated as  $\sim 32\%$ . This is about an order of magnitude higher than in any other Si:Er materials.

## 7.4 Conclusions

A detailed consideration of excitation mechanisms of the erbium in crystalline silicon prepared by SMBE, the Er-1 center, is carried out under cw and pulse lasers pumping. The overall excitation cross section for  $\text{Er}^{3+}$  ions has been evaluated as  $\sigma = (6 \pm 2) \times 10^{-15} \text{ cm}^2$ . This value is high suggesting that excitation of the Er-1 center is a very efficient process. Further, by a direct comparison with a calibrated  $\text{SiO}_2$ :Er sample, we conclude that up to  $\sim 32\%$  of the total number of  $\text{Er}^{3+}$  ions present in Si/Si:Er nanolayers can attain optical activity. This represents a considerable improvement over Si:Er prepared by ion implantation and in view of the discussion presented in the introduction paragraph of this Chapter opens new hopes towards realization of optical gain in Si:Er.



# Appendix A

## Specific Aspects of Er Excitation Across the Bulk of a Si Wafer

### A.1 Introduction

It is known that emission from Er ions implanted into a silicon wafer can be excited by an Ar laser pointed at the non-implanted side of the sample. In such a configuration, energy has to be transferred across the entire thickness of the sample (300-500  $\mu\text{m}$ ), which exceeds by 2 orders of magnitude absorption depth of a 514.5 nm line of an Ar ion laser. This effect is commonly ascribed to diffusion of excitons across the bulk of the Si wafer, and its appearance has been taken as evidence for participation of excitons in the energy transfer between Si host and  $\text{Er}^{3+}$  ions. In our earlier work we have shown that under illumination of the non-implanted side the energy transfer process leads to a delay in the onset of Er PL signal, whose magnitude depends on the excitation power. This effect is illustrated in Fig. A.1. As can be seen, for experiments conducted at low temperatures ( $T = 4.2$  K), delay times of an order of ms are measured. According to a simple diffusion model, the diffusion related delay time  $\Delta t$  between the exciton generation in the sub-surface region of the sample and its arrival at depth  $s$  is given by  $\Delta t = s^2/4D$ . For a reasonable parameter value of  $D = 90 \text{ cm}^2\text{s}^{-1}$  [126], the time delay due to diffusion for the distance of  $s \cong 350 \mu\text{m}$  is about  $3.5 \mu\text{s}$  which is 2 orders of magnitude faster than observed in the experiment.

Having excluded exciton diffusion across the silicon wafer as a possible reason for the long delay time observed in appearance of PL signal, we have considered charge accumulation at Si/Si:Er interface as an alternative mechanism. Indeed, it is generally accepted [127] that erbium implantation into oxygen-rich silicon leads to the formation of donor centers with ionization energies in the 0.1-0.25 eV range and concentration comparable to that of Er ions. For a sample prepared from

*p*-type Si, a *p-n* junction should occur in equilibrium at the boundary with the Er-implanted layer. The excitons arriving at the *p-n* junction will therefore experience the electric field related to the depletion layer formation. In this field, whose value can reach  $10^4$  V/cm, the excitons will be divided into electrons and holes. These will gradually accumulate at a junction lowering the potential. Excitons will start to appear in the Er-doped layer and excite Er only after the depletion region has been removed due to charge compensation. According to this scenario, the effect of *p-n* junction on exciton diffusion could be influenced by biasing the junction. We confirmed this hypothesis by showing that the actual value of the delay time can be tuned by a bias voltage applied to the junction.

## A.2 Experimental details

The experimental configuration for this purpose is illustrated in Fig. A.2a. It allowed for an easy change between excitation of either the implanted side or the backside of the sample, while a DC voltage (-10 V to +10 V) could be applied by electrical contacts on both surfaces. In both excitation modes PL was collected from the Er-implanted side. The experiments were performed in a closed cycle cryostat in the temperature range between  $T \approx 15$  K and  $T = 150$  K. An on-off modulated (25 Hz) argon laser operating at  $\lambda = 514.5$  nm was used as an excitation source. The emerging PL signal was monitored with a high sensitivity germanium detector (Edinburgh Instruments). Time-resolved measurements of erbium were carried out using a digital oscilloscope (Tektronic TDS 3000) in combination with an InP/InGaAs nitrogen-cooled photomultiplier tube Hamamatsu R5509-72. In this configuration, the experimentally measured system response time was 250  $\mu$ s.

The investigation was conducted for a low-energy (300 keV,  $3 \times 10^{12}$  cm<sup>-2</sup> dose) Er-implanted oxygen-rich *p*-type (B-doped) Cz-Si wafer of approximately 350  $\mu$ m thickness. The sample was also co-implanted with oxygen (40 keV,  $3 \times 10^{13}$  cm<sup>-2</sup> dose) and annealed at 900 °C in a nitrogen atmosphere for 30 minutes.

## A.3 Effect of electrical bias on PL delay time

In the initial measurement we have checked that the spectral shape of the Er-related emission was not influenced by experimental conditions, i.e., by the illumination mode (front/back side of the sample) and applied bias. Subsequently, we looked at the effect of biasing voltage on the delay time. For the purpose of this experiment contacts were made with silver paste on the opposing faces of the sample, which was then placed in the low-temperature experimental set-up allowing

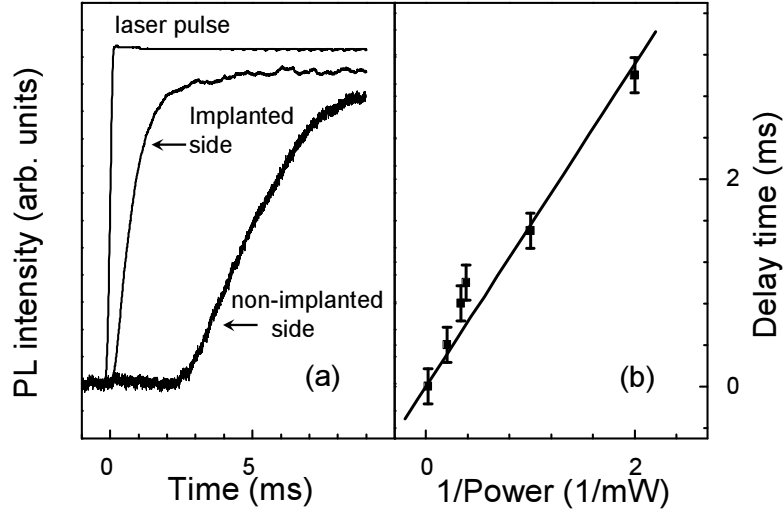


Figure A.1: *Time dependence of the intensity of Er-related PL under implanted and non-implanted side excitation. The laser pulse is also shown. In the inset, the delay time observed for the non-implanted side excitation is plotted as a function of (inverse) laser power.*

for measurements in the two illumination configurations (Fig. A.2a). In addition, DC voltage from a stabilized power supply could now be applied, providing electric field across the thickness of the sample. The results, depicted in Fig. A.2b, clearly show that the delay time can be tuned by the applied voltage increasing upon reverse bias and shortening upon forward bias [128]. Following our interpretation, under conditions of reverse bias the delay time can be increased as the depletion region increases; the delay time can be brought down to zero under forward bias which reduces the depletion region to a level at which excitons diffusing towards the Er-implanted layer are no longer destroyed. The effect is very similar to the delay time reduction upon increase of excitation density (Fig. A.1(b)).

In order to evaluate quantitatively if the junction effect can account for the observed delay we have to estimate the time necessary to compensate the change in the depleted region. The width of the depletion region is controlled by boron doping, and at low temperatures is given by:

$$W \cong \sqrt{\frac{\varepsilon (E_g - (E_D + E_B) / 2)}{2\pi e^2 N_B}}, \quad (\text{A.1})$$

where  $E_g$  is the energy gap,  $E_D$  and  $E_B$  are the binding energies of the Er-related donors and boron acceptors, respectively,  $e$  is the electron charge, and  $\varepsilon$  is the

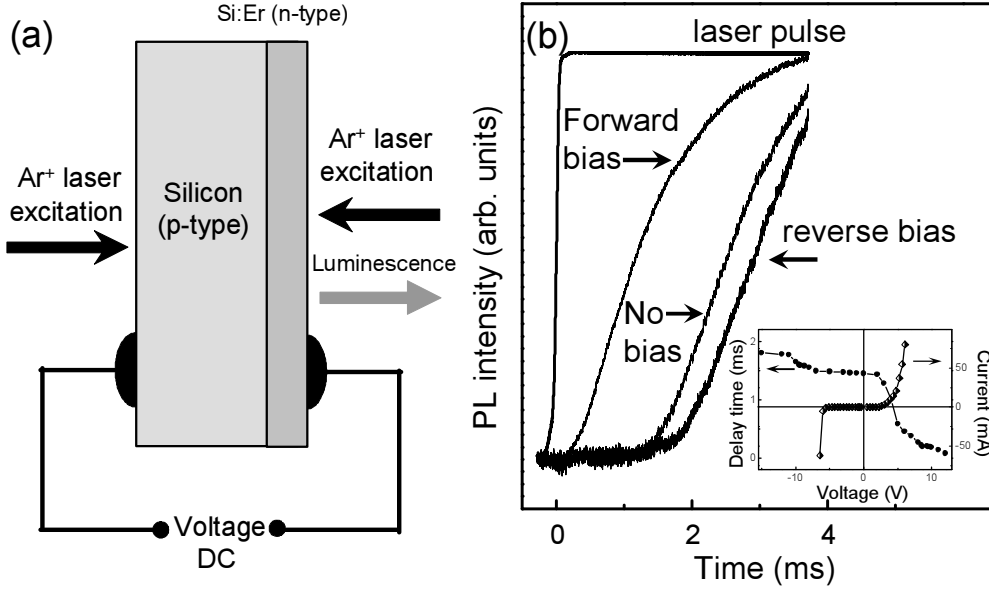


Figure A.2: (a) - Experiment allowing for excitation either of surface of the sample and for application of electrical bias. PL is detected from the Er implanted side of the sample. (b) - The effect of electrical bias on time development of the Er-related PL signal under non-implanted side excitation. The laser pulse is also shown. The inset shows the delay time of the Er PL observed for non-implanted side excitation as a function of electrical bias, and I-V characteristics of the (p-type) sample used in the experiment.

dielectric constant of silicon. The calculated depletion region of about  $1 \mu\text{m}$  is situated predominantly in the p-type layer. The negative charge ( $-N_B W$ ) is accumulated in the depletion region of the p-type layer, and the same positive charge ( $+N_D W_D = N_B W$ ) is in the n-type layer.  $N_B$  and  $N_D$  are the concentration of boron and Er-related donor center, respectively.

The time  $\delta t$  which is needed for the destruction of the p-n junction can be found from the equation:

$$\int_0^{\delta t} dt j_{ex}(s, t) = N_B W, \quad (\text{A.2})$$

where  $j_{ex}(s, t)$  is the exciton density flux. This can be obtained if consider the case of excitation by a green laser (515.4 nm) pointed at the wafer side opposite to the Er-implanted layer. In that case the relevant parameters are as follows: photon energy  $\hbar\nu = 2.4 \text{ eV}$ , absorption coefficient  $\alpha = 10^4 \text{ cm}^{-1}$ , and pumping intensity  $I = 3 \times 10^{16} \text{ cm}^{-2}\text{s}^{-1}$  for 0.4 mW. At low temperatures, for such a pumping-level

excitonic recombination dominates, and practically all created electron-hole pairs transform into excitons. As a result we have an exciton source  $S(x, t)$  near the surface (at  $x = 0$ ):

$$\frac{\partial N_{ex}}{\partial t} = D \frac{\partial^2 N_{ex}}{\partial x^2} - \frac{N_{ex}}{\tau_{ex}} + \alpha I g(t) \exp(-\alpha x), \quad (\text{A.3})$$

for a continuous pumping:

$$\frac{\partial N_{ex}}{\partial x} = 0 \quad \text{at } x = 0.$$

From that we can get the exciton density flux  $j_{ex}(x, t) = -D \partial N_{ex} / \partial x$  at  $x = s \gg \alpha^{-1}$  and for  $t < t_0$  [129, 130]:

$$j_{ex}(s, t) = \frac{I}{\sqrt{\pi}} \int_0^{t/\Delta t} dz \frac{1}{z^{3/2}} \exp \left[ - \left( \frac{1}{z} + \frac{s^2}{4L^2} z \right) \right]. \quad (\text{A.4})$$

Here  $N_{ex}$ ,  $D$ , and  $\tau_{ex}$  are the exciton concentration, diffusion coefficient, and the exciton lifetime, respectively, and  $g(t)$  describes the temporal evolution of the pump:  $g(t) = 1$  for  $t = t_0$ , and  $g(t) = 0$  for  $t > t_0$ , where the excitation laser is switched off at  $t = t_0$ . We introduce parameter  $\Delta t = s^2/4D$  and the diffusion length of the excitons  $L = \sqrt{D\tau_{ex}}$ . As mentioned above, the parameter  $\Delta t$  determines the diffusion-related time delay, i.e. the time necessary for an exciton to arrive at distance  $s$  due to diffusion.

Assuming the fast diffusion process we can use the equilibrium formula for finding the delay time  $\delta t$ :

$$\delta t \frac{\sqrt{\pi}}{2\sqrt{2}} I \exp(-s/L) = N_B W. \quad (\text{A.5})$$

From here the diffusion length  $L$  can be estimated. With the experimentally obtained value of the delay time  $\delta t$  in the millisecond range, we get  $L \approx 60 \mu\text{m}$ . Such a diffusion length corresponds to an exciton lifetime of  $\tau_{ex} \approx 0.4 \mu\text{s}$ . Therefore we conclude that the presence of the  $p$ - $n$  junction can lead to the observed delay time. Also we note that from Eq. A.5 we get  $\delta t \sim 1/I$ , which is also supported by experiment - see Fig. A.1(b).

## A.4 Excitation cross section of erbium in silicon

At low temperatures, the most probable excitation mechanism of  $\text{Er}^{3+}$  ions in crystalline silicon under optical pumping is by exciton recombination. In the case

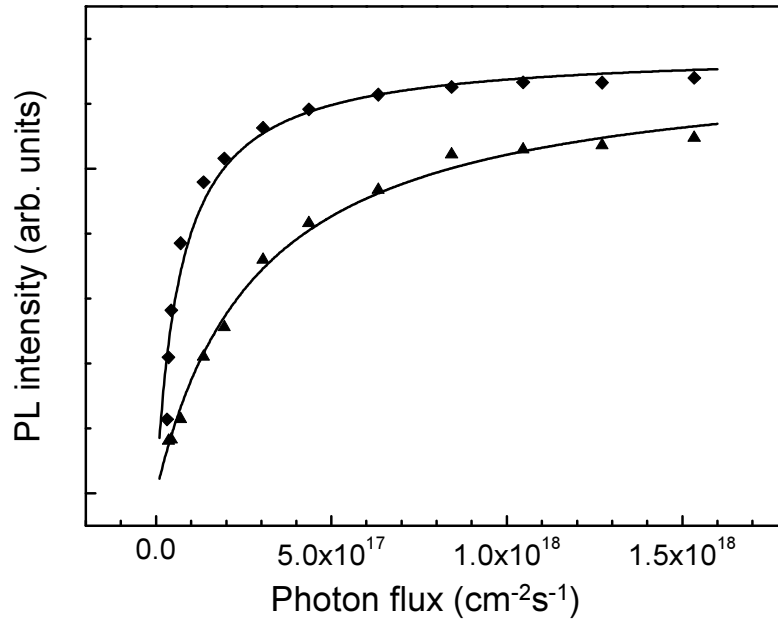


Figure A.3: *Intensity of Er-related PL under implanted (diamonds) and nonimplanted (triangles) side excitation as a function of pumping photon flux (Ar laser excitation). Solid lines are fitting curves to Eq. A.13.*

of band-to-band absorption in the matrix free excitons are formed. Neutral (at low temperatures) donors introduced by erbium and/or erbium-oxygen complexes easily capture them. Excitation of an erbium ion occurs via an Auger recombination of excitons in which the recombination energy is transferred by Coulomb interaction to an electron of  $4f$  shell of the erbium ion. Alternatively the Auger process could take place at collisions of free excitons with donors associated with erbium ions. The presence of a donor electron facilitates the energy conservation in the Auger process.

In order to describe the excitation process, we consider first the rate equations governing concentrations of free electrons and holes. We note that at low temperatures nonradiative recombination via deep centers is suppressed, and the recombination via shallow donor and acceptor centers is negligible. Though the capture cross section of electrons and holes by shallow Coulomb centers is sufficiently large, the interimpurity recombination rate is low, and shallow centers are instantly filled by charge carriers blocking this recombination channel. For this reason binding of free carriers into free excitons dominates at low temperatures and at fairly high pumping levels. Under these conditions rate equations for

electrons and holes will have the form

$$\frac{dn}{dt} = \frac{dp}{dt} = \alpha\Phi - \gamma np \quad (\text{A.6})$$

where  $\Phi$  is the flux of pumping photons, and  $\alpha$  absorption coefficient of silicon,  $n$  and  $p$  are the concentrations of nonequilibrium electrons and holes, respectively, and  $\gamma$  is the coefficient of the exciton binding process. The rate equation for free excitons can be written as follows:

$$\frac{dn_{ex}}{dt} = \gamma np - \frac{n_{ex}}{\tau_{ex}}, \quad (\text{A.7})$$

where  $\tau_{ex}$  is the exciton lifetime.

We assume that the exciton lifetime is controlled mainly by nonradiative Auger processes associated with neutral Er-related donors or other impurities,

$$\frac{1}{\tau_{ex}} \cong c_{im}N_{im} + c_{Er}N_{Er} + c_A(N_{Er} - N_{Er}^*), \quad (\text{A.8})$$

where  $N_{Er}$  is a total concentration of optically active erbium,  $N_{Er}^*$  is the concentration of excited erbium,  $N_{im}$  is the concentration of other impurities,  $c_{im}$ ,  $c_{Er}$ , and  $c_A$  are the capture coefficients of free excitons by impurities (including also optically nonactive erbium), erbium-related donor centers without erbium excitation and with erbium excitation, respectively. In Eq. A.8 we took into account possible saturation of excited erbium, which leads to blocking of Er excitation process.

The rate equation, which describes excitation of erbium ions, has the form

$$\frac{dN_{Er}^*}{dt} = c_A n_{ex} (N_{Er} - N_{Er}^*) - \frac{N_{Er}^*}{\tau}, \quad (\text{A.9})$$

where  $\tau$  is the lifetime of erbium in the excited state.

In order to analyze the rate equations A.6 – A.9, we shall separate our physical system into two subsystems. One of them (fast) has the relaxation times of all the processes involved not exceeding several microseconds: capture of free excitons by donors induced by erbium or some other impurities. The other one (slow) is characterized by time constant larger by two orders of magnitude: the lifetime of erbium ions in the excited state. Therefore we can regard the “fast” subsystem to be in a quasistationary state and get

$$n_{ex} = \alpha\Phi\tau_{ex}. \quad (\text{A.10})$$

In this approximation, the rate equation has the form:

$$\frac{dN_{Er}^*}{dt} = \sigma_{eff}\Phi(N_{Er} - N_{Er}^*) - \frac{N_{Er}^*}{\tau}, \quad (\text{A.11})$$

where we have introduced the effective cross section of erbium excitation  $\sigma_{eff}$  [131]:

$$\sigma_{eff} = \alpha C_A \tau_{ex}. \quad (\text{A.12})$$

The excitation cross section can be obtained from the experimental power dependence of erbium luminescence intensity. From the stationary solution of Eq. A.11 the dependence of erbium luminescence intensity on photon flux should depend on the excitation cross section  $\sigma$ :

$$I_{Er} \propto \frac{N_{Er}^*}{\tau_{rad}} = \frac{\sigma_{eff} \tau \Phi}{1 + \sigma_{eff} \tau \Phi} \frac{N_{Er}}{\tau_{rad}}. \quad (\text{A.13})$$

One can expect that the excitation cross section from the non-implanted side excitation is less effective due to the  $p - n$  junction effect and the diffusion of excitons in the silicon. Indeed, Fig. A.3 shows the power dependence of Er luminescence under excitation from implanted and non-implanted side. Taking the lifetime of erbium to be  $\tau_{Er} = 1.3$  ms for both configurations we have obtained  $\sigma_{eff} = (1 - 3) \times 10^{-15}$  and  $\sigma_{eff} = (6 - 8) \times 10^{-16}$  cm<sup>-2</sup> for the implanted and non-implanted side excitations, respectively.

# Appendix B

## The Effects of Stress and Magnetic Fields

The effects of stress and magnetic fields on a  $T_2$  state coupled to a spin of 1. The matrix is ordered as  $|\text{spin}\rangle |\text{orbital}\rangle$ , with the orbital parts defined in Chapter 3. Terms in the lower section of the matrix are given by the complex conjugates of the corresponding terms in the upper part.



# References

- [1] B. A. I. Monemar. Electron structure and bound excitons for defects in semiconductors from optical spectroscopy. *CRC Critical Review in Solid State and Materials Sciences* **15**, 111 (1988).
- [2] F. Bassani, G. Iadonisi, and B. Preziosi. Electronic impurity levels in semiconductors. *Rep. Prog. Phys.* **37**, 1099 (1974).
- [3] S. T. Pantelides. The electronic structure of impurities and other point defects in semiconductors. *Rev. Mod. Phys.* **50**, 797 (1978).
- [4] G. Davies. The optical properties of luminescence centers in silicon. *Physics Reports* **176**, 83 (1989).
- [5] O. King and D. G. Hall. Impurity-related photoluminescence from silicon at room temperature. *Phys. Rev. B* **50**, 10661 (1994).
- [6] G. Bohnert, K. Weronek, and A. Hangleiter. Transient characteristics of isoelectronic bound excitons at hole-attractive defects in silicon: The C(0.79 eV), P(0.767 eV), and H(0.926 eV) lines. *Phys. Rev. B* **48**, 14973 (1994).
- [7] H. Ennen, J. Schneider, G. Pomrenke, and A. Axmann. 1.54- $\mu$ m luminescence of erbium-implanted III-V semiconductors and silicon. *Appl. Phys. Lett.* **43**, 943 (1983).
- [8] <http://www.rijnh.nl/>.
- [9] J. Weber, H. Bauch, and R. Sauer. Optical properties of copper in silicon: Excitons bound to isoelectronic copper pairs. *Phys. Rev. B* **25**, 7688 (1982).
- [10] T. G. Brown and D. G. Hall. Optical emission at 1.32  $\mu$ m from sulfur-doped crystalline silicon. *Appl. Phys. Lett.* **49**, 245 (1986).
- [11] K. Thonke, J. Weber, J. Wagner, and R. Sauer. Origin of the 1.080 eV ( $I_2$ ) photoluminescence line in irradiated silicon. *Physica B* **116**, 252 (1983).

- 
- [12] A. N. Safonov, E. C. Lightowers, G. Davies, P. Leary, R. Jones, and S. Oberg. Interstitial-carbon hydrogen interaction in silicon. *Phys. Rev. Lett.* **77**, 4812 (1996).
- [13] G. Davies. Configurational instabilities at isoelectronic centers in silicon. *Phys. Scripta* **54**, 7 (1994).
- [14] G. Davies. Magnetic perturbations of excitons bound to an isoelectronic hydrogen-related defect in silicon. *Phys. Rev. B* **51**, 13783 (1995).
- [15] L. D. Yau and C. T. Sah. Measurement of trapped-minority-carrier thermal emission rates from Au, Ag, and Co traps in silicon. *Appl. Phys. Lett.* **21**, 157 (1972).
- [16] P. Migliorato, C. T. Elliott, and A. W. Vere. Photo-excitation of electrons from ionized silver acceptors in silicon. *Solid State Commun.* **24**, 117 (1977).
- [17] N. Baber, H. G. Grimmeiss, M. Kleverman, P. Omling, and M. Z. Iqbal. Characterization of silver-related deep levels in silicon. *J. Appl. Phys.* **62**, 2853 (1987).
- [18] N. T. Son, V. E. Kustov, T. Gregorkiewicz, and C. A. J. Ammerlaan. Electron-paramagnetic-resonance identification of silver centers in silicon. *Phys. Rev. B* **46**, 4544 (1992).
- [19] N. T. Son, T. Gregorkiewicz, and C. A. J. Ammerlaan. Magnetic resonance spectroscopy in silver-doped silicon. *J. Appl. Phys.* **73**, 1797 (1993).
- [20] P. N. Hai, T. Gregorkiewicz, C. A. J. Ammerlaan, and D. T. Don. Electron-paramagnetic-resonance study of silver-induced defects in silicon. *Phys. Rev. B* **56**, 4614 (1997).
- [21] J. Olajos, M. Kleverman, and H. G. Grimmeiss. High-resolution spectroscopy of silver-doped silicon. *Phys. Rev. B* **38**, 10633 (1988).
- [22] M. H. Nazare, M. C. Carmo, and A. J. Duarte. Luminescence from transition metal centers in silicon doped with silver and nickel. *Mater. Sci. Eng. B* **4**, 273 (1989).
- [23] M. Kleverman, J. Olajos, G. Grossmann, B. Bech-Nielsen, and H. G. Grimmeiss. Excited-state spectroscopy of deep defects in silicon. *Phys. Scripta* **T25**, 134 (1989).

- 
- [24] J. H. Svensson, B. Monemar, and E. Janzen. Pseudodonor electronic excited states of neutral complex defects in silicon. *Phys. Rev. Lett.* **65**, 1796 (1990).
- [25] M. Z. Iqbal, G. Davies, and E. C. Lightowers. Photoluminescence from silver-related defects in silicon. *Mat. Sci. Forum* **143-147**, 773 (1994).
- [26] N. T. Son, M. Singh, J. Dalfors, B. Monemar, and E. Janzen. Electronic structure of a photoluminescent center in silver-doped silicon. *Phys. Rev. B* **49**, 17428 (1994).
- [27] I. de Maat-Gersdorf, T. Gregorkiewicz, and C. A. J. Ammerlaan. Pseudodonor character of silver in silicon. *J. Lumin.* **60-61**, 556 (1994).
- [28] M. Singh, W. M. Chen, , N. T. Son B. Monemar, and E. Janzen. Shallow excited states of deep luminescent centers in silicon. *Solid State Commun.* **93**, 415 (1995).
- [29] M. X. Zhu, G. Davies, M. Z. Iqbal, and E. C. Lightowers. Silver-related donor defect in silicon. *Mat. Sci. Forum* **258-263**, 485 (1997).
- [30] N. Q. Vinh, M. A. J. Klik, and T. Gregorkiewicz. Time-resolved photoluminescence study of Si:Ag. *Physica B* **308-310**, 414 (2001).
- [31] N. Q. Vinh, T. Gregorkiewicz, and K. Thonke. 780-meV photoluminescence band in silver-doped silicon: Isotope effect and time-resolved spectroscopy. *Phys. Rev. B* **65**, 033202 (2001).
- [32] V. Heine and C. H. Henry. Theory of the isotope shift for zero-phonon optical transitions at traps in semiconductors. *Phys. Rev. B* **11**, 3795 (1975).
- [33] J. A. Van Vechten. Isotope shift at substitutional Cu in ZnO. *Phys. Rev. B* **13**, 946 (1976).
- [34] W. Bludau, A. Onton, and W. Heinke. Temperature dependence of the band gap of silicon. *J. Appl. Phys.* **45**, 1846 (1974).
- [35] L. D. Laude, F. H. Pollak, and M. Cardona. Effects of uniaxial stress on the indirect exciton spectrum of silicon. *Phys. Rev. B* **3**, 2623 (1971).
- [36] D. K. Wilson and G. Feher. Electron spin resonance experiments on donors in silicon. III. Investigation of excited states by the application of uniaxial stress and their importance in relaxation processes. *Phys. Rev.* **124**, 1068 (1961).

- [37] A. A. Kaplyanskii. *Opt. Spectrosc.* **16**, 329 (1964).
- [38] K. Thonke, A. Hangleiter, J. Wagner, and R. Sauer. 0.79 eV (C line) defect in irradiated oxygen-rich silicon: Excited state structure, internal strain and luminescence decay time. *J. Phys. C* **18**, L795 (1985).
- [39] G. Davies and M. C. do Carmo. in shallow impurities in semiconductors, Proceedings of the 3rd International Conference, Linköping, Sweden, 1988. *Inst. Phys. Conf. Ser. No 95, edited by B. Monemar (IOP, Bristol, 1989)*, p. 125.
- [40] R. Brout and W. Visscher. Suggested experiment on approximate localized modes in crystals. *Phys. Rev. Lett.* **9**, 54 (1962).
- [41] A. M. Zaitsev. Vibronic spectra of impurity-related optical centers in diamond. *Phys. Rev. B* **61**, 12909 (2000).
- [42] W. Schmid. Auger lifetimes for excitons bound to neutral donors and acceptors in Si. *Phys. Status Solidi B* **84**, 529, (1977).
- [43] G. C. Osbourn and D. L. Smith. Auger transition rates for excitons bound to acceptors in Si and Ge. *Phys. Rev. B* **16**, 5426 (1977).
- [44] S. A. Lyon, G. C. Osbourn, D. L. Smith, and T. C. McGill. Bound exciton lifetimes for acceptors in Si. *Solid State Commun.* **23**, 425 (1977).
- [45] G. S. Mitchard, S. A. Lyon, K. R. Elliott, and T. C. McGill. Observation of long lifetime lines in photoluminescence from Si:In. *Solid State Commun.* **29**, 425 (1979).
- [46] S. P. Watkins, U. O. Ziemelis, M. L. W. Thewalt, and R. R. Parsons. Long lifetime photoluminescence from a deep centre in copper-doped silicon. *Solid State Commun.* **43**, 687 (1982).
- [47] E. C. Lightowers, L. T. Canham, G. Davies, M. L. W. Thewalt, and S. P. Watkins. Lithium and lithium-carbon isoelectronic complexes in silicon: Luminescence-decay-time, absorption, isotope-splitting, and Zeeman measurements. *Phys. Rev. B* **29**, 4517 (1984).
- [48] J. Weber, W. Schmid, and R. Sauer. Localized exciton bound to an isoelectronic trap in silicon. *Phys. Rev. B* **21**, 2401 (1980).
- [49] N. Q. Vinh and T. Gregorkiewicz. Two-color mid-infrared spectroscopy of isoelectronic centers in silicon. *Mat. Res. Soc. Symp. Proc. Vol. 770*, I4.2.1 (2003).

- [50] G. Davies, M. Z. Iqbal, and E. C. Lightowers. Exciton self-trapping at an isoelectronic center in silicon. *Phys. Rev. B* **50**, 11520 (1994).
- [51] D. J. S. Beckett, M. K. Nissen, and M. L. W. Thewalt. Optical properties of the sulfur-related isoelectronic bound excitons in Si. *Phys. Rev. B* **40**, 9618 (1989).
- [52] P. C. M. Planken, P. C. van Son, J. N. Hovenier, T. O. Klaassen, W. Th. Wenckebach, B. N. Murdin, and G. M. H. Knippels. Far-infrared picosecond time-resolved measurement of the free-induction decay in GaAs:Si. *Phys. Rev. B* **51**, 9643 (1995).
- [53] J. M. Blackburn, D. P. Long, A. Cabanas, and J. J. Watkins. Deposition of conformal copper and nickel films from supercritical carbon dioxide. *Science* **294**, 141 (2001).
- [54] A. A. Istratov and E. R. Weber. Electrical properties and recombination activity of copper, nickel and cobalt in silicon. *Appl. Phys. A-Mater* **66**, 123 (1998).
- [55] U. Wahl, A. Vantomme, G. Langouche, J. G. Correia, and ISOLDE Collaboration. Lattice location and stability of ion implanted Cu in Si. *Phys. Rev. Lett.* **84**, 1495 (2000).
- [56] M. H. Nazare, A. J. Neves, and G. Davies. Optical studies of the 1.40-eV Ni center in diamond. *Phys. Rev. B* **43**, 14196 (1991).
- [57] H. B. Erzgraber and K. Schmalz. Correlation between the Cu-related luminescent center and a deep level in silicon. *J. Appl. Phys.* **78**, 4066 (1995).
- [58] S. K. Estreicher, D. West, J. Goss, S. Knack, and J. Weber. First-principles calculations of pseudolocal vibrational modes: The case of Cu and Cu pairs in Si. *Phys. Rev. Lett.* **90**, 035504 (2003).
- [59] K. G. McGuigan, M. O. Henry, E. C. Lightowers, A. G. Steele, and M. L. W. Thewalt. A new photoluminescence band in silicon lightly doped with copper. *Solid State Commun.* **68**, 7 (1988).
- [60] S. Knack, J. Weber, H. Lemke, and H. Riemann. Evolution of copper-hydrogen-related defects in silicon. *Physica B* **308-310**, 404 (2001).
- [61] S. K. Estreicher, D. West, and M. Sanati, private communication (2004).

- [62] K. G. McGuigan, M. O. Henry, M. C. Carmo, G. Davies, and E. C. Lightowers. A uniaxial stress study of a copper-related photoluminescence band in silicon. *Mat. Sci. Eng. B* **4**, 269 (1989).
- [63] R. L. Aggarwal and A. K. Ramdas. Optical determination of the symmetry of the ground states of group-V donors in silicon. *Phys. Rev.* **140**, A1246 (1965).
- [64] M. Forcales, M. A. J. Klik, N. Q. Vinh, J. Phillips, J-P. R. Wells, and T. Gregorkiewicz. Two-color mid-infrared spectroscopy of optically doped semiconductors. *J. Lumin.* **102-103**, 85 (2003).
- [65] G. Davies, T. Gregorkiewicz, M. Z. Iqbal, M. Kleverman, E. C. Lightowers, N. Q. Vinh, and M. Zhu. Optical properties of a silver-related defect in silicon. *Phys. Rev. B* **67**, 235111 (2003).
- [66] P. L. Bradfield, T. G. Brown, and D. G. Hall. Radiative decay of excitons bound to chalcogen-related isoelectronic impurity complexes in silicon. *Phys. Rev. B* **38**, 3533 (1988).
- [67] V. N. Abakumov, V. I. Perel, and I. N. Yassievich. *Nonradiative recombination in semiconductors*. (Modern problems in condensed matter sciences, edited by V. M. Agranovich and A. A. Maradudin, vol. **33**), North-Holland, 1991.
- [68] S. S. Iyer and Y. H. Xie. Light emission from silicon. *Science* **260**, 40 (1993).
- [69] S. Schmitt-Rink, C. M. Varma, and A. F. J. Levi. Excitation mechanisms and optical properties of rare-earth ions in semiconductors. *Phys. Rev. Lett.* **66**, 2782 (1991).
- [70] A. Polman. Erbium implanted thin films photonic materials. *J. Appl. Phys.* **82**, 1 (1997).
- [71] S. Coffa, G. Franzò, and F. Priolo. Light emission from Er-doped Si: Materials properties, mechanisms, and device performance. *Mater. Res. Bulletin* **23**, 25 (1998).
- [72] J. Palm, F. Gan, B. Zheng, J. Michel, and L. C. Kimerling. Electroluminescence of erbium-doped silicon. *Phys. Rev. B* **54**, 17603 (1996).
- [73] D. L. Adler, D. C. Jacobson, D. J. Eaglesham, M. A. Marcus, J. L. Benton, J. M. Poate, and P. H. Citrin. Local structure of 1.54- $\mu\text{m}$ -luminescence  $\text{Er}^{3+}$  implanted in Si. *Appl. Phys. Lett.* **61**, 2181 (1992).

- [74] U. Wahl, A. Vantomme, J. De Wachter, R. Moons, G. Langouche, J. G. Marques, J. G. Correia, and ISOLDE Collaboration. Direct evidence for tetrahedral interstitial Er in Si. *Phys. Rev. Lett.* **79**, 2069 (1997).
- [75] M. Needels, M. Schlüter, and M. Lannoo. Erbium point defects in silicon. *Phys. Rev. B* **47**, 15533 (1993).
- [76] H. Przybylińska, W. Jantsch, Yu. Suprun-Belevitch, M. Stepikhova, L. Palmetshofer, G. Hendorfer, A. Kozanecki, R. J. Wilson, and B. J. Sealy. Optically active erbium centers in silicon. *Phys. Rev. B* **54**, 2532 (1996).
- [77] J. D. Carey, R. C. Barklie, J. F. Donegan, F. Priolo, G. Franzò, and S. Coffa. Electron paramagnetic resonance and photoluminescence study of Er-impurity complexes in Si. *Phys. Rev. B* **59**, 2773 (1999).
- [78] observation of Zeeman effect in PL of Si:Er was claimed in several abstracts submitted to meetings devoted to defects in solids (MRS, ICDS).
- [79] B. A. Andreev, A. Yu. Andreev, H. Ellmer, H. Hutter, Z. F. Krasil'nik, V. P. Kuznetsov, S. Lanzerstorfer, L. Palmetshofer, K. Piplits, R. A. Rubtsova, N. S. Sokolov, V. B. Shmagin, M. V. Stepikhova, and E. A. Uskova. Optical Er-doping of Si during sublimational molecular beam epitaxy. *J. Cryst. Growth* **201/202**, 534 (1999).
- [80] M. V. Stepikhova, B. A. Andreev, V. B. Shmagin, Z. F. Krasil'nik, V. P. Kuznetsov, V. G. Shengurov, S. P. Svetlov, W. Jantsch, L. Palmetshofer, and H. Ellmer. Properties of optically active Si:Er and Si<sub>1-x</sub>Ge<sub>x</sub> layers grown by the sublimation MBE method. *Thin Solid Films* **369**, 426 (2000).
- [81] K. R. Lea, M. J. M. Leask, and W. P. Wolf. The raising of angular momentum degeneracy of *f*-electron terms by cubic crystal fields. *J. Phys. Chem. Solids* **23**, 1381 (1962).
- [82] N. Q. Vinh, H. Przybylińska, Z. F. Krasil'nik, B. A. Andreev, and T. Gregorkiewicz. Observation of Zeeman effect in photoluminescence of Er<sup>3+</sup> ion imbedded in crystalline silicon. *Physica B* **308-310**, 340 (2001).
- [83] G. D. Watkins, M. Kleverman, A. Thilderkvist, and H. G. Grimmeiss. Structure of gold in silicon. *Phys. Rev. Lett.* **67**, 1149 (1991).
- [84] R. K. Watts and W. C. Holton. Paramagnetic-resonance studies of rare-earth impurities in II-VI compounds. *Phys. Rev.* **173**, 417 (1968).

- [85] J. D. Kingsley and M. Aven. Paramagnetic resonance and fluorescence of  $\text{Er}^{3+}$  at cubic sites in ZnSe. *Phys. Rev.* **155**, 235 (1967).
- [86] A. G. Raffa and P. Ballone. Equilibrium structure of erbium-oxygen complexes in crystalline silicon. *Phys. Rev. B* **65**, 121309 (2002).
- [87] W. L. Ng, M. P. Temple, P. A. Childs, F. Wellhofer, and K. P. Homewood. Photoluminescence and photoluminescence excitation spectroscopy of Er-doped Si prepared by laser ablation. *Appl. Phys. Lett.* **75**, 97 (1999).
- [88] W. Jantsch, S. Lanzerstorfer, M. Stepikhova, H. Preier, and L. Palmetshofer. Status, hopes and limitations for the Si:Er-based 1.54  $\mu\text{m}$  emitter. *Solid State Phenom.* **70**, 53 (1999).
- [89] R. S. Smith, H. D. Muller, H. Ennen, P. Wennekers, and M. Maier. Erbium doping of molecular beam epitaxial GaAs. *Appl. Phys. Lett.* **50**, 49 (1987).
- [90] K. Thonke, H. U. Hermann, and J. Schneider. A Zeeman study of the 1.54  $\mu\text{m}$  transition in molecular beam epitaxial GaAs:Er. *J. Phys. C* **21**, 5881 (1988).
- [91] H. Ennen, J. Wagner, H. D. Muller, and R. S. Smith. Photoluminescence excitation measurements on GaAs:Er grown by molecular-beam epitaxy. *J. Appl. Phys.* **61**, 4877 (1987).
- [92] K. Takahei, A. Taguchi, Y. Horikoshi, and J. Nakata. Atomic configuration of the Er-O luminescence center in Er-doped GaAs with oxygen codoping. *J. Appl. Phys.* **76**, 4332 (1994).
- [93] T. Ishiyama, E. Katayama, K. Murakami, K. Takahei, and A. Taguchi. Electron spin resonance of Er-oxygen complexes in GaAs grown by metal organic chemical vapor deposition. *J. Appl. Phys.* **84**, 6782 (1998).
- [94] D. Haase, A. Dornen, K. Takahei, and A. Taguchi. Study of the Zeeman effect of  $\text{Er}^{3+}$  in GaAs:Er,O. *Mat. Res. Soc. Symp. Proc.* **422**, 179 (1996).
- [95] N. Q. Vinh, H. Przybylińska, Z. F. Krasil'nik, and T. Gregorkiewicz. Microscopic structure of Er-related optically active centers in crystalline silicon. *Phys. Rev. Lett.* **90**, 066401 (2003).
- [96] V. P. Kuznetsov, A. Y. Andreev, O. A. Kuznetsov, L. E. Nikolaeva, T. M. Sotova, and N. V. Gudkova. Heavily doped Si layers grown by molecular-beam epitaxy in vacuum. *Phys. Status Solidi A* **127**, 371 (1991).

- 
- [97] W. Jantsch, S. Lanzerstorfer, L. Palmetshofer, M. Stepikhova, and H. Preier. Different Er centres in Si and their use for electroluminescent devices. *J. Lumin.* **80**, 9, (1999).
- [98] A. Abragam and B. Bleaney. *Electron Paramagnetic Resonance of Transition Ions*. Clarendon Press, Oxford, 1970.
- [99] G. H. Dieke. *Spectra and Energy Levels of Rare Earth Ions in Crystals*. Wiley, New York, 1968.
- [100] B. Bleaney. The spin hamiltonian of a  $\Gamma_8$  quartet. *Proc. Phys. Soc.* **73**, 939 (1959).
- [101] G. F. Koster, J. O. Dimmock, R. G. Wheeler, and H. Statz. *Properties of the Thirty-Two Point Groups*. MIT Press, Cambridge, Massachusetts, 1963.
- [102] U. Ranon and W. Low. Electron spin resonance of  $\text{Er}^{3+}$  in  $\text{CaF}_2$ . *Phys. Rev.* **132**, 1609 (1963).
- [103] M. J. Weber and R. W. Bierig. Paramagnetic resonance and relaxation of trivalent rare-earth ions in calcium fluoride. I. Resonance spectra and crystal fields. *Phys. Rev.* **134**, A1492 (1964).
- [104] B. L. Crowder, R. S. Title, and G. D. Pettit. EPR and luminescence studies of  $\text{Er}^{+3}$  in acceptor-doped ZnTe. *Phys. Rev.* **181**, 567 (1969).
- [105] M. Sprenger, S. H. Muller, E. G. Sieverts, and C. A. J. Ammerlaan. Vacancy in silicon: Hyperfine interactions from electron-nuclear double resonance measurements. *Phys. Rev. B* **35**, 1566 (1987).
- [106] T. Gregorkiewicz, H. H. P. Th. Bekman, and C. A. J. Ammerlaan. Microscopic structure of the NL10 heat-treatment center in silicon: Study by electron-nuclear double resonance. *Phys. Rev. B* **38**, 3998 (1988).
- [107] F. P. Widdershoven - private communication.
- [108] T. Gregorkiewicz, H. H. P. Th. Bekman, and C. A. J. Ammerlaan. Comparative study of Si-NL8 and Si-NL10 thermal-donor-related EPR centers. *Phys. Rev. B* **41**, 12628 (1990).
- [109] P. Wagner and J. Hage. Thermal double donors in silicon. *Appl. Phys. A – Mater* **49**, 123 (1989).
- [110] J. Michel, L. V. C. Assali, M. T. Morse, and L. C. Kimerling. Light emission in silicon: From physics to devices. *Semiconduct. Semimet.* **49**, 111 (1998).

- [111] E. A. Fitzgerald and L. C. Kimerling. Silicon-based microphotronics and integrated optoelectronics. *MRS Bulletin* **23**, 39 (1998).
- [112] L. Pavesi, L. Dal Negro, C. Mazzoleni, G. Franzò, and F. Priolo. Optical gain in silicon nanocrystals. *Nature* **408**, 440 (2000).
- [113] W. L. Ng, M. A. Lourenco, R. M. Gwilliam, S. Ledain, G. Shao, and K. P. Homewood. An efficient room-temperature silicon-based light-emitting diode. *Nature* **410**, 192 (2001).
- [114] N. Q. Vinh, H. Przybylińska, Z. F. Krasil'nik, and T. Gregorkiewicz. Optical properties of a single type of optically active center in Si/Si:Er nanostructures. *Phys. Rev. B* **70**, in print (2004).
- [115] N. Q. Vinh, M. Klik, B. A. Andreev, and T. Gregorkiewicz. Spectroscopic characterization of Er-1 center in selectively doped silicon. *Mat. Sci. Eng. B-Solid* **105**, 150 (2003).
- [116] M. Forcales, T. Gregorkiewicz, I. V. Bradley, and J. P. R. Wells. Afterglow effect in photoluminescence of Si:Er. *Phys. Rev. B* **65**, 195208 (2002).
- [117] M. Forcales, T. Gregorkiewicz, and J. M. Zavada. Silicon-based all-optical memory elements for 1.54  $\mu\text{m}$  photonics. *Sol. St. Electron.* **47**, 165 (2003).
- [118] P. G. Kik and A. Polman. Gain limiting processes in Er-doped Si nanocrystal waveguides in  $\text{SiO}_2$ . *J. Appl. Phys.* **91**, 534 (2002).
- [119] M. Wojdak, M. Klik, M. Forcales, O. B. Gusev, T. Gregorkiewicz, D. Pacifici, G. Franzò, F. Priolo, and F. Iacona. Sensitization of  $\text{SiO}_2$ :Er luminescence by Si nanoclusters: Temporal and concentration limits. *Phys. Rev. B* **69**, 233315 (2004).
- [120] R. Serna, J. H. Shin, M. Lohmeier, E. Vlieg, A. Polman, and P. F. A. Alkemade. Incorporation and optical activation of erbium in silicon using molecular beam epitaxy. *J. Appl. Phys.* **79**, 2658 (1996).
- [121] D. T. X. Thao, C. A. J. Ammerlaan, and T. Gregorkiewicz. Photoluminescence of erbium-doped silicon: Excitation power and temperature dependence. *J. Appl. Phys.* **88**, 1443 (2000).
- [122] S. Coffa, G. Franzò, F. Priolo, A. Polman, and R. Serna. Temperature dependence and quenching processes of the intra-4f luminescence of Er in crystalline Si. *Phys. Rev. B* **49**, 16313 (1994).

- 
- [123] F. Priolo, G. Franzò, S. Coffa, and A. Carnera. Excitation and nonradiative deexcitation processes of  $\text{Er}^{3+}$  in crystalline Si. *Phys. Rev. B* **57**, 4443 (1998).
- [124] W. J. Miniscalco. Erbium-doped glasses for fiber amplifiers at 1500-nm. *J. Lightwave Technol.* **9**, 234 (1991).
- [125] W. Jantsch - private communication.
- [126] M. A. Tamor and J. P. Wolfe. Drift and diffusion of free excitons in Si. *Phys. Rev. Lett.* **44**, 1703 (1980).
- [127] G. Franzò, F. Priolo, S. Coffa, A. Polman, and A. Carnera. Room-temperature electroluminescence from Er-doped crystalline Si. *Appl. Phys. Lett.*, **64**, 2235 (1994).
- [128] N. Q. Vinh, I. N. Yassievich, and T. Gregorkiewicz. Erbium excitation across the bulk of silicon wafer: an effect of  $p - n$  junction at Si/Si:Er interface. *Physica B* **308-310**, 357 (2001).
- [129] P. M. Chaikin and T. C. Lubensky. *Principles of condensed matter physics*. Cambridge University Press, Cambridge, New York, Melbourne, 7th edition, 1995.
- [130] B. J. Pawlak, N. Q. Vinh, I. N. Yassievich, and T. Gregorkiewicz. Influence of  $p - n$  junction formation at a Si/Si:Er interface on low-temperature excitation of  $\text{Er}^{3+}$  ions in crystalline silicon. *Phys. Rev. B* **64**, 132202 (2001).
- [131] O. B. Gusev, M. S. Bresler, P. E. Pak, I. N. Yassievich, M. Forcales, N. Q. Vinh, and T. Gregorkiewicz. Excitation cross section of erbium in semiconductor matrices under optical pumping. *Phys. Rev. B* **64**, 075302 (2001).



# Summary

This thesis deals with fundamental properties of selected optically active isoelectronic centers in silicon.

The radiative decay of excitons bound to isoelectronic impurities is an important physical process in crystalline semiconductors. This is particularly true in indirect band-gap semiconductor like GaP, Si, in which the band-to-band radiative transitions are forbidden by the  $\vec{k}$ -conservation rule. Therefore motivation for the presented study comes from practical importance of silicon photonics as the way for integration of electronic and optical elements. In addition, exciton bound to copper or silver related centers in Si, and Er dopant which can receive energy by binding an exciton can emit infrared light at a wavelength of around 1.3  $\mu\text{m}$  or 1.5  $\mu\text{m}$ , which is most suitable for transmission by glass-fiber. In the first Chapter of this thesis, some general aspects of the isoelectronic centers are discussed and the experimental techniques used in this work are summarized in Chapter 2.

The results of a detailed phenomenological study of the optical properties of a silver-related center in silicon have been reported in Chapter 3. Perturbations of optical transitions by uniaxial stress and magnetic field have been accurately described in terms of an effective-mass electron, orbiting the center in a triply degenerate orbital state of  $T_d$  symmetry, and a tightly bound hole, which has its angular momentum quenched by the local trigonal field of the center. Using effective mass for vibrational mode derived from isotope data, the electron-phonon coupling of a reasonable magnitude is obtained. With this model, the total luminescence and the radiative decay time have been fitted over the 4 - 50 K temperature range. It has also been shown that the data can give an estimate of the time necessary to thermally ionize an electron from an effective-mass state. A detailed phenomenological understanding of the optical properties is therefore achieved, even though the molecular structure of the core of the center has not been determined.

Chapter 4 illustrates how the ionization cross section can be measured for centers of unknown concentrations from time-resolved two-color excitation measurements. The value obtained for a copper center in silicon is verified by comparison with the absorption coefficient reported for shallow donors of a well-defined concentration. Further, the presented data demonstrate a partial recovery of the luminescence after photo-ionization, due to repopulation of the ionized traps.

The first observation of Zeeman effect in PL of Si:Er system has been reported in Chapter 5. This provides the most direct microscopic information on the structure of a prominent center responsible for optical activity of Er in crystalline silicon. From a clear magnetic field induced splitting observed on the main line of the Er-1 PL spectrum, the lower than cubic symmetry of the emitting center is

conclusively identified as orthorhombic- $I$  ( $C_{2v}$ ), with  $\mathbf{g}$  tensor of the ground state of  $g_{\parallel} \cong 18.39 \pm 0.81$ ,  $g_{\perp} \cong 0$ . On the basis of these findings, the paramagnetism of the  $\text{Er}^{3+}$ -related center emitting at  $\lambda \simeq 1.5 \mu\text{m}$  is unambiguously established, and the understanding of the important and notoriously difficult Si:Er system is significantly advanced.

Chapter 6 presents results of a complete magneto-optical study of multilayer Si/Si:Er structures grown by SMBE technique. The presence of Si spacer regions considerably increases emission intensity when compared to that of single layers. The PL of annealed multilayer structures is dominated by emission from a particular center, the Er-1 center, which is then preferentially formed. The PL spectrum of this center is characterized by ultra narrow homogeneous lines. Based on analysis of the magnetic field induced, angular dependent splitting of the PL lines, we confirm the orthorhombic- $I$  symmetry of the Er-1 center and give  $g$ -tensors for several lower-lying levels of the  $^4I_{15/2}$  ground and the lowest excited  $^4I_{13/2}$  state multiplets. In particular, we identify the original  $\Gamma_6$  and  $\Gamma_7$  characters for the lowest crystal-field split levels of the ground and the excited states, respectively. Based on the study, the microscopic structure of the Er-1 center is proposed. It comprises a single  $\text{Er}^{3+}$  ion at a distorted interstitial  $T_d$  site with multiple oxygen atoms in its direct vicinity.

A detailed consideration of excitation mechanisms of the Er-1 center in multilayer Si/Si:Er structures prepared by SMBE under cw and pulse laser pumping is carried out in Chapter 7. The overall excitation cross section for  $\text{Er}^{3+}$  ions is determined as  $\sigma = (6 \pm 2) \times 10^{-15} \text{ cm}^2$ . This high value implies that excitation of the Er-1 center is a very efficient process. Further, by a direct comparison with a calibrated  $\text{SiO}_2:\text{Er}$  sample, it has been concluded that up to  $\sim 32\%$  of the total number of  $\text{Er}^{3+}$  ions present in Si/Si:Er nanolayers can attain optical activity. This represents a considerable improvement over Si:Er prepared by ion implantation and, as discussed in the introduction paragraph of this Chapter, opens new hopes towards realization of optical gain in Si:Er.

The influence of a  $p$ - $n$  junction created by Er implantation at a Si/Si:Er interface on the PL excitation kinetics of the  $\text{Er}^{3+}$  ions has been analyzed in Appendix A. It is shown that dissociation of excitons by the electric field potential at the junction can explain the delayed onset of Er PL, when excited from the non-implanted side of the silicon wafer. This finding confirms that excitons are responsible for excitation of  $\text{Er}^{3+}$  ions in crystalline silicon at low temperatures.

# Samenvatting

Dit proefschrift behandelt fundamentele eigenschappen van enkele optisch actieve, iso-elektronische centra in silicium.

Het radiatieve verval van excitonen, gebonden aan iso-elektronische onzuiverheden, is een belangrijk fysisch proces in kristallijne halfgeleiders, in het bijzonder wanneer de bandkloof indirect is, zoals bij GaP of Si, en radiatieve band-naar-bandtransities verboden zijn wegens behoud van kristalmoment ( $\vec{k}$ ). De motivatie voor de studie die in dit proefschrift wordt beschreven, komt voort uit het praktische belang van fotonica gebaseerd op silicium als weg naar integratie van elektronische en optische componenten. Bovendien kunnen excitoncentra gebonden aan koper- of zilveronzuiverheden in Si, en Er-dopantcentra, die aangeslagen worden via vangst van een exciton, infrarood licht uitzenden met een golflengte van 1.3  $\mu\text{m}$  of 1.5  $\mu\text{m}$ , dat uitermate geschikt is voor transmissie via glasvezels. In het eerste hoofdstuk van dit proefschrift worden enkele algemene aspecten van iso-elektronische centra besproken terwijl de experimentele technieken in hoofdstuk 2 worden belicht.

In hoofdstuk 3 worden de resultaten van een fenomenologische studie naar de optische eigenschappen van een zilvergerelateerd centrum in Si in detail gerapporteerd. Verstoringen van de optische transities onder invloed van uniaxiale mechanische spanning en magnetische velden werden nauwkeurig beschreven in termen van een effectieve-massa-elektron in een baan om het centrum, resulterend in een drievoudig ontaarde toestand met  $T_d$  symmetrie, en een sterk gebonden gat, wiens angulair moment tot nul is herleid door het lokale trigonale kristalveld van het centrum. Indien voor de vibrationele modi de effectieve massa's afgeleid uit data voor isotopen werden gebruikt, werd een aanvaardbare grootte voor de elektron-fononkoppeling teruggevonden. Op basis van dit model konden de totale luminescentie-intensiteiten en de radiatieve vervaltijden in het temperatuurinterval 4 - 50 K worden aangepast. De data leverden ook een schatting op voor de tijd, nodig om een elektron vanuit zijn effectieve-massatoestand thermisch te ioniseren. Op deze wijze werd een gedetailleerd inzicht in de optische eigenschappen van het centrum verkregen, ook al is diens inwendige moleculaire structuur niet volledig bepaald.

Hoofdstuk 4 laat zien hoe uit tijdsgeresolveerd twee-kleurenexcitatie metingen de werkzame doorsnede voor ionisatie kan worden bepaald voor centra met een onbekende concentratie. De waarde verkregen voor een kopercentrum in Si werd geverifieerd door vergelijking met de gerapporteerde absorptiecoëfficiënt van ondiepe donoren met een goed gedefinieerde concentratie. De gepresenteerde data wezen voorts op een gedeeltelijk herstel van de luminescentie na foto-ionisatie doordat de

geoniseerde vallen opnieuw gevuld worden.

De eerste observatie van het Zeeman-effect in de fotoluminescentie van Si:Er wordt in hoofdstuk 5 beschreven. Die leverde de meest directe informatie omtrent de microscopische structuur van een prominent optisch actief erbiumcentrum in kristallijn silicium. Uit de opsplitsing van de belangrijkste lijn in het fotoluminescentiespectrum van het Er-1 centrum kon de symmetrie van dit centrum on-dubbelzinnig als orthorombisch- $I$  ( $C_{2v}$ ) worden gidentificeerd, met als hoofdwaa-den voor de  $g$ -tensor in de grondtoestand :  $g_{\parallel} \sim 18.39$  en  $g_{\perp} \sim 0$ . Op basis van deze resultaten kon het paramagnetisme van dit  $Er^{3+}$ -gerelateerde centrum worden aangetoond, en werd het inzicht in het belangrijke maar berucht moeilijke systeem Si:Er aanzienlijk verruimd.

In hoofdstuk 6 worden de resultaten van een volledige magneto-optische studie van een multi-nonolaagstructuur van Si/Si:Er, vervaardigd volgens de sublimatie moleculaire-bundelepitaaxietechniek (SMBE), weergegeven. De aanwezigheid van Si-spatieerlaagjes zorgde voor een aanzienlijke toename van de emissie-intensiteit in vergelijking met die van enkele Si:Er-laag. Het fotoluminescentiespectrum van uitgegloeide multinanolaagstructuren bleek in hoofdzaak afkomstig van een wel-bepaald centrum, het Er-1 centrum, dat preferentieel gevormd werd. Het fotolu-minescentiespectrum van dit centrum wordt gekarakteriseerd door uiterst smalle homogene lijnen. De analyse van de hoekafhankelijkheid van de opsplitsing van deze lijnen onder invloed van een magnetisch veld bevestigde de orthorombisch- $I$  symmetrie van het Er-1 centrum en leverde  $g$ -tensoren op voor verscheidene laaggelegen niveaus in de  $^4I_{15/2}$  grondtoestand en de  $^4I_{13/2}$  eerste aangeslagen toe-stand. Meer in het bijzonder kon het oorspronkelijk (in  $O_h$  symmetrie)  $\Gamma_6$  en  $\Gamma_7$  karakter van de laagstgelegen kristalveldniveaus, respectievelijk in de grond- en aangeslagen toestand, worden gidentificeerd. Op basis van deze studie werd een microscopisch model voor het Er-1 centrum vooropgesteld. Het omvat een  $Er^{3+}$  ion in een vervormde interstitiele positie met  $T_d$  symmetrie, met meerdere zuurstofatomen in zijn onmiddellijke omgeving.

Hoofdstuk 7 omvat een gedetailleerde beschouwing van de excitatiemechanis-men van het Er-1 centrum in SMBE-vervaardigde multinanolaagstructuren van Si/Si:Er, onder continue en gepulste excitatie. Als waarde voor de effectieve werkzame doorsnede voor excitatie van  $Er^{3+}$  ionen werd  $6.2 \pm 2 \times 10^{-15} \text{ cm}^2$  gevon-den. Deze vrij hoge waarde geeft aan dat de excitatie van het Er-1 centrum een heel efficiënt proces is. Voorts bleek uit vergelijking met een  $SiO_2:Er^{3+}$  calibratiemon-ster dat tot 32% van het totale aantal  $Er^{3+}$ -ionen in de multinanolaagstructuur optisch actief zijn. Dit levert een aanzienlijke verbetering ten opzichte van Si:Er-structuren vervaardigd door ionenimplantatie en opent nieuwe perspectieven voor optische versterking in Si:Er, zoals uiteengezet in de introductie van dit hoofdstuk.

In appendix A wordt de invloed van een p-n-junctie, gecreerd aan het Si/Si:Er grensvlak door Er-implantatie, op de kinetiek van de fotoluminescentie van  $\text{Er}^{3+}$  ionen geanalyseerd. Er werd aangetoond dat de vertraagde aanloop van het fotoluminescentiesignaal bij excitatie via de niet-gemplanteteerde zijde kan worden verklaard door de dissociatie van excitonen in het elektrisch veld over de  $p - n$ -junctie. Deze resultaten bevestigen dat excitonen verantwoordelijk zijn voor de excitatie van  $\text{Er}^{3+}$  ionen in kristallijn Si bij lage temperatuur.



# Acknowledgments

The work described in this thesis has been carried out mainly in the Van der Waals-Zeeman Institute, the University of Amsterdam. I am grateful to many people, who have contributed, directly or indirectly, to the success of this thesis.

First of all, I would like to thank Tom Gregorkiewicz for his daily supervision and assistance. Tom, I am thankful to you for your valuable guidance on science as well as for your support and great help for my personal life whenever I needed it. I appreciate the advices you have given to me during these years very much. I will miss our Friday scientific group meetings. I have learnt a lot from you. Your dedication to work and your positive spirit have greatly influenced me. Thank you for being patient and reading the manuscript of this thesis.

I am deeply indebted to Prof. Friso Van der Veen for having accepted to guide me in the initial time I started in the Van der Waals-Zeeman Institute.

Many thanks go to my group colleagues. Manuel, Mark, Maciej, Nacho, Henk, and Salvo, thanks a lot for your company. My thesis was very much inspired by our discussions not only during our official group meetings but also during daily coffee and lunchtime. Gentlemen, I will miss you and our dreamlike team. I wish the best for all of you in the future.

Although most parts of my work were carried out in the Netherlands, I have constantly received support from the International Training Institute for Materials Science (ITIMS), Hanoi, Vietnam. I would like to express my sincere thanks to the Board of Director of ITIMS: Prof. Dr. Than Duc Hien, Prof. Dr. Nguyen Duc Chien, Prof. Dr. Nguyen Phu Thuy. Without their great support, I would not be able to finish this thesis.

This thesis would not be possible without collaboration of external scientists. I sincerely thank Prof. Irina Yassievich, Dr. Michael Bresler, Dr. Oleg Gusev, Dr. Hanka Przybylinska, and Prof. Gordon Davies, for offering me comments on parts of this thesis. I also thank Prof. Zakhary Krasil'nik, Boris Andreev, Prof. Wolfgang Jantsch, and Dr. Frans Widdershoven, for providing me with samples.

Daily work in the Van der Waals - Zeeman Institute has been possible thanks to Mariet Bos, Rita Vinig, Ina, and Roos. Thank you so much for helping me with all the paperwork. Many thanks also go to Peter and Arend for their help and hospitality. I will miss the Lunar New Year parties you organized for Vietnamese students during my stay here.

I would like to thank also the technicians in the Van der Waals – Zeeman Institute: Bert Zwart, Eddy Inoeng, Tran Dinh Tho, René Rik, Marc Brugman, Derk Bouhuijs, Harry Beukers, Martin Bekelaar, Wim van Aarten, Ron Manuputy, Hugo Schlatter, Ton Riemersma, Ben Harison, Dirk de Vries, Alof Wassink, Jo-

han te Winkel, Flip de Leeuw, Bert Moleman, Willem Moolhuyzen, Wim Koops, Ronald Winter. I am grateful to Ian Bradley, Jon-Paul Wells, Jonathan Phillips, our UK facility scientists and staff members at the Free Electron Laser facility for Infrared eXperiments in Rijhuizen (Nieuwegein).

I would like to take this opportunity to thank also all my former teachers and staff members at the Institute of Materials Science and Institute of Physics, especially Prof. Phan Hong Khoi, Dr. Tran Phan Dat, Dr. Tran Thi Tam, Dr. Nguyen Nhu Dat, Prof. Vu Xuan Quang.

I am thankful to my colleagues in the Van der Walls - Zeeman Institute: Jeroen, Michel, Joost, Bartek, Thao, Huy, Duong, Thang, Dennis, Leonid, Jorge, Yuri, Sara, Tracy, Zhang, Tegus. Somehow, you are also responsible of this work. Thanks for your company and your discussions.

I would like to thank also all staff members of ITIMS, especially Vu Ngoc Hung, Pham Thi Thuan, Tran Kim Tu, Nguyen Phuong Loan, Tran Thu Ha, Tran Kim Anh, Bui Thi Hang, Vu Anh Minh, and Nguyen Minh Hong, for their support and help.

Many thanks are sent to my Vietnamese friends Minh Phuong, Duy Hien, Van Hieu, Thang Long, Tam, Dieu Huong, Viet Ha, Thanh Loan, Lien Huong, Thanh Binh, Buu Hue, Huu Khanh, Thanh Huong, Xuan Tu, La Quang, Diep Tu, Hong Thai, Tran Lam, Lap, Suan Ly, Nguyen Thuy, Thu Tra, Thu Nam, Hong Phong, Thu Hien, Thu Huong, Thanh Thuy, Thanh Tam, Mai Beckelaan, and Nguyen Huy. Thank you all for sharing me with good moments during my stay in Amsterdam.

My special thanks go to My Hanh for her love and continued support. My dear, thank you for everything you have done for me. In particular, I will never forget our special rehearsals for my presentations. Thank you so much for your valuable comments and critique.

Last but not least, my deep thanks are devoted to my dearest beloved ones - my grandparents, my parents and my sister. Thank you for providing me with your love, constant support and continuous encouragement through all the years. I have always tried my best to live up to your expectation.

Amsterdam, September 2004.

Nguyen Quang Vinh

# List of publications

## APS Journals:

1. N. Q. Vinh, H. Przybylinska, Z. F. Krasil'nik, and T. Gregorkiewicz, *Optical properties of a single type of optically active center in Si/Si:Er nanostructures*, Phys. Rev. B **70**, in print (2004).
2. N. Q. Vinh, T. Gregorkiewicz, J. Phillips, G. Davies, *Time-resolved free-electron laser spectroscopy of a copper isoelectronic center in silicon*, Submitted to Phys. Rev. Lett. (2004).
3. N. Q. Vinh, Z. F. Krasil'nik, and T. Gregorkiewicz, *Optical properties of a single type of optically active center in Si/Si:Er nanostructures*, Appl. Phys. Lett. in preparation (2004).
4. Gordon Davies, T. Gregorkiewicz, M. Zafar Iqbal, M. Kleverman, E. C. Lightowers, N. Q. Vinh, and Mengxia Zhu *Optical properties of a silver-related defect in silicon*, Phys. Rev. B **67**, 235111 (2003).
5. N. Q. Vinh, H. Przybylinska, Z. F. Krasil'nik, and T. Gregorkiewicz, *Microscopic structure of Er-related optically active centers in crystalline silicon*, Phys. Rev. Lett. **90**, 066401 (2003).
6. N. Q. Vinh, T. Gregorkiewicz, and K. Thonke, *780-meV photoluminescence band in silver-doped silicon: Isotope effect and time-resolved spectroscopy*, Phys. Rev. B **65**, 033202 (2002).
7. B. J. Pawlak, N. Q. Vinh, I. N. Yassievich, and T. Gregorkiewicz, *Influence of p-n junction formation at a Si/Si:Er interface on low-temperature excitation of Er<sup>3+</sup> ions in crystalline silicon*, Phys. Rev. B **64**, 132202 (2001).
8. O. B. Gusev, M. S. Bresler, P. E. Pak, I. N. Yassievich, M. Forcales, N. Q. Vinh, and T. Gregorkiewicz, *Excitation cross section of erbium in semiconductor matrices under optical pumping*, Phys. Rev. B **64**, 075302 (2001).

## Other Journals:

9. N. Q. Vinh, M. Klik, B. A. Andreev, and T. Gregorkiewicz, *Spectroscopic characterization of Er-1 center in selectively doped silicon*, Mat. Sci. Eng. B-Solid **105**, 150 (2003).
10. H. Przybylinska, N. Q. Vinh, B. A. Andreev, Z. F. Krasil'nik, and T. Gregorkiewicz, *Microscopic structure of Er-related optically active centers in Si*, Mat. Res. Soc. Symp. Proc. Vol. **770**, I7.1.1 (2003).

11. N. Q. Vinh and T. Gregorkiewicz, *Two-color mid-infrared spectroscopy of isoelectronic centers in silicon* Mat. Res. Soc. Symp. Proc. Vol. **770**, I4.2.1 (2003).
12. M. Forcales, M. A. J. Klik, N. Q. Vinh, J. Phillips, J-P. R. Wells, and T. Gregorkiewicz, *Two-color mid-infrared spectroscopy of optically doped semiconductors*, J. Lumin. **102-103**, 85 (2003).
13. N. Q. Vinh, H. Przybylinska, Z. F. Krasil'nik, and T. Gregorkiewicz, *Magneto-optical study of  $Er^{3+}$ -related center in selectively doped Si:Er*, Physica E **16**, 544 (2003).
14. O. B. Gusev, M. S. Bresler, P. E. Pak, I. N. Yassievich, M. Forcales, N. Q. Vinh, and T. Gregorkiewicz, *Excitation cross-section of erbium in semiconductor matrices under optical pumping*, Sol. St. Phen. **82-84**, 651 (2002).
15. M. Forcales, M. Klik, N. Q. Vinh, I. V. Bradley, J-P. R. Wells, T. Gregorkiewicz, *Free-electron laser studies of energy transfer mechanisms in semiconductors doped with transition series ions*, J. Lumin. **94-95**, 243 (2001).
16. N. Q. Vinh, H. Przybylinska, Z. F. Krasil'nik, B. A. Andreev, T. Gregorkiewicz, *Observation of Zeeman effect in photoluminescence of  $Er^{3+}$  ion imbedded in crystalline silicon*, Physica B **308-310**, 340 (2001).
17. N. Q. Vinh, I. N. Yassievich, and T. Gregorkiewicz, *Erbium excitation across the bulk of silicon wafer: an effect of p-n junction at Si/Si:Er interface*, Physica B **308-310**, 357 (2001).
18. N. Q. Vinh, M. A. J. Klik, T. Gregorkiewicz, *Time-resolved photoluminescence study of Si:Ag* Physica B **308-310**, 414 (2001).
19. N. Q. Vinh and T. P. Dat, *Numerical analysis for investigation of dynamic processes of Transversely Excited nitrogen laser*, Proceeding of the Second International Workshop on Materials Science (IWOMS'99), Hanoi, Vietnam, November '99, pp.654 (1999).
20. P. H. Khoi, N. T. T. Tam, N. Q. Vinh, P. L. P. Hoa, and N. T. Tai, *Thermogravimetric investigation of the photoluminescent yellow silicon-based fibers*, The 5th Asian Thermophysical Properties Conference, Seoul, Korea, pp.175 (1998).
21. P. H. Khoi, N. Q. Vinh, N. X. Chanh, and P. H. Huong, *Preparation and properties of photoluminescent silicon yellow fibers*, Modern problems in Optics and spectroscopy, pp.356 (1996).

# Awards

1. “Young Scientist Award” in recognition of best paper presented during the European Materials Research Society Meeting, Symposium on “Rare earth doped materials for photonics”, Strasbourg, France, June 2003.
2. “VIFOTECH Award” the Vietnamese Fund for Supporting Technological Creativity, Hanoi, Vietnam, 1996.

